



Technische Universität München

TUM School
of Natural Sciences

Implementation of MIEZETOP at MIRA and Spin Dynamics in Antiferromagnets

Henrik Johannes Gabold

Vollständiger Abdruck der von der TUM School of Natural Sciences der Technischen Universität München zur Erlangung des akademischen Grades eines

Doktors der Naturwissenschaften (Dr. rer. nat.)

genehmigten Dissertation.

Vorsitzender:

Prof. Dr. Martin Zacharias

Prüfende der Dissertation:

1. Prof. Dr. Peter Böni
2. Prof. Dr. Christian Pfeleiderer

Die Dissertation wurde am 29.08.2022 bei der Technischen Universität München eingereicht und durch die Fakultät für Physik am 29.09.2022 angenommen.

Abstract

This work summarises the implementation of MIEZE at the triple axis spectrometer MIRA and the spin wave analysis of $\text{BaCdVO}(\text{PO}_4)_2$ and CuMnSb . MIEZE is a variant of the neutron spin echo spectroscopy, which offers high energy resolution on dynamics of atomic scale. This allows the measurement of quasi-elastic processes, linewidths of inelastic excitations and fine energy splitting, which is not possible with a standard triple axis spectrometer. By combining MIEZE with a triple axis spectrometer, one obtains a energy resolution of MIEZE, while maintaining the flexibility of triple axis spectroscopy in momentum transfer. Compared to other spin echo techniques, MIEZE allows measurements of depolarising samples and in depolarising environments.

$\text{BaCdVO}(\text{PO}_4)_2$ and CuMnSb are both systems that order antiferromagnetically at low temperatures. $\text{BaCdVO}(\text{PO}_4)_2$ is a quasi two dimensional system and a candidate for exhibiting a spin nematic phase. $\text{BaCdVO}(\text{PO}_4)_2$ was measured in a time-of-flight neutron spectrometer and the resulting spectrum is described by a spin wave model. CuMnSb is a type II antiferromagnet, which shows characteristics of local-moment and itinerant magnetism. CuMnSb was measured with a triple axis spectrometer and the spin wave dispersion at low temperatures has been investigated. It was found that a model including next neighbours up to the fourth order describes the spin wave dispersion best. The obtained exchanged couplings showed that CuMnSb is magnetically frustrated and exhibits, due to the extent range, itinerant interactions.

Zusammenfassung

Diese Arbeit fasst die Implementierung von MIEZE am Dreiachsenspektrometer MIRA und die Spinwellenanalyse von $\text{BaCdVO}(\text{PO}_4)_2$ und CuMnSb zusammen. MIEZE ist eine Variante der Neutronen-Spin-Echo-Spektroskopie, die eine hohe Energieauflösung bei Dynamiken auf atomarer Skala bietet. Dies ermöglicht die Messung von quasi-elastischen Prozessen, Linienbreiten von inelastischen Anregungen und feiner Energieaufspaltung, was mit einem Standard-Dreiachsenspektrometer nicht möglich ist. Durch die Kombination von MIEZE mit einem Dreiachsenspektrometer erhält man die Energieauflösung von MIEZE, während die Flexibilität des Impulsübertrags der Dreiachsenspektroskopie erhalten bleibt. Im Vergleich zu anderen Spinechotechniken ermöglicht MIEZE Messungen an depolarisierenden Proben und in depolarisierenden Umgebungen.

$\text{BaCdVO}(\text{PO}_4)_2$ und CuMnSb sind beides Systeme, die bei niedrigen Temperaturen antiferromagnetisch geordnet sind. $\text{BaCdVO}(\text{PO}_4)_2$ ist ein quasi zweidimensionales System und ein Kandidat für die Ausbildung einer spinnematischen Phase. $\text{BaCdVO}(\text{PO}_4)_2$ wurde mit einem Flugzeit-Neutronenspektrometer gemessen, und das resultierende Spektrum wird durch ein Spinwellenmodell beschrieben. CuMnSb ist ein Typ-II-Antiferromagnet, der Merkmale von lokalisierten Momenten und itineranten Magnetismus aufweist. CuMnSb wurde mit einem Dreiachsenspektrometer gemessen und die Spinwellen-Dispersion bei niedrigen Temperaturen untersucht. Es wurde festgestellt, dass ein Modell, das die nächsten Nachbarn bis zur vierten Ordnung einschließt, die Spinwellenausbreitung am besten beschreibt. Die erhaltenen Austauschkopplungen zeigen, dass CuMnSb magnetisch frustriert ist und aufgrund der Reichweite der magnetischen Wechselwirkung itinerant wechselwirkt.

Contents

Abstract	iii
1 Introduction	1
2 Introduction to Neutron Scattering	3
2.1 Basic Neutron Properties	3
2.2 Fermi's Golden Rule and the Scattering Cross Section	4
2.2.1 Nuclear Scattering	6
2.2.2 Magnetic Scattering	7
3 Implementation of MIEZE on the triple axis spectrometer MIRA	11
3.1 Triple Axis Spectroscopy (TAS)	12
3.2 Spin Echo Techniques	13
3.2.1 Larmor Precession	13
3.2.2 Adiabatic Transition	15
3.3 Classical Neutron Spin Echo (NSE)	16
3.3.1 Mathematical Description of NSE	16
3.4 Neutron Resonance Spin Echo	19
3.4.1 Passage through a RF-flipper	20
3.5 Modulation of Intensity with Zero Effort (MIEZE)	22
3.6 Reduction Factor	25
3.7 MIEZETOP setup	27
3.7.1 The instrument MIRA	28
3.7.2 B_0 Coil System	29
3.7.3 RF-coil	30
3.7.4 $\pi/2$ -flipper	31
3.7.5 Polariser	31
3.7.6 Detector	32
4 First measurements of MIEZETOP	35
4.1 MIEZE Setup	35
4.2 Characterisation and Tuning	36
4.3 Configuration	37
4.4 Reduction Factor in Forward Scattering	41
4.5 Reduction Factor in Diffraction	42
4.6 Reduction Factor in TAS	44
4.7 Summary	45

5	BaCdVO(PO₄)₂	47
5.1	$J_1 - J_2$ model	48
5.1.1	Two-Dimensional square lattice Heisenberg antiferromagnet	49
5.1.2	Generalisation of the $J_1 - J_2$ -model	52
5.1.3	Spin nematic	54
5.2	BaCdVO(PO ₄) ₂	57
5.3	Experimental procedure	60
5.4	Results and Discussion	60
5.5	Summary	63
6	CuMnSb	65
6.1	Structural and Magnetic Properties of CuMnSb	66
6.2	Measurement strategies	68
6.3	Temperature dependence of magnon excitation energy	69
6.4	Dispersion	72
6.4.1	Energy Scans	73
6.4.2	Model of Spin Wave Dispersion	76
6.4.3	Magnon Dispersion	78
6.5	Summary	80
7	Conclusion	83
	Bibliography	89
A	Appendix: Electronic devices	103
B	Appendix: CuMnSb	107
B.1	Temperature dependence of energy scans	108
B.2	Energy scans at T = 2 K for different Q directions	109
B.3	Magnon Linewidth	119

1 Introduction

The neutron was discovered by Chadwick in 1932 and by that, one of the first open questions of nuclear and particle physics were resolved [1]. The description of neutrons by wave mechanics and the consequent scattering by crystalline specimen was suggested by Elsasser [2]. The wave-like behavior of the neutron was experimentally proven by Halban et al. [3] and Mitchel et al. [4]. While these experiments were of pure nuclear scattering, Bloch suggested in the same year that magnetic structures should be observable by neutron scattering due to magnetic moment of the neutron. Consequently, Shull and Smart were able to prove the existence of antiferromagnetic order as predicted by Néel [5] in MnO by the usage of magnetic neutron diffraction [6].

As the complexity of scientific questions increased with the progress in magnetic materials, new and more refined measurement techniques had to be developed. Nowadays, already a variety of principles in neutron scattering techniques have been developed and are dealt in several textbooks [7, 8, 9, 10]. However, there are still limiting factors in neutron scattering, eg. the resolution of small energy scales due to the low flux and brightness of the neutron beam. One approach to lift the limit in resolution are NSE (**N**eutron **S**pin **E**cho) and NRSE (**N**eutron **R**esonant **S**pin **E**cho) techniques, respectively.

The MIEZE (**M**odulation of **I**ntensity with **Z**ero **E**ffort) technique, a variety of NRSE, is a spin echo method with a energy resolution several magnitudes higher than standart methods, like triple axis spectroscopy or time-of-flight spectroscopy. Compared to NRSE, with MIEZE, measurements of magnetic specimen or in depolarising environments can be performed [11]. This allows precise measurements of inelastic or quasielastic scattering in magnetic materials as e.g. line-widths of magnetic excitations, which directly correlates to the lifetime of the excitation. In MnSi, the determination of the skyrmion and helimagnon lifetime is one missing part, that would support the completion of the existing phenomenological theory [12, 13, 14, 15]. Here, NSE techniques are essential because the energy scale is too small at the relevant momentum transfers to resolve it with standard techniques. In this thesis, the implementation of the MIEZE technique at the triple axis instrument MIRA at FRM2, Garching bei München, Germany is presented.

BaCdVO(PO₄)₂ and CuMnSb are both antiferromagnets, whose interactions mechanisms are not fully understood. BaCdVO(PO₄)₂ is a quasi-two dimensional antiferromagnet, which is one candidate to exhibit a spin nematic phase. In this phase, neighbouring spin pairs dimerise into antiferroquadrupolars, which possibly show ordering without breaking the time reversal invariance. The time reversal invariance of the nematic phase makes it invisible for the most magnetic probing techniques such as magnetic neutron diffraction or NMR [16, 17]. Inelastic neutron scattering, however, could be able to resolve the nematic phase as it is expected to express a linear dispersion Goldstone mode. In this thesis, BaCdVO(PO₄)₂ was measured with the time-of-flight spectrometers IN5, ILL,

1 Introduction

Grenoble France and LET, ISIS, Oxfordshire, United Kingdom. The resulting spin wave dispersion was analysed in order to reveal the spin nematic phase.

CuMnSb is a type-II antiferromagnet, in which ferromagnetic planes stack antiferromagnetically along the third direction. Theoretical calculations predicted that for a defect-free crystal at low temperatures the magnetic structure becomes unstable and more complex magnetic structures are energetically more favourable compared to the type-II antiferromagnetism [18]. However, already low defect concentrations stabilise the type-II antiferromagnetic ordering, which explains the observed magnetic structure from [19, 20, 21]. More recent magnetisation and neutron measurements on a high quality CuMnSb crystal revealed an additional phase transition towards lower temperatures within the magnetic phase that include a change in the magnetic phase group [22]. In this thesis, the results of triple axis spectroscopy on a high quality CuMnSb crystal, performed at EIGER, PSI, Villigen, Switzerland, are presented and analysed. By modelling the spin wave dispersion, the exchange interactions are quantified and the interaction mechanisms of low temperature phase is further disclosed.

2 Introduction to Neutron Scattering

In this chapter the advantages of neutron scattering to other probing techniques are discussed. The fundamental equations of neutron scattering will be presented, which are derived in detail in the two textbooks [8, 10].

2.1 Basic Neutron Properties

A neutron is a particle with a mass of $m \approx 1.675 \times 10^{-24}$ kg and has zero charge. Compared to proton, electron or x-ray scattering experiments, where the particle interacts mainly with the electron orbitals, the neutron interacts directly with the atomic nucleus. As the interaction via nuclear forces are of short range, the lower interaction probability of a neutron with a solid leads to a $\approx 10^3$ larger penetration depth compared to other scattering experiments. This allows the investigation of bulk materials and the application of extreme environmental conditions. By this means, temperatures from a few mK to over thousand degrees, high pressures, electric fields, magnetic fields of several tesla or any combinations of these can be applied.

Furthermore, neutrons are spin- $\frac{1}{2}$ particles and, thus, possess a magnetic moment $\mu_n = e\hbar/2m$. The magnetic moment makes neutron scattering a unique technique for probing static and dynamic magnetic properties as the magnetic moment of the neutron interacts with unpaired electrons. Hence, it is possible to investigate magnetic ordering phenomena or magnetic excitations in condensed matter. Especially polarised neutron scattering has opened further possibilities for the investigation of magnetic materials, as the interaction strength between a neutron and a nuclear spin depends on their spin alignment.

However, neutrons, coming from the fuel element of a reactor, do not necessarily have the kinetic energy as it is needed for a specific experimental setup. The average energy of the neutrons can be changed by a moderator, in which the neutrons gain or lose energy by inelastic collisions with the atoms of the moderator material. The resulting kinetic energy of the neutrons is Maxwell distributed and depends on the moderator temperature. In condensed matter physics, the energy of a neutron is usually divided into groups of different moderator temperatures, e.g. 'cold', 'thermal' and 'hot', see table 2.1. The relation of the kinetic energy and the moderator temperature is given by

$$E_{\text{kin}} \approx k_B T. \quad (2.1)$$

The small mass of neutrons $m \approx 1u$ makes cold and slow thermal neutrons ideal for inelastic scattering experiments, as the neutron's kinetic energy is of the same order of magnitude as the excitations. The exact choice of energy depends on the investigated excitations.

2 Introduction to Neutron Scattering

Faster thermal and hot neutrons, in contrast, have a de-Broglie wavelength λ of the same order of magnitude as the average interatomic distances in solids or dense liquids. These energies are ideally suited for the analysis of atomic structures in diffraction experiments, which utilise the inference of neutron waves. Nevertheless, hot neutrons are also used for inelastic experiments with high energy transfers or for liquid and amorphous structure factor measurements with high momentum transfers.

Source	Energy (meV)	Temperature (K)	Wavelength (Å)
cold	0.1-10	1-120	30-3
thermal	5-100	60-1000	4-1
hot	100-500	1000-6000	1-0.4

Table 2.1: Temperature ranges of neutrons and their corresponding energy and wavelength (from [10])

2.2 Fermi's Golden Rule and the Scattering Cross Section

Scattering experiments focus on the study of structures and excitations in condensed matter. The interaction of neutrons with a sample is investigated by measuring the probability that a neutron with wave vector \mathbf{k} and energy $E = \frac{\hbar^2}{2m_n}k^2$ is scattered into a state with wave vector \mathbf{k}' and energy $E' = \frac{\hbar^2}{2m_n}k'^2$. The transferred momentum is

$$\mathbf{Q} = \mathbf{k} - \mathbf{k}'. \quad (2.2)$$

The variable \mathbf{Q} is known as the scattering vector. The state of the scattering system changes from $|\lambda\rangle \rightarrow |\lambda'\rangle$ with an energy transfer [10]

$$\hbar\omega = E - E' = \frac{\hbar^2}{2m_n}(\mathbf{k}^2 - \mathbf{k}'^2). \quad (2.3)$$

In a simple scattering experiment, a particle beam with a wave vector \mathbf{k} impinges on a sample as shown in figure 2.1. The number of neutrons per incident flux that interact with the sample and are scattered in all directions defines the *total scattering cross-section*,

$$\sigma = \frac{\text{particles scattered per second}}{\text{incident flux}}. \quad (2.4)$$

Considering a measurement, where all neutrons are counted, which were scattered into a specific solid angle $d\Omega$ in the direction of θ and ϕ . The corresponding cross-section is known as the *differential cross-section*

$$\frac{d\sigma}{d\Omega} = \frac{\text{particles scattered per second into } d\Omega}{\text{incident flux}}. \quad (2.5)$$

In inelastic experiments, additionally to the direction of the neutrons, the transferred energy is analysed. By counting all scattered neutrons in a specific direction, whose

2.2 Fermi's Golden Rule and the Scattering Cross Section

energy lies between E' and $E' + dE$, one defines the *partial differential cross-section*

$$\frac{d^2 \sigma}{d\Omega dE} = \frac{\text{particles scattered per second into } d\Omega \text{ with a final energy between } E' \text{ and } E' + dE}{\text{incident flux}}. \quad (2.6)$$

Figure 2.1 illustrates the *partial differential cross-section*. Since neutrons are a very weak perturbation to the measured system, one can apply first order-perturbation theory and the *partial differential cross section* can be described via Fermi's golden rule [10]

$$\left. \frac{d^2 \sigma}{d\Omega dE} \right|_{\lambda \rightarrow \lambda'} = \frac{k'}{k} \left(\frac{m_n}{2\pi\hbar^2} \right) \left| \langle \mathbf{k}' \lambda' | V | \mathbf{k} \lambda \rangle \right|^2 \delta(\hbar\omega + E_\lambda - E_{\lambda'}). \quad (2.7)$$

The initial and final state of the probed system are denoted by λ and λ' , respectively. E_λ and $E_{\lambda'}$ are the initial and final energy of the scattered system, such that

$$E + E_\lambda = E' + E_{\lambda'}. \quad (2.8)$$

The quantity $\hbar\omega$ is the energy transfer from the neutron to the system, V is the interaction operator for the neutron with the probed system and δ is the Dirac delta distribution. The exact interaction potential for the neutron depends on the type of scattering process, which is either nuclear or magnetic [23].

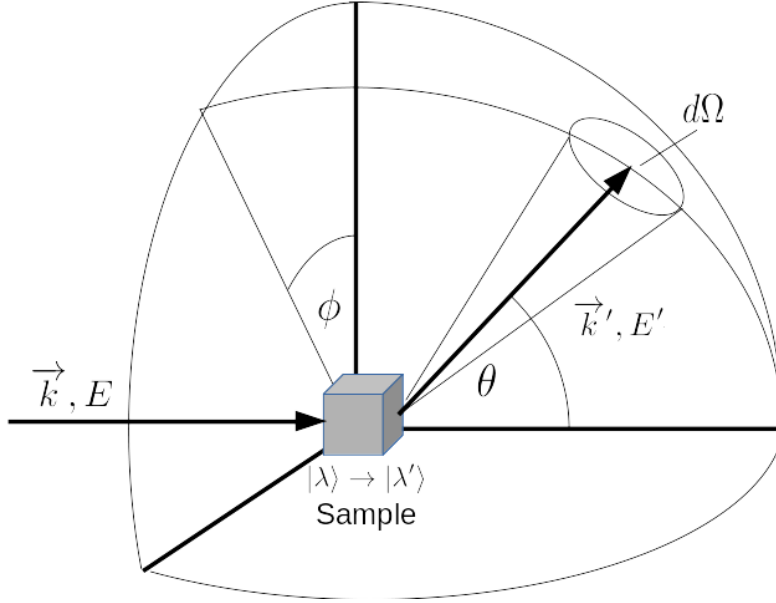


Figure 2.1: Visualisation of the partial differential cross-section. The incident beam with momentum \mathbf{k} and energy E is scattered by a sample and the sample changes from state $|\lambda\rangle \rightarrow |\lambda'\rangle$. The partial differential cross-section is the amount of scattered particles into $d\Omega$ and within the energy interval E' and $E' + dE$.

2.2.1 Nuclear Scattering

As neutron scattering is considered as a weak perturbation, the first Born approximation can be applied to describe scattering events [8]. Hereby, the interaction matrix elements are calculated by treating the incident and the outgoing neutrons as plane waves. The total potential is given by the sum over the interaction potentials of all scattering centres

$$V(\mathbf{r}) = \sum_i V_i(\mathbf{r} - \mathbf{R}_i), \quad (2.9)$$

with \mathbf{R}_i being the position of the i -th scattering centre. The matrix elements of equation (2.7) can then expressed as

$$\langle \mathbf{k}'\lambda' | V | \mathbf{k}\lambda \rangle = \sum_i V_i(\mathbf{Q}) \langle \lambda' | \exp i\mathbf{Q}\mathbf{R}_i | \lambda \rangle, \quad (2.10)$$

where

$$V_i(\mathbf{Q}) = \int d\mathbf{r} V(\mathbf{r}) \exp(i\mathbf{Q}\mathbf{r}) \quad (2.11)$$

is the spatial Fourier transformation of $V(\mathbf{r})$ and describes the potential in the reciprocal space. The change in momentum is defined in equation (2.2). Since the interaction range of nuclear scattering is several orders of magnitude smaller than the neutrons wavelength, the nuclear potential can be described by a delta function

$$V_i(\mathbf{r}) = \frac{2\pi\hbar^2}{m} b_i \delta(\mathbf{r} - \mathbf{R}_i), \quad (2.12)$$

where the i -th nucleus has a scattering length of b_i . The scattering length b_i depends on the element and isotope of the scattering nucleus. Equation (2.12) is known as the *Fermi pseudopotential*. Inserting *Fermi pseudopotential* equation (2.12) into equation (2.11) one gets

$$V_i(\mathbf{Q}) = \frac{2\pi\hbar^2}{m} b_i. \quad (2.13)$$

Inserting the matrix elements given by equation (2.10) using equation (2.13) into equation (2.7) the partial differential cross-section becomes

$$\left. \frac{d^2\sigma}{d\Omega dE} \right|_{\lambda \rightarrow \lambda'} = \frac{k'}{k} \left| \sum_j b_j \langle \lambda' | \exp(i\mathbf{Q}\mathbf{R}_j) | \lambda \rangle \right|^2 \delta(\hbar\omega + E_\lambda - E_{\lambda'}). \quad (2.14)$$

Equation (2.14) describes a single scattering process, in which one neutron changes its wave vector $\mathbf{k} \rightarrow \mathbf{k}'$ with a momentum transfer of \mathbf{Q} and the scattering system goes from state λ to λ' .

However, a real scattering experiment does not consist of a single transition. Instead one measures an ensemble of neutrons, each with a momentum and energy transfer, described by the *partial differential cross-section* as defined in equation (2.6). Hence, one

has to sum over all possible final states λ' and to average over all initial states, which yields

$$\frac{d^2 \sigma}{d\Omega dE} = \frac{k'}{k} \sum_{\lambda, \lambda'} p(\lambda) \left| \langle \lambda' | \sum_j b_j \exp(i\mathbf{Q}\mathbf{r}_j) | \lambda \rangle \right|^2 \delta(\hbar\omega + E_\lambda - E_{\lambda'}), \quad (2.15)$$

where $p(\lambda)$ is statistical weighting factor for the initial state $|\lambda\rangle$. Assuming all nuclei have the same scattering length b , Van Hove [24] showed that equation (2.15) can equivalently be expressed as

$$\frac{d^2 \sigma}{d\Omega dE} = N \frac{k'}{k} b^2 S(\mathbf{Q}, \omega), \quad (2.16)$$

where

$$S(\mathbf{Q}, \omega) = \frac{1}{2\pi\hbar N} \sum_{j, j'} \int_{-\infty}^{\infty} dt \langle \exp(-i\mathbf{Q}\mathbf{r}_{j'}(0)) \exp(i\mathbf{Q}\mathbf{r}_j(t)) \rangle \exp(-i\omega t) \quad (2.17)$$

is the dynamic structure factor. Hereby, N is the number of scattering nuclei, t is time and the angle brackets $\langle \cdot \rangle$ denote the thermal average over the initial states. The dynamical structure factor $S(\mathbf{Q}, \omega)$ is the time Fourier transformation of the intermediate scattering function $I(\mathbf{Q}, t)$, defined as

$$I(\mathbf{Q}, t) = \frac{1}{N} \sum_{j, j'} \langle \exp(-i\mathbf{Q}\mathbf{r}_{j'}(0)) \exp(i\mathbf{Q}\mathbf{r}_j(t)) \rangle, \quad (2.18)$$

which is, in turn, direct proportional to the spatial Fourier transformation of the van Hove density-density correlation function [24]

$$G(\mathbf{R}, \tau) = \int dt \int d^3r \langle \rho(\mathbf{r}, t) \rho(\mathbf{r} + \mathbf{R}, t + \tau) \rangle. \quad (2.19)$$

The dynamical structure factor is independent of k and k' , and it solely depends on the transferred momentum and energy from the neutron to the sample. In other words, it is the probability of the neutron's change in energy and momentum in a scattering process. Thus, the goal of inelastic neutron experiments can be rephrased as to measure the dynamical structure factor and to obtain, by that, information on the structure and dynamics of the investigated system [23].

2.2.2 Magnetic Scattering

One of the major benefits in neutron scattering is the interaction of the neutron with magnetic moments [9]. The magnetic moment of a neutron can be expressed in terms of pauli matrices $\hat{\sigma}$ by

$$\hat{\boldsymbol{\mu}}_n = \gamma \mu_N \hat{\boldsymbol{\sigma}}, \quad (2.20)$$

where $\gamma = -1.91$ [25] is the gyromagnetic ratio in units of μ_N , where μ_N is the nuclear Bohr magneton

$$\mu_N = \frac{e\hbar}{2m_p}, \quad (2.21)$$

2 Introduction to Neutron Scattering

with the mass of a proton m_p and the electron charge e . The interaction of a neutron with a magnetic field \mathbf{H} is expressed by

$$\hat{\boldsymbol{\mu}}_n \cdot \mathbf{H} = -\gamma\mu_N\hat{\boldsymbol{\sigma}}. \quad (2.22)$$

In magnetic neutron scattering experiments, the corresponding field is usually generated by the unpaired electrons of the sample. The operator for the magnetic dipole moment of a free electron is

$$\hat{\boldsymbol{\mu}}_e = -2\mu_B\hat{\mathbf{s}}, \quad (2.23)$$

with the Bohr magneton

$$\mu_B = \frac{e\hbar}{2m_e}, \quad (2.24)$$

the electron mass m_e and the spin angular momentum operator $\hat{\mathbf{s}}$. An electron gives two contributions to the local field, namely magnetic dipole moment of the electron and magnetic moment generated by the momentum of the electron. The magnetic dipole moment of the electron at position \mathbf{R} is given by

$$\mathbf{H}_S = \nabla \times \left(\frac{\mu_0}{4\pi} \frac{\boldsymbol{\mu}_e \times \mathbf{R}}{|\mathbf{R}|^3} \right), \quad (2.25)$$

whereas the field that is generated by the momentum is given by

$$\mathbf{H}_L = -\frac{\mu_0\mu_B}{2\pi\hbar} \frac{\mathbf{p} \times \mathbf{R}}{|\mathbf{R}|^3}. \quad (2.26)$$

Hence, using equations (2.22) to (2.26) the interaction potential becomes

$$-\boldsymbol{\mu}_n \cdot (\mathbf{H}_S + \mathbf{H}_L) = -\frac{\mu_0}{4\pi} \gamma\mu_N 2\mu_B \sigma \left(\nabla \times \left(\frac{\mathbf{s} \times \mathbf{R}}{|\mathbf{R}|^3} \right) - \frac{\mathbf{p} \times \mathbf{R}}{|\mathbf{R}|^3} \right). \quad (2.27)$$

By inserting the magnetic interaction potential equation (2.27) into Fermi's Golden Rule equation (2.7), one gets, after some calculation [8, 9, 10], the magnetic scattering cross section

$$\frac{d^2\sigma}{d\Omega dE} = (\gamma r_0)^2 \frac{k'}{k} F^2(\mathbf{Q}) \exp(-2W(\mathbf{Q})) \sum_{\alpha,\beta} \left(\delta_{\alpha\beta} - \frac{Q_\alpha Q_\beta}{Q^2} \right) S^{\alpha\beta}(\mathbf{Q}, \omega), \quad (2.28)$$

with $\alpha, \beta = x, y, z$ and $r_0 = \gamma e^2 / m_e c^2 \approx 0.54 \times 10^{-15}$ m is the classical electron radius. Further, the magnetic form factor $F(\mathbf{Q})$, the Debye-Waller factor $\exp(-2W(\mathbf{Q}))$ and the magnetic scattering function were introduced. The magnetic form factor $F(\mathbf{Q})$ is the Fourier transformation of the density of unpaired electrons and decreases drastically with \mathbf{Q} . The magnetic scattering cross-section per electron $4\pi(\gamma r_0)^2$ is under suitable conditions of the same order of magnitude as nuclear scattering, which is a crucial property of neutron scattering. The magnetic cross section depends on the angle between the sample's moments and the scattering vector, so that the magnetic moment of the neutron

2.2 Fermi's Golden Rule and the Scattering Cross Section

only couples to moments perpendicular to \mathbf{Q} . The magnetic scattering function $S^{\alpha\beta}(\mathbf{Q}, \omega)$ contains all information regarding the magnetic structure and dynamic of the sample. It can be expressed as [10]

$$S^{\alpha\beta}(\mathbf{Q}, \omega) = \frac{1}{2\pi\hbar} \sum_{i,i'} \int_{-\infty}^{\infty} dt \exp(i\mathbf{Q}(\mathbf{R}_i - \mathbf{R}'_i)) \langle S_i^\alpha(0) S_{i'}^\beta(t) \rangle \exp(-i\omega t). \quad (2.29)$$

The magnetic scattering function $S^{\alpha\beta}(\mathbf{Q}, \omega)$ is complementary to the nuclear dynamic scattering function and it corresponds to the probability of finding a magnetic moment j' at position \mathbf{R}'_i at time t . The fluctuation dissipation theorem allows to connect the $\alpha\beta$ -component of the scattering function $S^{\alpha\beta}(\mathbf{Q}, \omega)$ with the imaginary part of the dynamic susceptibility tensor $\chi^{\alpha\beta}(\mathbf{Q}, \omega)$ [26]

$$S^{\alpha\beta}(\mathbf{Q}, \omega) = \frac{N\hbar}{\pi} \left(1 - \exp\left(-\frac{\hbar\omega}{k_B T}\right) \right) \text{Im}(\chi^{\alpha\beta}(\mathbf{Q}, \omega)), \quad (2.30)$$

with N being the total number of ions and the thermal population factor

$$\left(1 - \exp\left(-\frac{\hbar\omega}{k_B T}\right) \right)^{-1} = \langle n + 1 \rangle. \quad (2.31)$$

The dynamic susceptibility $\chi^{\alpha\beta}(\mathbf{Q}, \omega)$ describes the linear response of a scattering system to a small, inhomogeneous magnetic field with a wave vector \mathbf{Q} and energy ω . Its imaginary part $\text{Im}(\chi^{\alpha\beta}(\mathbf{Q}, \omega))$ determines the mean energy dissipation rate in the system [27, 28]. Equation (2.30) can be used directly to model inelastic magnetic neutron scattering data.

For inelastic magnetic signals, e.g. spin waves, it is appropriate to use the Lorentzian spectral weight function to describe the dynamic susceptibility tensor by [29]

$$\text{Im}(\chi^{\alpha\beta}(\mathbf{Q}, \omega)) = \frac{\chi(\mathbf{Q})}{2\pi} \left(\frac{\hbar\omega\Gamma}{\hbar[\omega - \omega(\mathbf{Q})]^2 + \Gamma^2} + \frac{\hbar\omega\Gamma}{\hbar[\omega + \omega(\mathbf{Q})]^2 + \Gamma^2} \right). \quad (2.32)$$

Hereby $\hbar\omega(\mathbf{Q})$ is the energy of the excitation, which is usually described by the dispersion relation of the corresponding excitation. Γ is the line width of the excitation, which correlates to the lifetime of an excitation. For spinwaves, the line width is generally expected to correlate with the energy and scales with a power law regarding temperature and \mathbf{Q} . The exact nature of the static susceptibility $\chi(\mathbf{Q})$ depends on the type of excitation, generally one expects $\chi(\mathbf{Q}) \sim Q^{-2}$ for magnetic excitations [29]. The two terms, that only differ in sign, refer to energy gain and energy loss processes, similar to Stokes and anti-Stokes in optical spectroscopy.

3 Implementation of MIEZE on the triple axis spectrometer MIRA

The energy spectrum of neutron scattering experiments usually consists of two contributions: The inelastic lines due the interaction of neutrons with matter exciting or de-exciting quantum states and a sharp elastic line with no energy transfer. But also the interaction of neutrons with diffusing or reorienting particles, as in liquids or in hot solids, is possible. Such interaction processes lead to a broadening of the elastic line and are usually referred to 'quasielastic' scattering[30, 31]. Quasielastic neutron scattering includes complex scientific questions of very slow dynamics such as molecular rotation, molecular tunneling, diffusion, polymer reptation, relaxation or glassy dynamics. Since the energy resolution of inelastic techniques like triple-axis spectroscopy (TAS) or time-of-flight (TOF) are typically in the order of $\delta E \approx 50 - 150 \mu\text{eV}$ [32], only motions on the time scale of $10^{-13} - 10^{-12}$ s can be investigated. However, there are slow dynamical processes, which happen in time scales up to $1 \mu\text{s}$, with corresponding energy transfers in the sub μeV regime, which cannot be resolved with TAS or TOF. Neutron backscattering instruments can reach an energy resolution down to sub μeV , however, the backscattering technique lacks of a sufficient Q -resolution [33]. Additionally, the Liouville theorem asserts that volume in phase space enclosed by adjacent trajectories is constant as a function of time. As a consequence in neutron scattering, the neutron flux is limited by the instrumental resolution and vice versa. Thus, neutron backscattering becomes inadequate for many studies of time scales longer than $\approx 10^{-10}$ s, due to low count rates.

Mezei successfully demonstrated in 1972, that the Liouville theorem can be circumvented by introducing a new technique, the neutron spin echo (NSE) [34]. In this polarised neutron technique, the neutron spin acts as a 'clock', that rotates in a long, constant magnetic field due to Larmor precession. Small changes in the kinetic energy of the neutron due to inelastic processes lead to a deviation of the neutron spin rotation angle. This new approach allowed to access energy scales, that have not been resolvable with other scattering methods. In contrast to standard scattering techniques, NSE measures directly the time-dependence τ of the intermediate scattering function, which will explained more detailed in section 3.3.

Golub and Gähler introduced the neutron resonance spin echo (NRSE) technique in 1987, which is a variant of NSE [35]. In this technique the long constant field regions of NSE are replaced by short resonant field spin flippers. Even though NRSE can not yet access a Fourier range comparable to NSE, the great advantage is the possibility to be combined with a triple axis instrument. This enables the measurement of line widths of dispersing excitations or the measurement of fine energy levels over the entire Brillouin zone.

However, the tremendous drawback of NSE and NRSE is the inherent sensitivity to depolarising samples like superconductors, materials with magnetic order or the application of an external magnetic field [36]. The **M**odulation of **I**ntensity with **Z**ero **E**ffort (MIEZE) technique is a further development of NRSE, which mitigates the sensitivity towards depolarising effects. The only user-open MIEZE setup is currently provided by the beamline RESEDA at FRM2, Garching, Germany [37]. Given the geometry of RESEDA, the MIEZE technique has only been applied in forward scattering geometry, which strongly limits the accessible Q -range.

In the following, the integration of the MIEZE technique into the existing triple axis instrument MIRA is presented. The combination of MIEZE and TAS not only increases the instruments energy resolution, it further enables the measurement of the line width of inelastic signals of depolarising sample in a depolarising environment. Thus, one can precisely determine the life time of excitations, e.g. magnons.

3.1 Triple Axis Spectroscopy (TAS)

In TAS, one measures $S(\mathbf{Q}, \omega)$ at discrete points in the (\mathbf{Q}, ω) space. Usually, either the energy transfer $\hbar\omega$ or the momentum transfer \mathbf{Q} is kept fixed, while the other variable is scanned. The following description of the TAS method follows mainly [7, 23], the details of the specific TAS 'MIRA' are taken from Ref. [32, 38].

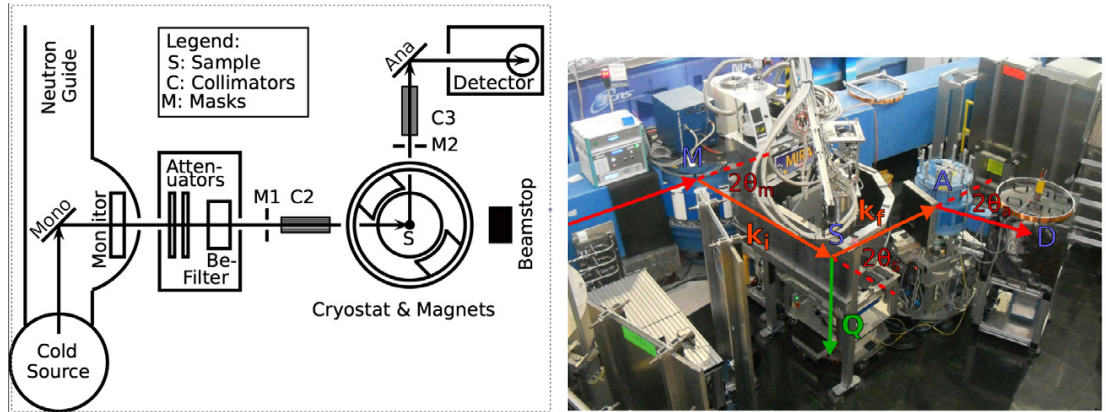


Figure 3.1: Triple Axis Spectrometer. A schematic of a triple axis spectrometer (left). The arrow shows the neutron flight path. A specific wavelength from the neutron beam is selected by the monochromator (Mono). The analyser (Ana) selects a certain energy transfer of the scattered neutrons. The incident and outgoing angle on the sample determines the momentum transfer. The number of neutrons with a specific momentum and energy are counted by the detector. The TAS MIRA at FRM2 (right). The red arrow shows the neutron flight path. The blue label denote the monochromator (M), sample stage (S) and analyser (A). The transferred momentum is $Q = k_i - k_f$ [32, 39].

A TAS consists of three stages, namely the monochromator, the sample stage and the analyser. The first axis, the monochromator, selects a specific wavelength band from the

polychromatic neutron beam coming from the moderator. The monochromator selects a wavelength by utilising Bragg's law

$$n\lambda = 2d_{hkl} \sin \theta. \quad (3.1)$$

Hereby the polychromatic neutron beam impinges on a crystal with a known lattice spacing d_{hkl} , e.g., pyrolytic graphite (PG). Only neutrons, which fulfil Bragg's law are reflected by the crystal and by adjusting the angle of incoming neutrons towards the crystal planes, a specific wavelength λ can be chosen. The selected wavelength λ determines the energy E and momentum $|\mathbf{k}|$.

The principle of the analyser is identic to the monochromator: Again, by utilising Bragg's law a specific energy E' can be selected from the scattered neutron beam. The combination of specific monochromator and analyser configurations allows only neutrons with energy transitions $E - E' = \hbar\omega$ to be measured. The momentum transfer $\mathbf{Q} = \mathbf{k} - \mathbf{k}'$ is determined by the choice of scattering angles at the sample stage. The configuration of the three axis measures only the neutrons with the chosen momentum and energy transfer (\mathbf{Q}, ω) . Thereby, one receives the intensity of the *partial differential cross-section* as defined in equation (2.6), and, consequently, the dynamical scattering function $S(\mathbf{Q}, \omega)$.

Beside the main elements of a triple axis instrument, there are other components to improve or alternate the properties of the neutron beam: Collimators (C) are used to reduce the beam divergence which is determined by the monochromator crystal and neutron guide. Collimators C2, C3 are placed in front and after the sample stage, as shown in figure 3.1 . A cooled Be-filter reduces the background signal by filtering higher order reflections n of the Bragg condition equation (3.1). The masks (M1, M2) are slits geometrically shaping the beam. The monitor measures the incident number of neutrons in order to normalize it with the signal measured in the detector.

3.2 Spin Echo Techniques

All spin echo techniques have the common principle of using the Larmor precession of a neutron as a 'clock' to measure small differences in the flight time of the particle. One measures the relative change of flight time of scattered neutrons with respect to unscattered neutrons over a certain distance. From the difference in neutron velocity one can deduce the gain or loss in the kinetic energy of the neutron. Thereby, small changes in energy can be measured, which are not resolvable by other scattering techniques. The resulting energy resolution is several orders of magnitude better than TAS or TOF, while not being limited by the Liouville theorem.

3.2.1 Larmor Precession

Larmor precession is the rotation of the spin within a magnetic field, where the rotational frequency depends on the magnetic field strength. It is a characteristic property of particles with a magnetic dipole moment and the fundament for all spin echo techniques. The time evolution of a neutron spin, expressed in Pauli matrices $\boldsymbol{\sigma} = (\sigma_x(t), \sigma_y(t), \sigma_z(t))$,

in a known field $\mathbf{B}(t)$ is given by

$$\frac{d}{dt}\boldsymbol{\sigma}(t) = -\frac{\gamma_N\mu_N}{\hbar} [\mathbf{B}(t) \times \boldsymbol{\sigma}(t)]. \quad (3.2)$$

Applying a constant field along the z -axis

$$\mathbf{B}(t) = \begin{pmatrix} 0 \\ 0 \\ B_z \end{pmatrix}, \quad (3.3)$$

the three components of equation (3.2) become

$$\frac{d\sigma_x}{dt} = -\omega_L\sigma_y, \quad \frac{d\sigma_y}{dt} = \omega_L\sigma_x, \quad \frac{d\sigma_z}{dt} = 0, \quad (3.4)$$

which can be solved by

$$\sigma_x(t) = \cos(\omega_L t)\sigma_x(0) - \sin(\omega_L t)\sigma_y(0) \quad (3.5)$$

$$\sigma_y(t) = \sin(\omega_L t)\sigma_x(0) + \cos(\omega_L t)\sigma_y(0) \quad (3.6)$$

$$\sigma_z(t) = \sigma_z(0) \quad (3.7)$$

where ω_L is the Larmor frequency and defined by

$$\omega_L = \frac{-\gamma_N\mu_N B}{\hbar} = \gamma_L B. \quad (3.8)$$

The quantity γ_L is the gyromagnetic ratio and $\gamma_L = -1.832 \times 10^8 \text{ s}^{-1}\text{T}^{-1}$ in SI-units. Equations (3.5) to (3.7) show that only the perpendicular components of the spin precess around the magnetic field vector, while the parallel component stays unchanged [7]. Figure 3.2 shows spin rotation around a constant field. In spin echo techniques, the

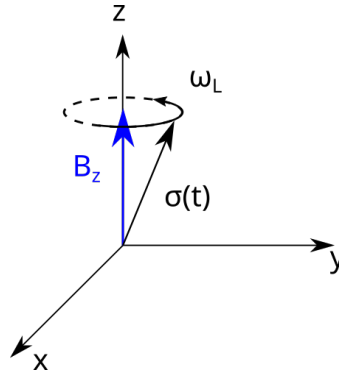


Figure 3.2: Illustration of the Larmor precession. The spin of a particle $\sigma(t)$ rotates around the applied magnetic field B_z with the frequency ω_L

integrated rotation of the polarisation of the neutron beam is considered as the phase.

The total phase a neutron gains within a magnetic field is determined by the field line integral and the neutron velocity

$$\Delta\phi = \frac{\int_0^L dlB(l)}{v}, \quad (3.9)$$

with a magnetic field region of the length L and a magnetic field $B(l)$ [34]. As the polarisation of the neutron beam acts as a clock in spin echo methods, the phase ϕ refers to the pointer of the clock and is the quantity, which is utilised to measure changes in the neutrons energy.

3.2.2 Adiabatic Transition

The Larmor precession can be utilised to adiabatically rotate the neutron spin, which is easier to be realised than drastic changes in the magnetic fields. If the direction of a magnetic field changes sufficiently slow the parallel component of the neutron spin is conserved [7]. A neutron spin that is initially parallel to the magnetic field follows the slow change of the effective field direction. Hereby, the adiabaticity of the process is described by the adiabaticity parameter

$$\mathcal{E} = \frac{\omega_L}{\omega_B}, \quad (3.10)$$

which is defined by the ratio of the Larmor frequency ω_L and the angular rotation of the magnetic field ω_B . If one assumes a neutron travelling along the x -direction with velocity v and a magnetic field rotating with a constant angular rate $\frac{d\theta_B}{dx}$, the angular rotation of the field from the perspective of the neutron spin can be expressed as

$$\omega_B = \frac{d\theta_B}{dt} = \frac{d\theta_B}{dx}v. \quad (3.11)$$

The adiabaticity parameter becomes then

$$\mathcal{E} = \frac{\gamma_L B}{\frac{d\theta_B}{dx}v}, \quad (3.12)$$

where equations (3.8) and (3.11) have been used. In order to minimise the loss of polarisation in the transition process, empirically, a adiabaticity parameter of $\mathcal{E} > 10$ has been proven to be reasonable [7]. Thus, one has to ensure that the angular change in the magnetic field direction is either sufficiently slow or the field strength is strong enough along the transition. The resulting empirical condition over the whole transition process is

$$\left. \frac{d\theta_B}{dx} \right|_x < 2.65B(x) [\text{T}] \lambda \left[\text{\AA} \right], \quad (3.13)$$

with the angular rotation of the magnetic field $\left. \frac{d\theta_B}{dx} \right|_x$, the neutron wavelength λ in ångström and the magnetic field strength $B = |\mathbf{B}|$ at position x in tesla. The constant 2.65 is the result of all physical constants and conversions factors.

3.3 Classical Neutron Spin Echo (NSE)

The general setup of a NSE is illustrated in figure 3.3. It is composed of two constant magnetic field regions with opposite direction $\mathbf{B}_1 = -\mathbf{B}_2$. A polariser is placed before the first constant field \mathbf{B}_1 region and another polariser is placed after the second constant field \mathbf{B}_2 region. As a neutron enters fully polarised the first region, the spin precesses around the magnetic field \mathbf{B}_1 by the total angle ϕ_1 . If the neutron passes the sample stage without being scattered inelastically it receives in the second region the same inverted total rotation angle in opposite direction and the initial neutron polarisation is restored. This setup is independent of the neutron velocity distribution since the field line integral of the first field region \mathbf{B}_1 is the same as the second field region \mathbf{B}_2 .

If a neutron is scattered inelastically, the neutron velocity changes and thus the phase obtained in \mathbf{B}_2 differs compared to \mathbf{B}_1 . The polarisation of the neutron at the second polariser position is then either under- or over-compensated and *not* fully restored. Thereby the amount of the neutrons passing the second polariser is reduced, i.e. the measured signal is damped compared to the elastically scattered neutron. This reduction in polarisation is directly correlated with the inelastic scattering process.

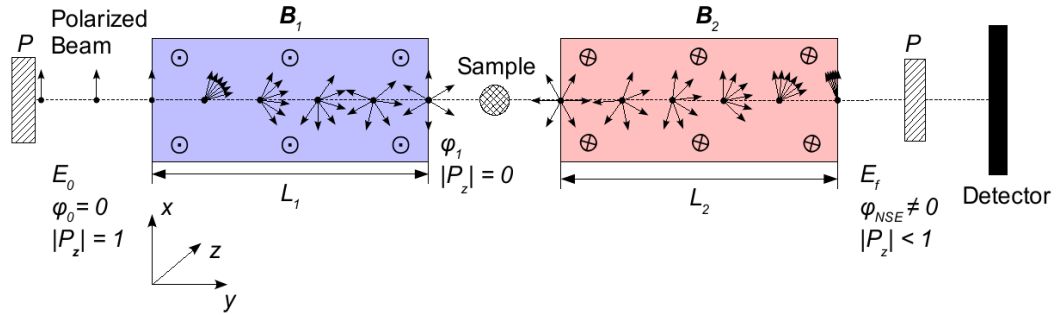


Figure 3.3: Schematic of a NSE spectrometer. A polarised neutron beam passes through regions with opposing magnetic field \mathbf{B}_1 and \mathbf{B}_2 . In region of \mathbf{B}_1 the spin of the neutrons precesses around the magnetic field. If the neutron passes the sample stage without being inelastically scattered the precession of the first region is exactly reversed in the second region with the opposite field \mathbf{B}_2 . If the neutron is part of an inelastic scattering process, the kinetic energy of the neutron differs as well as the time spent in the region of \mathbf{B}_2 . The polarisation of the neutron beam is either under- or overcompensated depending on the gain or loss in energy. As the initial polarisation is not fully restored, the measured intensity after the second polariser is reduced compared to the unscattered case. (Taken from ref. [40])

3.3.1 Mathematical Description of NSE

An incident neutron wave packet Ψ travelling along the y -axis, with an initial full polarization in x -direction $|+\rangle_x$ is considered. The constant magnetic field \mathbf{B}_1 is parallel to the z -axis, while \mathbf{B}_2 is antiparallel to the z -axis in region 2.

3.3 Classical Neutron Spin Echo (NSE)

It is noted that an eigenstate $|+\rangle_x$ of the spin operator σ_x with an eigenvalue 1 can be written as a superposition of the two eigenstates $|\pm\rangle_z$,

$$|+\rangle_x = \frac{1}{\sqrt{2}} (|+\rangle_z + |-\rangle_z) = \frac{1}{\sqrt{2}} \begin{bmatrix} 1 \\ 1 \end{bmatrix}_z, \quad (3.14)$$

where the top and bottom row of the bracket vector refer to the $|+\rangle_z$ -state and the $|-\rangle_z$ -state, respectively [41]. The neutron beam can be described by the plane wave approach and the wave function is then given by [42]

$$\Psi = e^{i(k_i y - \omega_i t)} \begin{bmatrix} 1 \\ 1 \end{bmatrix}. \quad (3.15)$$

As soon as a neutron with velocity v_i enters the first magnetic field region, the applied magnetic field can be described as a potential

$$\hbar\omega_z = \pm\mu B_1, \quad (3.16)$$

for the two incident spins. The \pm sign corresponds to the antiparallel and parallel spin components relative to the applied field. The resulting velocity of the two spins is

$$v_{\pm} = v_i \pm \frac{\hbar\omega_z}{mv_i}. \quad (3.17)$$

Due to the difference in velocity, the two opposite spin directions spend different times in the field region \mathbf{B}_1 . The two periods of time are approximated to the first order by

$$t_{\pm} = \frac{L}{v_{\pm}} = \frac{L}{v_i} \mp \frac{\hbar\omega_z L}{mv_i^3} = t_0 \mp \tau_{\text{NSE}}/2, \quad (3.18)$$

where t_0 is the median time of the two states spent in the region. The relative delay between the spin states after the passage of the length L at sample position is

$$\tau_{\text{NSE}} = \frac{2\hbar\omega_z L}{mv_i^3} = t_- - t_+. \quad (3.19)$$

The echotime τ_{NSE} is an important quantity for all spin echo variants, since the time difference between the two spin components is the varying parameter for such experiments, as it is shown later. Using equation (3.9), the phases picked up by the two spins while passing the magnetic field of the length L are

$$\phi_{\pm}^{(1)} = \pm\omega_z \frac{L}{v_i}. \quad (3.20)$$

Thus, after the passage through the first field region, the incident wave function equation (3.15) becomes

$$\Psi = e^{i(k_i y - \omega_i t)} \begin{bmatrix} e^{-i\omega_z L/v_i} \\ e^{i\omega_z L/v_i} \end{bmatrix}. \quad (3.21)$$

If the velocity of the neutron does not change, each spin receives the exact opposite change in phase on the passage through second region with $\mathbf{B}_2 = -\mathbf{B}_1$. However, if the neutron is scattered inelastically, the resulting change in velocity leads to a different phase picked up by the neutrons in the second region \mathbf{B}_2 ,

$$\phi_{\pm}^{(2)} = \mp \frac{\omega_z L}{v_i + \Delta v}, \quad (3.22)$$

where Δv denotes the change in velocity and the sign switch originates by the opposite magnetic field. The amplitude of the wave function of each spin is only proportional to the density of the scattering system at the corresponding time and place [43]

$$\Psi_{\pm} \propto \rho(r_i, t_{\pm}). \quad (3.23)$$

The spin state of a neutron, after region \mathbf{B}_1 (see equation (3.21)), that is scattered at position \mathbf{r}_i and time t_i with density $\rho(r_i, t_i)$, becomes [41, 42, 43]

$$\Psi_{sc} = e^{i(\mathbf{k}_f \mathbf{r} - \omega_f t)} \rho(\mathbf{r}_i, t_i) e^{i\mathbf{Q} \mathbf{r}_i} e^{i\omega t_i} \begin{bmatrix} e^{i\phi_+^{(1)}} \\ e^{i\phi_-^{(1)}} \end{bmatrix}, \quad (3.24)$$

where $\mathbf{Q} = \mathbf{k}_f - \mathbf{k}_i$, $\omega = \omega_f - \omega_i$ and $\phi_{\pm}^{(1)}$ as defined in equation (3.20). Including the passage through the second field region \mathbf{B}_2 , as described in equation (3.22), the total phase approximated to the first order becomes

$$\phi_{\text{tot}, \pm} = \pm \omega_z \frac{L}{v_i} \mp \frac{\omega_z L}{v_i + \Delta v} = \pm \omega \frac{\hbar \omega_z L}{m v_i^3} = \pm \omega \tau_{\text{NSE}}/2 \quad (3.25)$$

If one integrates over all possible scattering events, the wave function after region \mathbf{B}_2 becomes

$$\Psi_f = e^{i(k_f y - \omega_f t)} \left[\int dt_i \int d^3 r_i e^{i\omega t_i} e^{-i\mathbf{Q} \mathbf{r}_i} \rho(\mathbf{r}_i, t_i) e^{i\omega \tau_{\text{NSE}}/2} \right. \\ \left. \int dt_j \int d^3 r_j e^{i\omega t_j} \rho(\mathbf{r}_j, t_j) e^{-i\mathbf{Q} \mathbf{r}_j} e^{-i\omega \tau_{\text{NSE}}/2} \right]. \quad (3.26)$$

Thus, the expectation value of the x -polarisation at the position of the second polariser is

$$\langle \sigma_x \rangle \propto \langle \Psi_f | \sigma_x | \Psi_f \rangle = \\ \int d\omega \int d^3 r_i \int d^3 r_j \int dt_i \int dt_j \langle \rho(\mathbf{r}_i, t_i) \rho(\mathbf{r}_j, t_j) \rangle e^{i\omega(t_i - t_j)} e^{-i\mathbf{Q}(\mathbf{r}_j - \mathbf{r}_i)} e^{-i\omega \tau_{\text{NSE}}}, \quad (3.27)$$

where the integral over ω originates from the ensemble average of the density product. Since the second polariser filters for the x -polarisation, equation (3.27) describes the expected signal in the detector. In order to simplify equation (3.27), one introduces the relative coordinates $\mathbf{R} = \mathbf{r}_j - \mathbf{r}_i$ and the relative time $\tau = t_i - t_j$. The integral over $d\omega$ can be expressed as

$$\int d\omega e^{i\omega(\tau - \tau_{\text{NSE}})} = 2\pi \delta(\tau - \tau_{\text{NSE}}). \quad (3.28)$$

The polarisation can then be expressed as

$$\langle \sigma_x \rangle \propto \int dR^3 e^{-i\mathbf{Q}\mathbf{R}} \int d\tau \delta(\tau - \tau_{\text{NSE}}) \left[\int dt_i \int d^3r_i \langle \rho(\mathbf{r}_i, t_i) \rho(\mathbf{r}_i + \mathbf{R}, t_i + \tau) \rangle \right]. \quad (3.29)$$

The term in the square brackets is the van-Hove density-density correlation function G in dependence of the echotime τ_{NSE} , as described in equation (2.19). The final polarisation can be expressed as

$$\langle \sigma_x \rangle \propto \int dR^3 e^{-i\mathbf{Q}\mathbf{R}} G(\mathbf{R}, \tau_{\text{NSE}}). \quad (3.30)$$

The right side of equation (3.30) is the intermediate scattering function, as defined in equation (2.18), which is the spatial Fourier transformed of the van-Hove correlation function $G(\mathbf{R}, \tau_{\text{NSE}})$. Although the measured quantity $\langle \sigma_x \rangle$ is a sum of scattering events with different energy transfers ω , only pairs of scattering events occurring at $(t_i - t_j) = \tau_{\text{NSE}}$ contribute to this quantity. A more detailed explanation can be found in Ref. [41].

Experimentally, one usually chooses a set of echotimes τ_{NSE} by varying the magnetic field strengths $\mathbf{B}_1, \mathbf{B}_2$. By measuring the final polarisations as a function of the set of echotimes τ_{NSE} , one obtains the intermediate scattering function.

3.4 Neutron Resonance Spin Echo

The Neutron Resonance Spin Echo (NRSE) is a variant of NSE. NRSE follows a similar working principle as NSE, but each constant field region is replaced by a pair of radio frequency (RF) spin flipper. Each RF-flipper is superimposed by a constant magnetic field, which is limited to the vicinity with width d . Depending on the magnetic field direction relative to the neutron beam one distinguishes between transversal and longitudinal NRSE. In the transversal NRSE the constant field is perpendicular to the neutron flight path, while in the longitudinal case the field is parallel. In case of transversal NRSE, the space between the RF-flipper and the area in the vicinity has to be field free, which is realised by μ -metal shielding. The basic, transversal NRSE setup is illustrated in figure 3.4.

Likewise in NSE, the first pair of RF flippers separates the phase of opposite spins in z -projection of the x -polarised neutron beam. The second pair aligns the phase of the two spins back together. Any inelastic interaction of the neutron with the sample results in an additional phase between the two spin components. As a consequence, the second arm does not fully restore the two spin states and the difference in phase results in a reduced intensity after passing the second polariser. The echotime in this setup is doubled compared to classical NSE with same constant magnetic field strength, $\tau_{\text{NRSE}} = 2\tau_{\text{NSE}}$.

A full derivation of NRSE can be found in [41, 42, 43] and only the key equations, which are required for the subsequent formulation of MIEZE, are stated here. In particular, the change of polarisation is described, that is induced by a single RF-coil in a constant field.

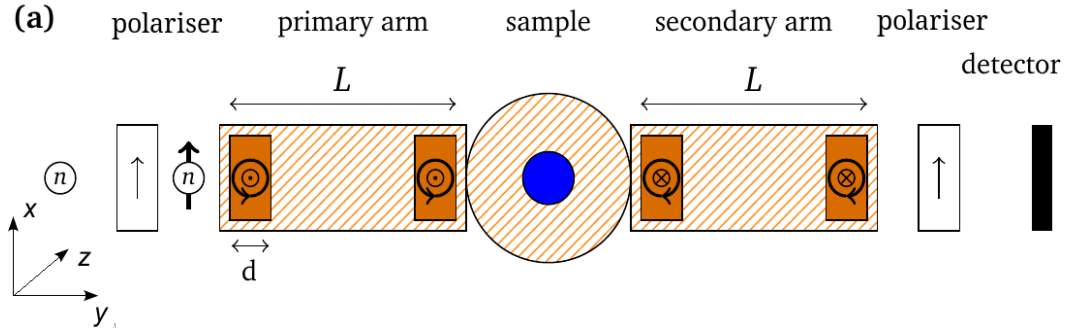


Figure 3.4: Illustration of a NRSE instrument. A neutron beam is polarised and passes through the two arms of a NRSE and the second polariser towards the detector. The two NRSE arms are opposite in their constant magnetic fields B_z and rotating magnetic field B_{rf} . Each arm consists of two RF-flipper which are embedded in zero-field regions. The area in the vicinity sample stage is field free as well. Adapted from ref. [44].

3.4.1 Passage through a RF-flipper

A RF-flipper combines two magnetic fields within a region of width d : A constant field B_z in z -direction orthogonal to the incident neutron polarisation and an oscillating field B_{rf} , that rotates around the constant field vector in the x, y -plane. The resulting magnetic field vector is

$$\mathbf{B} = \begin{pmatrix} B_{rf} \cos \omega_s t \\ B_{rf} \sin \omega_s t \\ B_z \end{pmatrix}. \quad (3.31)$$

The frequency ω_s is the frequency of the oscillating field. The wave function of a neutron travelling through a magnetic field can be described by the Schrödinger equation

$$\begin{aligned} i \frac{\partial \Psi}{\partial t} &= -\frac{\partial^2 \Psi}{\partial y^2} + \boldsymbol{\sigma} \mathbf{B} \cdot \Psi \\ &= -\frac{\partial^2 \Psi}{\partial y^2} + \begin{bmatrix} \omega_z & \omega_{rf} e^{-i\omega_s t} \\ \omega_{rf} e^{i\omega_s t} & \omega_z \end{bmatrix} \cdot \Psi, \end{aligned} \quad (3.32)$$

where $\hbar\omega_{rf,z} = \mu B_{rf,z}$ are the potentials induced by B_{rf} and B_z , respectively. Similar to section 3.3 the components parallel (+) and antiparallel (-) to B_z are treated separately

$$\Psi = \begin{bmatrix} \Psi^+ \\ \Psi^- \end{bmatrix}, \quad (3.33)$$

and equation (3.32) becomes a coupled differential equation for the two spins

$$i \frac{\partial \Psi^\pm}{\partial t} = -\frac{\partial^2 \Psi^\pm}{\partial y^2} \pm \omega_z \Psi^\pm + \omega_{rf} e^{\mp i\omega_s t} \Psi^\mp. \quad (3.34)$$

This equation is well known as Krüger's problem, which is solved by transforming the problem into a rotating coordinate system of the precessing neutron [45]. The frequency of the rotating field ω_s is chosen such that it is resonant to the Larmor frequency $\omega_L = \omega_s = \gamma B_z = 2\omega_z$ induced by the constant field B_z . Thus, the field B_{rf} is fixed in the rotating frame of the neutron spin. The field strength of B_{rf} is chosen such that the passing neutron experiences exactly a π -flip

$$2\omega_{rf} \cdot d/v = \pi \quad (3.35)$$

in the rotating frame. Since the π -flip is performed on top of the Larmor precession, the accumulated phase is doubled compared to classical NSE. Taking the resonance and π -flip condition into account, the incident wave function with the initial polarisation α^\pm

$$\Psi_{in} = \frac{1}{\sqrt{2}} \begin{bmatrix} \alpha^+ \\ \alpha^- \end{bmatrix} e^{i(k_0 y - \omega_0 t)}, \quad (3.36)$$

becomes after passing the RF-flipper of width d ,

$$\Psi_{RF} = \frac{-i}{\sqrt{2}} \begin{bmatrix} \alpha^- e^{i\Theta(y)} \\ \alpha^+ e^{-i\Theta(y)} \end{bmatrix} e^{i(k_0 y - \omega_0 t)}, \quad (3.37)$$

with the phase

$$\Theta(y) = \omega_L \left[\frac{(y - \frac{d}{2})}{v} - t \right]. \quad (3.38)$$

A detailed derivation can be found in ref. [42]. It is noted that the initial polarisation α^\pm is switched after the passage through one RF-flipper. The inversion of the population of the spin components originates from the resonant and π flip condition. Thus, the initially parallel component of the spin becomes the antiparallel component and vice versa. However, the switch of initial polarisation cancels after the passage of a second coil. The expected polarisation in x -direction becomes

$$\langle \sigma_x \rangle = \cos \left\{ 2\omega_L \left[\frac{y - \frac{d}{2}}{v} - t \right] \right\}. \quad (3.39)$$

The spin precesses with a frequency of $2\omega_L$ time and with $2\omega_L/v$ in space. Quantum mechanically, the two initial spin states $\sigma_z = \pm 1$ receive a change in kinetic energy by $\pm\omega_L$, due to the magnetic potential. The passage of the second RF-flipper under the same conditions doubles the effect. The resulting echotime is

$$\tau_{NRSE} = \frac{4\hbar\omega_z(L + d)}{mv_i^3}, \quad (3.40)$$

with the distance between the two RF-flippers L , and the mass m and initial velocity v_i of the neutron. Thus, the range of τ_{NRSE} is doubled compared to NSE with same constant fields [7, 43]. However, although NRSE is more efficient than NSE, until today the accessible range in τ_{NSE} of NSE is still higher than in τ_{NRSE} of NRSE. The limiting factor is hereby the high frequencies ω_s of the rotating field B_{rf} , that are needed for the same performance, which are not realised yet.

3.5 Modulation of Intensity with Zero Effort (MIEZE)

Modulation of Intensity with Zero Effort (MIEZE) is a variation of NRSE, where the second pair of RF-flippers after the sample becomes obsolete. One great benefit of the MIEZE technique is that the complete neutron spin manipulation happens in front of the sample. In contrast to NSE and NRSE, MIEZE is independent of depolarising properties of the sample and the sample environment.

The MIEZE principle also uses two RF-flipper in front of the sample stage, but, different to NRSE, the second flipper is driven with a higher frequency compared to the first. Likewise NRSE, the two spin components antiparallel and parallel to the constant field are separated kinetically by the first RF-flipper. The second RF-flipper utilises the fact that the RF-flipper also switches the initial spin components. Thereby the initially slower component becomes the faster one and vice versa. Since the second coil is driven at a higher frequency the kinetic energy of the slower spin is overcompensated and starts "catching up". Thus two spin components, which were separated by the first RF-flipper, come back together and interfere after a certain distance, similar to a Michelson interferometer. The point of interference depends on the relative frequency and distance of the two RF flippers and defines the MIEZE condition (equation (4.2)). If one places a second polariser after the primary arm, one measures an oscillating intensity in time at the point of interference. The oscillating signal defines the *contrast* C , which is the ratio of the amplitude to the average signal, and is ideally $C = 1$. If the neutron beam is scattered inelastically the two spin components do not come completely back together and contrast is reduced. The change in contrast is direct proportional to the intermediate scattering function and by that one obtains information of the transferred energy [11]. The schematic of the MIEZE setup is illustrated in figure 3.5.

The influence of the first coil on the spin components was deduced in section 3.4. For the description of the influence of the second coil, one transforms the output of the first coil into the coordinate system, where the entrance of the second coil is defined as zero [42]:

$$y = y' + L_1 = y' + L + d, \quad (3.41)$$

where d is the width of the RF-flipper and L is the distance between the two flippers. The distance between the two centres of the RF-flipper is $L_1 = L + d$. The input into the second coil is then

$$\Psi_{\text{in},2} = -\frac{i}{\sqrt{2}} e^{i(k_0(y'+L_1)-\omega_0 t)} \begin{bmatrix} \alpha^- e^{i\omega_A L/v} e^{i\Theta'(y')} \\ \alpha^+ e^{-i\omega_A L/v} e^{-i\Theta'(y')} \end{bmatrix}. \quad (3.42)$$

with the phase as in equation (3.38) transformed into the new coordinate system

$$\Theta(y) = \omega_A \frac{L}{v} + \Theta'(y') = \omega_A \frac{L}{v} + \omega_A \left[\frac{(y' + \frac{d}{2})}{v} - t \right], \quad (3.43)$$

where ω_A is the RF frequency in the first coil, equivalent to ω_s in NRSE. For the passage through the second coil, one uses equation (3.36) and equation (3.37), but with $\omega_A \rightarrow \omega_B$,

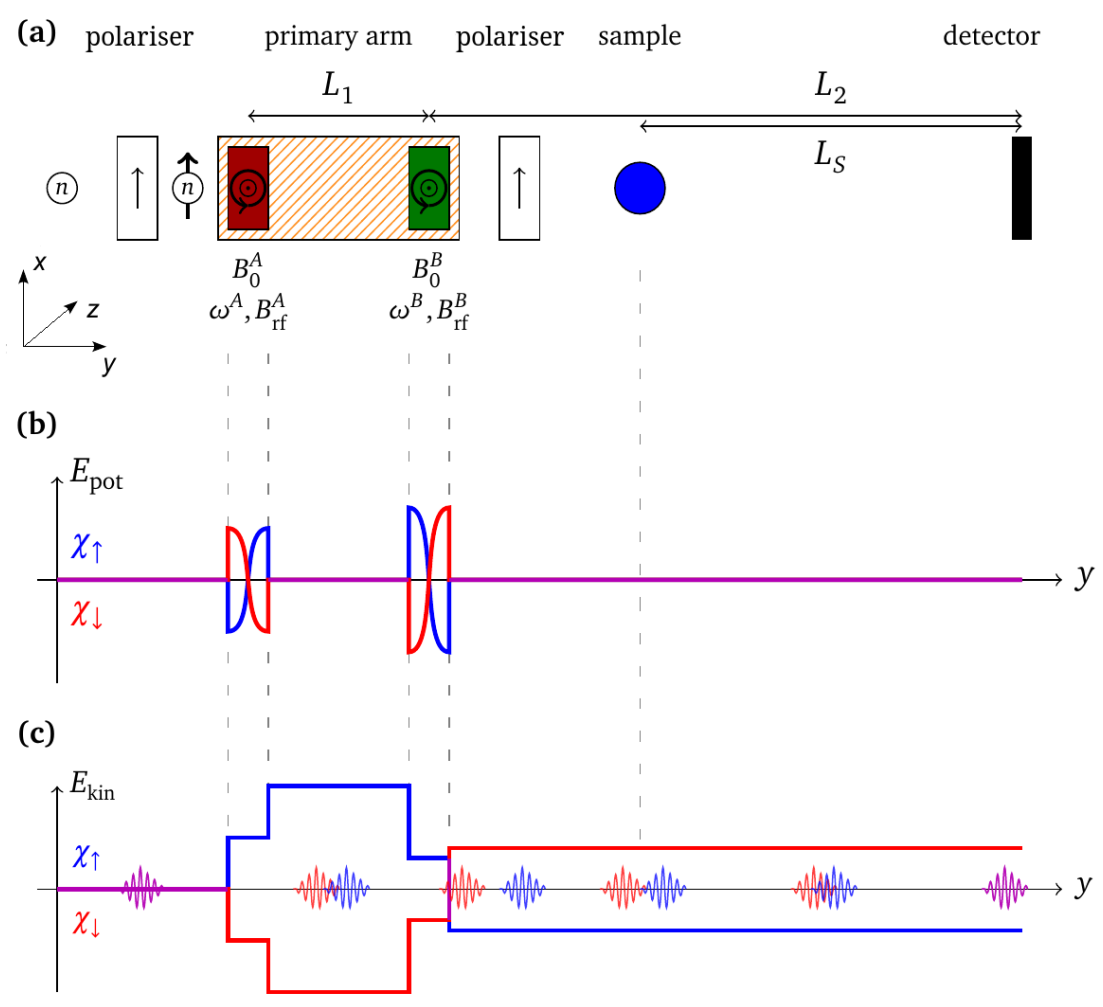


Figure 3.5: The MIEZE principle. a) shows a general MIEZE setup b) gives the potential induced by the RF coils experienced by the different spin states c) is the resulting difference in kinetic energy and illustrates the separation of the spin components. An incident polarised neutron beam passes two RF flipper, driven at different frequencies ω_A, ω_B and different constant fields B_0^A, B_0^B . While passing the first RF flipper, the parallel and antiparallel spin components experience different potentials resulting into a difference in kinetic energy. The two spin components separate until it is overcompensated by the the second RF flipper. The spin components get back together and interfere at detector position. By placing a polariser after the second RF flipper one measures an oscillating intensity. Taken from ref. [40]

where ω_B is the frequency of the second coil. The output after the second coil is then given by,

$$\Psi_{\text{out},2} = \frac{1}{\sqrt{2}} e^{i(k_0 y' - \omega_0 t)} \begin{bmatrix} \alpha^+ e^{i\Phi(y')} \\ \alpha^- e^{-i\Phi(y')} \end{bmatrix}, \quad (3.44)$$

where

$$\Phi = \frac{\Delta\omega y'}{v} - \Delta\omega t - \frac{\omega_A L}{v} - \frac{\Omega d}{v}, \quad (3.45)$$

with

$$\Delta\omega = \omega_B - \omega_A; \quad \Omega = (\omega_B - \omega_A)/2. \quad (3.46)$$

The ideal location for the detector is chosen such that $\langle\sigma\rangle$ is independent of the neutron velocity to equalize the contribution of all neutrons. Equation (3.45) shows that all terms depending on the velocity cancel out if

$$\frac{\Delta\omega y'}{v} - \frac{\omega_A L}{v} - \frac{\Omega d}{v} = 0. \quad (3.47)$$

With the distance between the entrance of the first and the exit of the second coil $L_1 = L + d$, the distance from the second coil to the detector is $L_2 = y' - \frac{d}{2}$ and from equation (3.47) one gets

$$\frac{\omega_B}{\omega_A} = \frac{L_1 + L_2}{L_2}. \quad (3.48)$$

Equation (3.48) is known as the MIEZE condition. If the MIEZE condition is fulfilled, both wave packets interfere independently of the neutron velocity and the wave function at the detector position becomes simply

$$\Psi = \Psi_{\text{in}} \begin{bmatrix} e^{-i\Delta\omega t} \\ e^{i\Delta\omega t} \end{bmatrix}, \quad (3.49)$$

with Ψ_{in} defined in equation (3.36). The beam intensity measured by the detector is then

$$|\Psi|^2 \propto \frac{1 + \cos 2\Delta\omega t}{2}. \quad (3.50)$$

From equation (3.50) one can extract the contrast

$$C = \frac{\max_t |\Psi|^2 - \min_t |\Psi|^2}{2 \langle |\Psi|^2 \rangle_t}. \quad (3.51)$$

As $|\Psi|^2$ oscillates over time, $\max_t |\Psi|^2 - \min_t |\Psi|^2$ is the amplitude of the oscillation and $\langle |\Psi|^2 \rangle_t$ is the average intensity. The contrast C is the equivalent quantity to the polarisation in NSE. As well as in NSE, the contrast decreases if neutrons are inelastically scattered. Assuming again a small energy transfer at a point \mathbf{r}_i at time t_i , it follows that the contrast C is proportional to the intermediate scattering function $I(\mathbf{Q}, \omega)$. The

echotime τ_{MIEZE} is equivalent to τ_{NSE} and describes the time separation of the spin states at the sample position. It is given by [11]

$$\tau_{\text{MIEZE}} = (\omega_B - \omega_A) \frac{4\hbar L_s}{mv^3} \quad (3.52)$$

with the distance from sample to detector being L_s . This echotime τ_{MIEZE} is determined by the combination of frequencies ω_A, ω_B in the two coils, while the MIEZE condition has to be kept satisfied.

When performing measurements, a defined set of MIEZE echotimes τ_{MIEZE} is applied to measure the contrast $C(\tau_{\text{MIEZE}})$ for each τ_{MIEZE} . The relative loss of contrast of a neutron beam as a function of τ_{MIEZE} is direct proportional to the intermediate scattering function $I(\mathbf{Q}, \omega)$.

3.6 Reduction Factor

The disadvantage of a time-of-flight technique like MIEZE is that the efficiency of this method is limited in resolution due to deviations from the optimal flight path. A deviation of the optimal flight path disturbs the MIEZE condition and leads to a reduction in the contrast that does not originate from a sample. The spatial mean width of the MIEZE condition is given by [11, 43]

$$\Delta_{\text{MIEZE}} = \frac{\pi v}{\frac{\delta v}{v} 4(\omega_B - \omega_A)}, \quad (3.53)$$

where v is the neutron velocity, δv is the mean width of the velocity distribution and $(\omega_B - \omega_A)$ is the difference in frequency between the two coil sets. With increasing echotime τ_{MIEZE} , the width in space where the MIEZE condition is valid becomes narrower and the contrast reduction of a non-optimal flightpath significant. If the contrast falls below $\lesssim 20\%$ the measurement loses its validity, since statistical factors become too dominant.

There are three different factors within the setup which reduce the contrast. These factors are denoted as

$$C = R_{\text{flipper}} \cdot R_{\text{geometry}}(g, \theta_s, \Lambda) \cdot R_{\text{detector}}(\theta_D, \Lambda) \cdot C_0. \quad (3.54)$$

R_{flipper} is mainly determined by the flipping efficiency of the $\pi/2$ -flipper coils.

For R_{geometry} there are two contributions: The instrument geometry and the geometric shape of the sample. The quantity g corresponds to the geometric shape of the sample, $\Lambda = 2\pi v / \Delta\omega$ is the distance a neutron with velocity v travelled over one period $2\pi / \Delta\omega$ and θ_D is the detector angle with respect to the plane of \mathbf{k}_f [46]. In scope of this work only sample shapes of disk and square plates are considered, since those are the sample shapes that were used for the experiments described later. The influence of the other shapes in MIEZE are described by [46] in detail. One should notice, that in the references [46, 47] the detector angle $\theta_D = 0$ is defined as perpendicular to \mathbf{k}_i . However, in the following, the detector angle $\theta_D = 0$ is defined as perpendicular to \mathbf{k}_f for practical reason. Hence $\theta_D \rightarrow \theta_D + 2\theta_D$ compared to the references [46, 47].

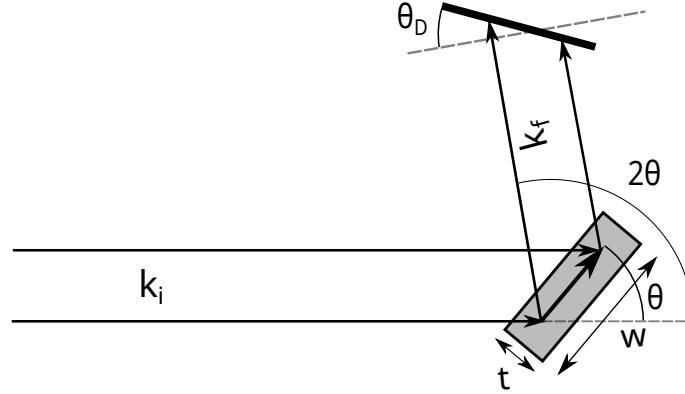


Figure 3.6: Scattering geometry. The neutrons impinge on a square-plate shaped sample with dimensions ($w \times t \times h$) with an angle θ with respect to the incident neutron beam. The neutron beam scatters with an angle of 2θ towards the detector. The detector is tilted by an angle θ_D with respect to the plane of \mathbf{k}_f .

Considering a parallel beam as in figure 3.6, if the beam gets scattered at an arbitrary point \mathbf{r} off the centre under an angle θ , the change in path length as a function of the scattering angle θ and the detector angle θ_D becomes

$$\Delta L_2 = x - \frac{x \cos(2\theta + \theta_D) + y \sin(2\theta + \theta_D)}{\cos(\theta_D)}, \quad (3.55)$$

with x and y being the components of the vector \mathbf{r} . The resulting difference in phase at the detector position is given by

$$\Delta\phi = 2\pi \frac{\Delta L_2}{\Lambda}. \quad (3.56)$$

The total geometric reduction of contrast is obtained by averaging over all possible scattering points inside the sample [47]

$$R_{\text{geometry}} = \frac{\int_{-t/2}^{t/2} \int_{-w/2}^{w/2} \cos(\Delta\phi) dy dx}{w \cdot t}, \quad (3.57)$$

where t is the sample thickness, w is the sample width. For a plate-like sample the reduction factor becomes [47]

$$R_{\text{square}} = \text{sinc} \left(\frac{\pi w}{\Lambda} \left[-\sin \theta - \frac{\sin(\theta_D + \theta)}{\cos(\theta_D)} \right] \right) \times \text{sinc} \left(\frac{\pi t}{\Lambda} \left[-\cos \theta + \frac{\cos(\theta_D + \theta)}{\cos(\theta_D)} \right] \right). \quad (3.58)$$

The reduction factor of the sample R_{square} can be maximised for both terms [47]. The first maximum of the first term lies at

$$\theta_{D,\text{opt1}} = \arctan\left(\frac{1 - \cos 2\theta}{\sin 2\theta - \tan \theta}\right) - 2\theta, \quad (3.59)$$

and maximum of the second terms at

$$\theta_{D,\text{opt2}} = \arctan\left(\frac{\tan \theta (1 - \cos 2\theta)}{\tan \theta \sin 2\theta + 1}\right) - 2\theta. \quad (3.60)$$

Although both terms cannot be satisfied simultaneously, changing the detector angle in a way that the dominating term gets maximised the loss in contrast due to instrumental and sample geometry can be minimised. Thus, for performing measurements which are not in forward scattering geometry, it is necessary to rotate the detector, especially for increasing MIEZE times.

The reduction factor of the detector originates from the path length differences inside the detector foils. The corresponding reduction factor is [47]

$$R_{\text{detector}} = \text{sinc}\left(\frac{\epsilon\pi}{\Lambda \cos(2\theta - \theta_D)}\right), \quad (3.61)$$

where ϵ is the thickness of the detector.

If applying MIEZE on a triple axis instrument, the analyser leads to an additional reduction factor. R_{analyser} is treated exactly like a sample, with corresponding properties.

3.7 MIEZETOP setup

The MIEZE setup uses RF-flippers, where a static field and a resonant oscillating field are superimposed. Since the change in phase in the vicinity of the RF-flipper should be equal for all neutrons over the beam crosssection, highly homogeneous fields, well-defined field borders and a zero-field region between the RF-flippers are required. The realisation of these condition is difficult and the application of high susceptibility materials, like μ -metal, is necessary.

RESEDA was the first beamline using an alternative approach by switching from static fields perpendicular to the beam (transversal MIEZE/NRSE) to static fields along the neutron beam (longitudinal MIEZE) [37]. As a consequence the initial neutron polarisation has to be along the beam direction as well. One of the major advantages lies in the symmetry of the static field coils and the π -flip of the neutron when passing one resonant flipper, as described in section 3.4.1. Any spin rotation which is induced by the static magnetic field before the RF-flipper is exactly reversed after the RF-flipper from the perspective of neutrons. By that it is no longer necessary to have well-defined field borders or a homogeneous static field as long as it is symmetric. The same arguments are valid for neutrons with a deviation from the beam centre: Any stray fields induced by B_0 perpendicular to the neutron beam before the RF-coil are inverted thereafter. This self correction simplifies the setup of the longitudinal MIEZE drastically compared to

the transversal one. The mathematical description remains unchanged, since any change in phase that was assumed to be zero before and after the RF-flipper in the transversal setup exactly cancels in the longitudinal setup. The MIEZETOP setup applied at MIRA is shown in figure 3.7.

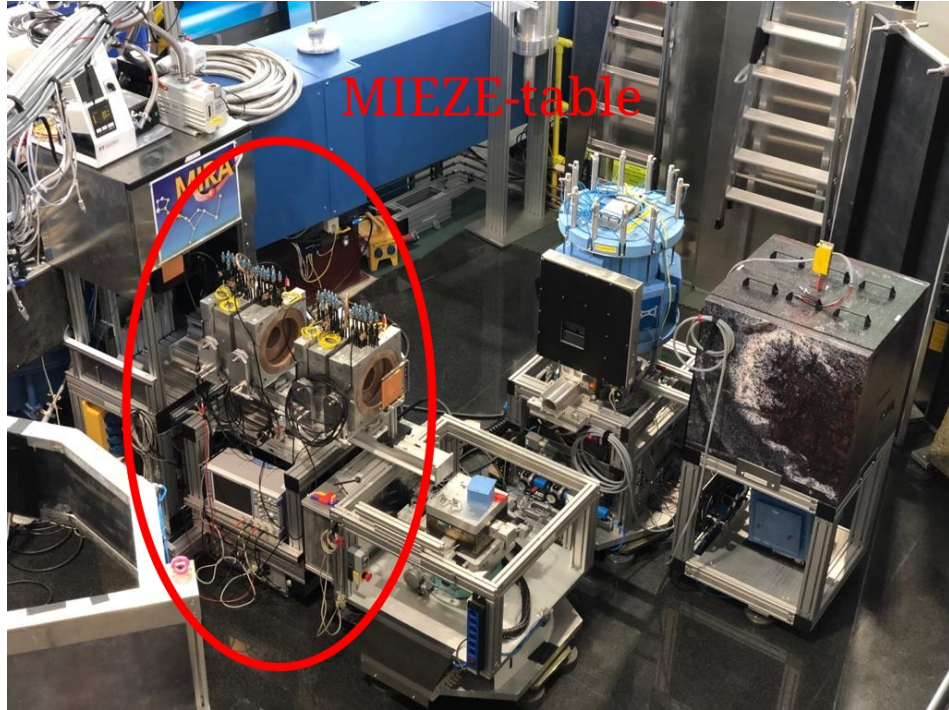


Figure 3.7: The complete MIEZETOP setup. The MIEZE-table (red circle) is integrated into MIRA.

In the following subsections all components used in the MIEZE setup are described, such as electronic equipment, detector system and polarisation analysers. Thereafter the setup as a whole is described. The circuit plan and the description of the electronic devices can be found in appendix A.

3.7.1 The instrument MIRA

MIRA is a TAS instrument. The main configuration is a cold three axes spectrometer, whose wavelengths range $3.5 \text{ \AA} < \lambda < 6 \text{ \AA}$, which corresponds to $1.2 \text{ \AA}^{-1} < k < 1.6 \text{ \AA}^{-1}$ and energy transfers from $-6 \text{ meV} < \Delta E < 3 \text{ meV}$ can be reached. As a monochromator crystal pyrolytic graphite is chosen. PG has a layered hexagonal structure ordered in the (001) plane, while the other orientation of the planes in the other directions is random. Positive values refer to the energy gain of the measured system and negative accordingly to the energy loss.

All measurements can be performed with polarised or unpolarised neutrons. MIRA has two available detectors: A finger detector with a very low background of less than 0.1 cps

and a 6-foils 2D position and time sensitive CASCADE detector. Currently two add-ons are under development: A small 3D spherical polarisation analysis device (MiniPAD) and the MIEZETOP presented in this thesis.

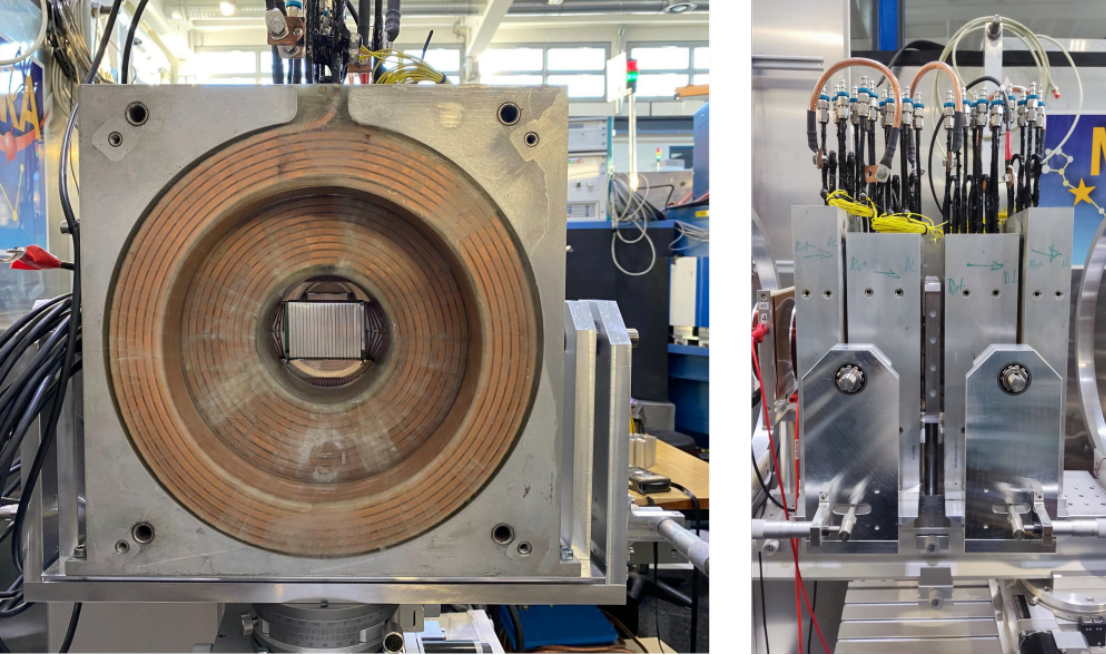


Figure 3.8: Front (left) and side (right) view of the B_0 coils in Helmholtz configuration. The inner pair defines the magnetic field in the vicinity of the RF-flipper (centre). The outer pair are connected inverse to reduce the range of the magnetic field.

3.7.2 B_0 Coil System

The coil set shares a similar design as the one used at RESEDA [37], and are shown in figure 3.8. The B_0 coil system consists of two pairs of coils, an inner pair and an outer pair. Both pairs are used in the Helmholtz configuration, where the distance between the coils is $d_{\text{Helmholtz}} = R_{\text{coil}}$ in order to create a constant field between a pair of coils. The wire has a square cross-section with a side length of 5 mm. Inside the wire is a 3 mm diameter hollow space, which allows the application of water cooling. The wire is cast into epoxy.

The inner coil pair has 168 windings ordered in 12×14 . The width is $w = 86$ mm and the inner radius is $r = 87$ mm. The outer coil pair has 48 windings ordered in 8×6 . The width is $w = 50$ mm and the inner radius is $r = 130$ mm. The coils are placed on a two-angle rotator to adjust the magnetic axis of the coil to the beam axis.

The inner coil pair produces a magnetic field downstream the neutron beam and acts as constant field in the longitudinal MIEZE setup. The outer pair of coils produces a static magnetic field opposite to the inner pair, but with a order of magnitude weaker.

The outer pair functions as *cut-off* coils by faster decreasing the magnetic field outside the coil system.

3.7.3 RF-coil

The RF-coil is the key component of the MIEZE setup. In NRSE or MIEZE the static field B_0 is combined with a rotating RF field, which constitute together the RF-flipper. Since a rotating field is rather difficult to realise, one uses a linearly oscillating field, which can be decomposed into two counter-rotating fields. In the rotating coordinate system, the first field component is static, the second rotates with twice the frequency. The linear combination of the second component and the static field B_0 , results in an effective field $B_{0,\text{eff}}$. This effect, referred to as the Bloch-Siegert shift, leads to a small shift of the

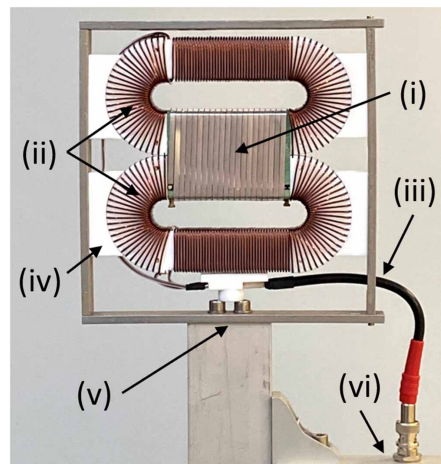


Figure 3.9: Radio frequency coil used for the NSE coils. (i) Main coil, (ii) compensation coils, (iii) high voltage connector, (iv) Teflon holders, (v) aluminum support and frame (vi) small c-box. The design was developed by RESEDA and the figure was obtained from [48].

resonance frequency due to the new effective field. It is negligible for cold neutrons and frequencies of 50 kHz and above [49], but reduces the contrast for lower frequencies.

In order to prevent any static perturbations of the static field and reducing the power loss, one has to minimise the stray fields of the RF-flipper [50]. This is realised by guiding back the magnetic flux in form of two closed loops. Figure 3.9 shows a completely assembled RF-coil. The original design was developed for the instrument RESEDA [48].

The body of the main coil is made of glass-fibre reinforced plastic (GRP) and the body for the loops is made of Teflon. The flat wire, where the neutrons pass, is made of 99.5% pure, uncoated aluminium, in order to reduce disturbing incoherent scattering. The loops are made of high frequency (HF) copper wire to avoid heat production at higher frequencies due to the skin effect. The Al band and the HF filament at the end of the neutron window frame are connected by soldering tags.



Figure 3.10: A $\pi/2$ -flipper consists of two perpendicular magnetic fields. The vertical field is generated by a rectangular Al coil. The horizontal field is generated by a Helmholtz configuration.

3.7.4 $\pi/2$ -flipper

The $\pi/2$ -flipper consists of two orthogonal fields of the same strength, one parallel to the beam and one perpendicular to the beam. The magnetic field along the beam direction is realised by a Helmholtz configuration (hsf). The magnetic field perpendicular to beam is realised by a flat rectangular coil made of Al wire (sf), such that the neutrons can pass through the coil.

By superposition of both orthogonal fields with same strength, the effective field points by an angle of 45° with respect to the neutron beam. The strength of the effective field is chosen such that the spin rotates exactly by π around the effective field vector. A neutron which is initially polarised along the beam direction receives a π -rotation around a vector with an angle of 45° with respect to the initial spin direction. By that polarisation of the neutron beam receives effectively $\pi/2$ -flip in respect to the initial one.

In order to preserve the polarisation, a guide field is indispensable. Otherwise magnetic field of the earth or other weak stray fields disturb the polarisation. Since it is very difficult to change the polarisation in a small space by 90° without any disturbance, it is easier to involve the guide field into the spin-flip procedure. Therefore the Helmholtz setup is not only a crucial part of the flipping process, it further acts as a guide field.

3.7.5 Polariser

To polarise the neutron beam, a supermirror bender manufactured by Swiss Neutronics was used. A supermirror polariser consists of a stack of silicon wavers coated with Fe/Si multilayers. This multilayer systems is magnetised and placed in the neutron trajectory.

At the interfaces of this magnetised multilayer system the spin components parallel and antiparallel experience different potentials. Consequently, the total reflection edge

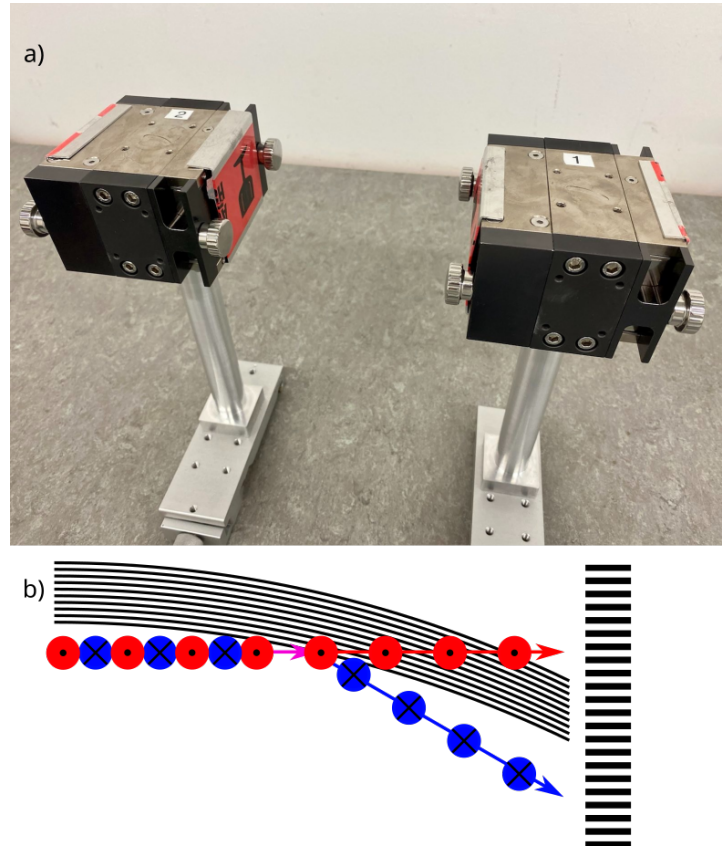


Figure 3.11: a) Picture of the used polarisers. b) Principle of the of a solid state polariser. An unpolarised neutron beam impinges on magnetised Fe/Si multilayers. Due to the different total reflection edges, the unwanted spin component is reflected away, while the other spin component is transmitted. The collimator after the multilayered system absorbs the reflected component.

of the neutron beam differs for the spin components parallel and antiparallel to the magnetisation of the coated wavers. This difference is utilised by choosing a small angle between the wavers and the beam such that one spin component gets reflected away from the beam path, while the other one is transmitted. The multilayer system is followed by a collimator, that absorbs the reflected neutrons.

The polariser that was used in the later described experiments achieved a polarisation $> 95\%$. The resulting polarisation is perpendicular to the neutron beam, guided by the strong magnetic dipole field $B_{\text{center}} \approx 500 \text{ G}$ of the polariser. The polarisers and their working principle is shown in figure 3.11.

3.7.6 Detector

A MIEZE signal is a high-frequency modulation of intensity, which has to be measured at a specific distance after the RF-coils. Therefore, the detector has to be able of detect the

neutrons precisely in space and time.

The CASCADE neutron detector consists of 6 gas electron multiplier (GEM) foils, which transport and amplify charges in the counting gas. The total absolute detection efficiency is for cold neutrons around $\approx 30\%$ (5% for each foil). The detector covers a position sensitive area of $20 \times 20 \text{ cm}^2$ and has a readout structure with 128×128 pixels. The lateral pixel size is therefore 1.56 mm. The single conversion foils are $\approx 1 \mu\text{m}$ thick. The maximum time resolution per time-channel is 100 ns (10 MHz). The detector is operated such that it measures 16 frames per oscillating intensity period.

4 First measurements of MIEZETOP

The following measurements with the MIEZETOP setup (see figure 3.7) took place in autumn 2018 and in spring 2020. The first period was used for characterising the coils and to test all components in operation. The first oscillating MIEZE signal was measured. In the second period, newly implemented modifications and, subsequently, the applicability of MIEZE in diffraction and triple axis mode were tested. Since then, the reactor operation is unexpectedly paused, which made it impossible to conduct any further experiments.

4.1 MIEZE Setup

The MIEZE setup, as shown in figure 3.7, has to be optimised such that the accessible range of echotime τ_{MIEZE} is maximised, without violating the MIEZE condition given by equation (3.48). The echotime τ_{MIEZE} as defined in equation (3.52) depends on the difference of the frequencies of both RF-flippers

$$\tau_{\text{MIEZE}} = (\omega_B - \omega_A) \frac{4\hbar L_s}{mv^3}, \quad (4.1)$$

where $\omega_{A,B}$ are the frequencies of the RF-flippers, L_s the sample detector distance and v the neutron velocity. Since the applicable frequencies $\omega_{A,B}$ have technically an upper limit, the distances between the components of the setup have to be optimised to achieve the maximal range. If one inserts the MIEZE condition

$$\frac{\omega_B}{\omega_A} = \frac{L_1 + L_2}{L_2}, \quad (4.2)$$

into equation (4.1), it becomes

$$\tau_{\text{MIEZE}} = \frac{L_1}{L_2} \omega_A \frac{4\hbar L_s}{mv^3}. \quad (4.3)$$

For limited applicable frequencies, L_1/L_2 and L_s have to be maximised in order to increase the maximal range in τ_{MIEZE} . The physical limits of the ratio L_1/L_2 are mainly determined by the available space at the beamline, without reducing the flexibility of the scattering angles of MIRA and, hence, the available \mathbf{Q} range. Bearing in mind that MIEZETOP should act as an easily exchangeable addition to the TAS, the already existing setup should not be drastically altered. Thus, any rearrangement of components should be restricted to the MIEZE-table, which is shown figure 3.7. The resulting distances are shown in figure 4.1.

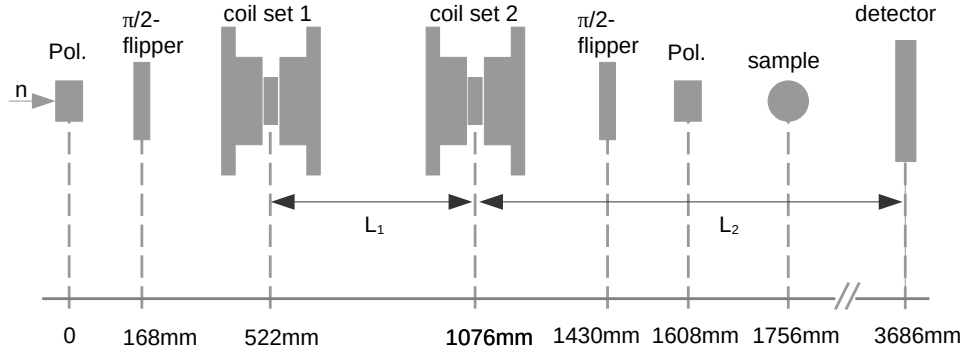


Figure 4.1: Schematic of the MIEZETOP setup. The position of each component is labelled with the distance to the first polariser as reference. L_1 and L_2 are the distances, that determine the MIEZE condition.

4.2 Characterisation of the MIEZE components and Tuning of the Echotimes

The oscillating magnetic field B_{rf} of the RF-flipper has to be chosen such that a passing neutron performs exactly a π -flip, as described in section 3.4. To determine the necessary field strength of B_{rf} , firstly, one applies an arbitrary magnetic field in the B_0 coils, sets the frequency f_L of the oscillating field to resonant condition and measures the neutron counts versus B_{rf} . With increasing B_{rf} , the polarisation of the neutron beam starts rotating and the measured intensity decreases, as the second polariser selects only one spin component. At minimum intensity, the polarisation of the neutron beam is exactly changed by π .

However, in order to minimise external disturbances of this adjustment process, the chosen field B_0 has to be high enough to avoid the influence of the Bloch-Siegert shift. On the other hand, the applied frequency should be low enough such that parasitic effects, e.g. of the coaxial cable, do not damp or disturb the amplitude of the resonant circuit. The applied field was $B_0 \approx 48$ G and the corresponding Larmor frequency is $f_L = 88$ kHz. The corresponding scan is shown figure 4.2 a), for technical simplicity, the applied RF-voltage was scanned and the minimum is found at $U_{B_{rf}} = 1.55$ V. Since the necessary field strength of B_{rf} only depends on the neutron velocity, it is kept - likewise the neutron velocity - constant over the whole experiment.

Since in MIEZE experiments, one measures the contrast in dependence of the echotime τ_{MIEZE} , one has to determine a set of echotimes *a priori*. Each echotime has two different resonant frequencies in the respective RF-flipper, which have to be optimised, in order to obtain the maximal contrast. To ensure that the calculated resonant condition is at an optimum, the B_0 field is scanned, while f_L and B_{rf} are kept fixed. Due to the same

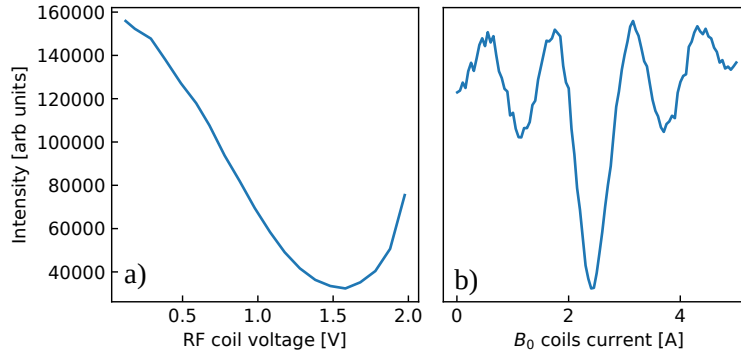


Figure 4.2: Determination of the magnetic fields for the $\pi/2$ flip condition in the RF coil. The RF coil voltage versus the intensity (a) and the current of the B_0 coil versus intensity (b). The minimum intensity gives a flipping voltage of $U_{B_{rf}} = 1.55$ V. The resonant flipping current is $I_{B_0} = 2.3$ A correspondingly. The fluctuations in the right figure originate from the dense steps and the lower counting time compared to the left figure.

reason as for the adjustment of B_{rf} , the resonant condition is optimised in the minimum of the measured intensity. This adjustment of the resonant condition has to be repeated for every applied eigenfrequency of the RF-flipper. Figure 4.2 b) shows an exemplary B_0 scan for $f_L = 88$ kHz and $U_{B_{rf}} = 1.55$ V.

Using the distances $L_1 = 522$ mm and $L_2 = 2610$ mm, the two coil sets have been calibrated such that the MIEZE condition (see equation (4.2)) is fulfilled. For the MIEZE setup, as illustrated in figure 3.7, the ratio of the two coil sets is

$$\frac{\omega_B}{\omega_A} = \frac{L_1 + L_2}{L_2} = 1.2. \quad (4.4)$$

In total six echotimes τ_{MIEZE} were configured, which are, using the definition given by equation (4.1): 0.017 ns, 0.0355 ns, 0.0426 ns, 0.0737 ns, 0.106 ns and 0.22 ns with a neutron wavelength $\lambda = 4.33$ Å, $k_i = 1.45$ Å⁻¹ and a neutron velocity $v \approx 913$ m/s, respectively.

4.3 Configuration of the spin-flipper and the adiabatic transition

Since MIEZETOP is based on the longitudinal MIEZE, the polarisation of the neutron beam adiabatically rotates from perpendicular to parallel along the beam in the region between the first polariser and the first $\pi/2$ -flipper. The $\pi/2$ -flipper flips then the polarisation of the neutron back again perpendicular to the beam. The adiabatic transition is illustrated in figure 4.3. The first $\pi/2$ flip defines the starting point of the MIEZE procedure. If the polarisation deviates from perpendicular to the beam after the $\pi/2$ -flipper, this deviation continues throughout the MIEZE process. Therefore, the adiabatic

transition followed by the $\pi/2$ -flip is a critical process, since every imperfection reduces the maximal achievable initial contrast and limits the quality of experiment measurements.

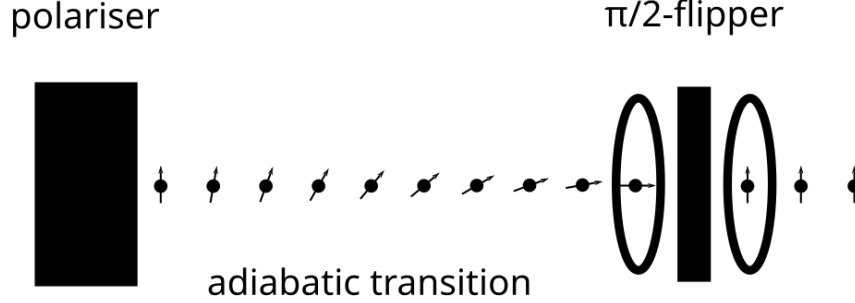


Figure 4.3: Schematic of the adiabatic transition. The polarisation of the neutron beam rotates adiabatically from perpendicular to parallel along the neutron beam. The $\pi/2$ -flipper rotates the polarisation back perpendicular to the beam and defines the starting point of the spin precession and MIEZE procedure, respectively.

Due to the limited space within in the MIEZE setup, there are two sources, that decrease the perfection of the transition:

- The quality of the adiabatic transition depends on the adiabaticity parameter \mathcal{E} , as defined in equation (3.12). The effective field for the adiabatic transition downstream is a linear combination of the decreasing dipole field of the polariser and the increasing field of Helmholtz coils of the $\pi/2$ -flipper, such that the effective field rotates from perpendicular to parallel to the beam. If the $\pi/2$ -flipper is too close to the polariser the effective field rotates too fast and the adiabaticity parameter becomes $\mathcal{E} < 10$. Even though, the simulation yielded an adiabaticity parameter of at least $\mathcal{E} \approx 10.9$, not considered perturbations like external stray fields might disturb adiabatic transition and reduce the adiabaticity parameter to $\mathcal{E} < 10$.
- if the $\pi/2$ -flipper is too close to the B_0 -coil, the spatial extension of the B_0 field is present in the $\pi/2$ -flipper and disturbs the flipping process.

These two negative influences can be compensated to a certain degree by adjusting the horizontal field B_{hsf} and the vertical field B_{sf} of the $\pi/2$ -flipper. Thus, in order to find the optimal initial contrast, for each echo time two maps of the contrast as a function of B_{hsf} and B_{sf} were measured, one for the first $\pi/2$ -flipper and one for the second, the results are shown in figure 4.4. Since the spin-flipping procedure of each flipper is independent of each other, the optimisation can be carried out for each flipper separately. It is sufficient to characterise the first spin flipper in dependence B_{hsf} and B_{sf} while the second spin flipper is set to a calculated maximum. Thereafter the second spin-flipper is characterised

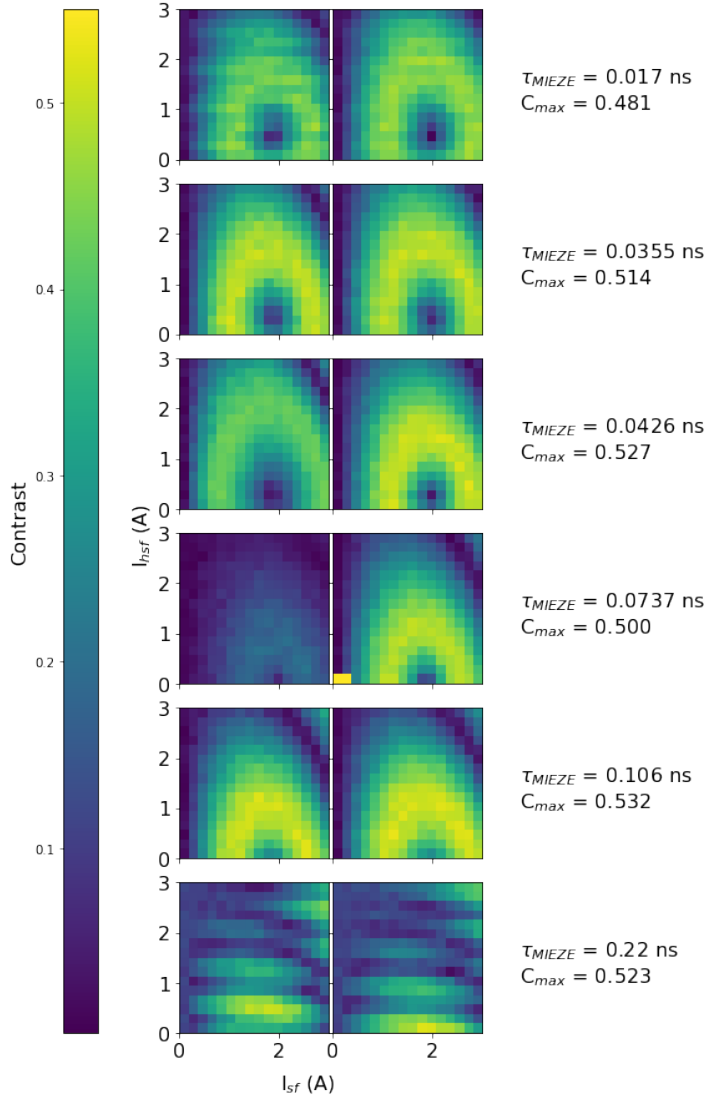


Figure 4.4: The different B_{hsf} - B_{sf} maps and the resulting contrast for the tuned echo times. The left column corresponds to the first $\pi/2$ -flipper and the right column corresponds to the second flipper. Each row refers to a specific echo time with the maximum achieved contrast. The circular structure of high contrast originates from the different spin directions and should be halved at $B_{hsf} = 0$ (see figure 4.5). However, the centre of the ring is shifted to $B_{hsf} > 0$, for lower echo times. With increasing echo time the ring structure shifts to lower B_{hsf} , until the influence of B_0 -field becomes too dominant and the ring structure is no longer visible.

while the previous measured optimum from the first $\pi/2$ -flipper is used. The maximal achieved contrast is listed for each echo time in figure 4.4.

The typical contrast profile in dependency of the two orthogonal fields of the flipper has a ring-like structure, as shown in figure 4.4. Ideally the contrast is maximal, if

4 First measurements of MIEZETOP

the effective field of the $\pi/2$ -flipper has an angle of 45° towards the beam direction, as described in section 3.7.4. However, since the measured contrast directly correlates with the component of the polarisation that is perpendicular to the beam, a magnetic field perpendicular to the beam ($B_{\text{hsf}} = 0$) is also able to rotate the polarisation out of the beam direction and a certain contrast can be measured. In principle, the ring structure shows to which degree the polarisation has been rotated away from the beam direction and, hence, refers to the effective fields, which are able to provide an initial contrast. This is illustrated in figure 4.5.

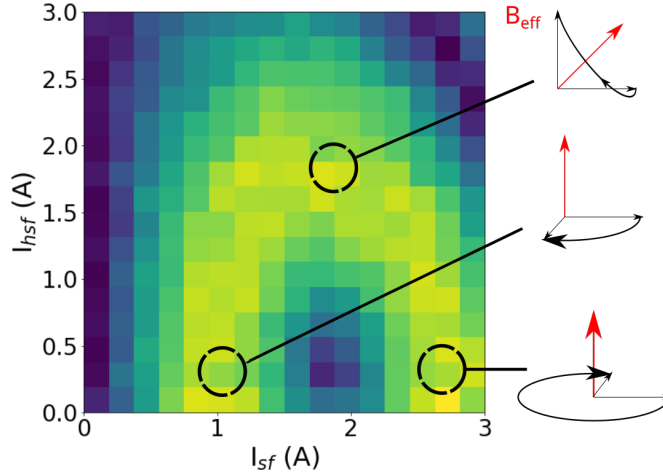


Figure 4.5: Exemplary contrast map. The ring-like structure originates from the influence of the two magnetic fields of the $\pi/2$ flipper, that are perpendicular to each other. For $B_{\text{hsf}} = 0$, i.e. just B_{sf} is scanned, the first maximum is caused by a $\pi/2$ -flip, the minimum by a π -flip and the second maximum by a $3\pi/2$ -flip. By increasing B_{hsf} , the maximum of the contrast shifts towards the $\pi/2$ -flipper condition. The point, where the effective field of B_{hsf} and B_{sf} leads to a π flip (and a effective $\pi/2$ flip), is the point of the highest contrast and the $\pi/2$ -flipper is best configured.

In figure 4.4, two effects of the ring structure are observed, which both are based on the before mentioned spatial challenges: Firstly, the centre of the ring structure does not lie on the x -axis. This indicates that the transition between polariser and $\pi/2$ -flipper is not adiabatic and, thus, the polarisation is not parallel to the neutron beam at the flipper position. For small echotimes, this can to be compensated by the horizontal field B_{hsf} , resulting into a shift of the ring structure to higher fields.

Secondly, the ring-like structure gradually shifts to lower B_{hsf} values as the echotime increases. This behaviour is caused by the by magnetic field of the B_0 coils, which extends to the flipper position and influences the flipping process. For $\tau_{\text{MIEZE}} = 0.22$ ns the circular structure becomes stripe like as the B_0 field becomes too dominant inside the flipper. Due to the proximity of the $\pi/2$ -flipper to the B_0 -coil, $\tau_{\text{MIEZE}} = 0.22$ ns is the highest achievable echotime with a reasonable contrast $C \gtrsim 0.5$, which is possible within the current setup.

The slightly lower contrast of $\tau_{\text{MIEZE}} = 0.017$ ns originates from the Bloch-Siegert

shift, which is prominent for low applied frequencies in the RF-flipper, as mentioned in section 3.7.3.

Beside the aforementioned reduction factors, the polariser in combination with the compact design is possibly another contrast reducing element. Due to the narrow scattering angle of the polariser, a small contribution of neutrons with the unwanted polarisation direction is still contained in the beam, resulting in a decrease of the contrast.

4.4 Reduction Factor in Forward Scattering

The reduction factors of the contrast are especially important for the application of the MIEZE in combination of TAS, as the initial contrast determines the maximal performance of the setup. As described in section 3.6, the angle of the detector influences the contrast of the MIEZE signal, as the path length of the left and the right side of the beam might differ and, thus, a difference in phase $\Delta\phi$ is measured over the cross section of the beam, see equation (3.56). The thickness $\epsilon = 1 \mu\text{m}$ of the foils of the CASCADE detector does not significantly influence the contrast in this setup, see equation (3.61) $R_{\text{detector}} \approx 1$. The influence of detector angle on the contrast is measured with a polycrystalline graphite sample in forward scattering geometry. The geometric shape of the sample was defined by an overlaying cadmium sheet with round cut-out with a diameter of 15 mm, such that the sample can be assumed as a disk. The shape of the neutron beam is $20 \times 20 \text{ mm}^2$ defined by the slit. The six echotimes were measured with three different detector

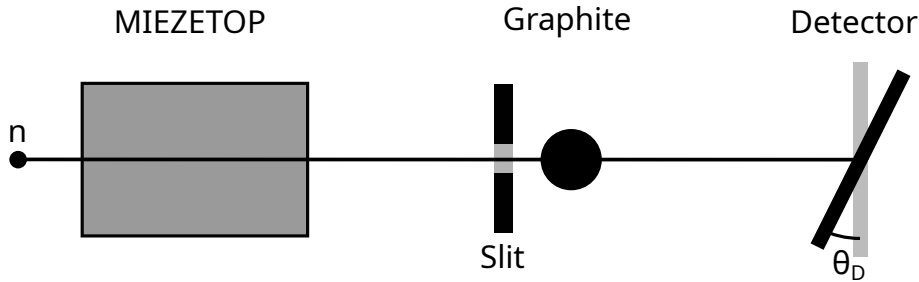


Figure 4.6: Schematic of the setup in forward scattering. A neutron beam passes the MIEZETOP setup, followed by a polycrystalline graphite sample, and impinges on the detector under different angles. The slit defines the beam shape as $20 \times 20 \text{ mm}^2$.

angles ($\theta_D = 0^\circ, 10^\circ, 20^\circ$), where 0° is defined such that the beam is normal to the detector surface. Figure 4.7 a) shows the measured contrast for the different detector angles, whereas Figure 4.7 b) shows the measured contrast normalised with the contrast measured at a detector angle of $\theta_D = 0^\circ$. The solid lines show the reduction in contrast in dependency of the detector angle, following section 3.6. Hereby equation (3.57) was calculated with the Monte-Carlo method as well as numerical quadrature, since in case of a disk the integral has no analytical solution. Both methods yielded the same result.

4 First measurements of MIEZETOP

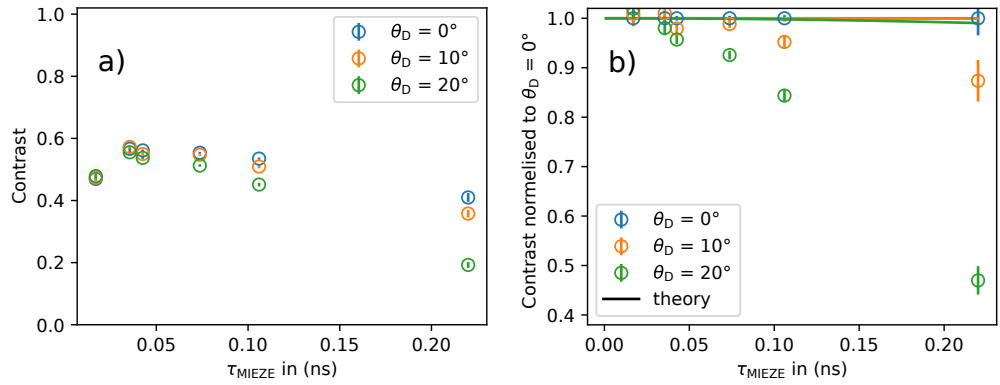


Figure 4.7: MIEZE measurement on graphite powder on forward scattering. a) shows the measured contrast for the different applied angles. b) shows the reduction in contrast of the rotated detector compared to $\theta_D = 0^\circ$. The solid lines show the expected contrast reduction of the detector angles $\theta_D = 10^\circ, 20^\circ$, as described in section 3.6.

There is a drastic deviation of the measured contrast in comparison with the theoretical calculated contrast reduction. In the forward scattering configuration and with a disk of a diameter $d = 15$ mm and a thickness $t = 5$ mm, only marginal changes in contrast with detector angle of maximal $\approx 1\%$ are expected as illustrated by the solid lines in figure 4.7. In this scattering geometry, only the difference of the flight path over the cross section of the neutron beam contributes to the contrast reduction.

The mean spatial width of the MIEZE condition lies in a range of $0.6 < \Delta < 6$ m (see equation (3.53)) for the applied echotimes τ_{MIEZE} and the mean width of the velocity distribution $\delta v/v \approx 0.01$ [32]. The given range of the spatial width of the MIEZE group is of the same order as the distance between sample and detector $L_s = 1.93$ m and, thus, an unfocused MIEZE condition can not explain the strong contrast reduction. The theoretical calculations have already shown to be valid in earlier experiments[51]. A divergent beam, such that the circle on the detector is enlarged does not significantly change the reduction in contrast, as a circle narrows towards the edge and the regions at the edge of no significant statistical influence. Until now, the origin for the drastic contrast reduction has not been resolved.

4.5 Reduction Factor in Diffraction

The influence of the path differences that occur in the diffraction mode on the reduction of contrast was determined by measuring a highly pyrolytic graphite square (HOPG) sample under Bragg condition, illustrated in figure 4.8. HOPG has a high reflectivity 80% for the applied wavelength $\lambda \approx 4.3$ Å [23], which allows fast measurements due to a high intensity. For the chosen wavelength the Bragg peak lies occurs 80.47° , which is expected to have a significant influence on the reduction factor, but still a measurable contrast. Since HOPG is as well the monochromator material, the scattering angles of

the monochromator and the sample stage are the same. Likewise to section 4.4, the shape

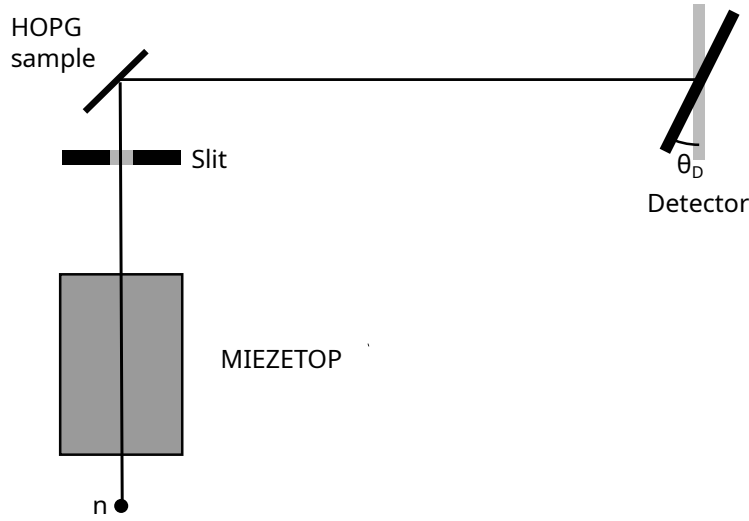


Figure 4.8: Schematics of the diffraction setup. The neutron beam passes the MIEZETOP and gets elastically scattered by a HOPG plate. The analyser crystal lies parallel to the beam such that the beam passes without being scattered. The resulting contrast is measured against the detector angle. The slit defines the beam shape.

of the neutron beam is $20 \times 20 \text{ mm}^2$ defined by the slit.

Under this scattering condition, the contrast was measured in dependence of the detector angle θ_D ranging $-15 < \theta_D < 15$, for each of the six predefined echotimes τ_{MIEZE} . By rotating the detector, the reduction factor, due to the path difference of over the beam profile, can be partly compensated, as described in section 3.6. The measurements are shown in figure 4.9. The measured contrast is given by the circles, where the colours refer to the applied echotimes as labelled on the right. With increasing echotime, the decrease in contrast with respect to the detector angle becomes more significant. Especially for echotimes $\tau_{\text{MIEZE}} < 0.05 \text{ ns}$, the contrast is nearly independent of the detector angle in the observed regime. The angle, where the contrast is maximised, is shifted to $\theta_{D,\text{opt}} \approx 3^\circ$. The solid line is the result of equation (3.58), but normalised to the initial contrast.

The increasing dependence of the contrast to the detector angle with respect to increasing echotime τ_{MIEZE} originates from the decreasing Λ , where $\Lambda = 2\pi v/\Delta\omega$ is the distance a neutron with velocity v travels over one period MIEZE period $2\pi v/\Delta\omega$ as defined in section 3.6. The angular shift in peak position of the measured contrast follows the prediction of equation (3.59) and is at the expected detector angle $\theta_{D,\text{opt}} \approx 3^\circ$.

However, the measured contrast is higher contrast than the theoretical calculations of the reduction factor suggest. This is especially for visible for the higher echotimes $\tau_{\text{MIEZE}} > 0.05 \text{ ns}$. The contrast in dependency of the detector angle decreases faster than the theoretical calculation predicts. The increased sensitivity with respect to the

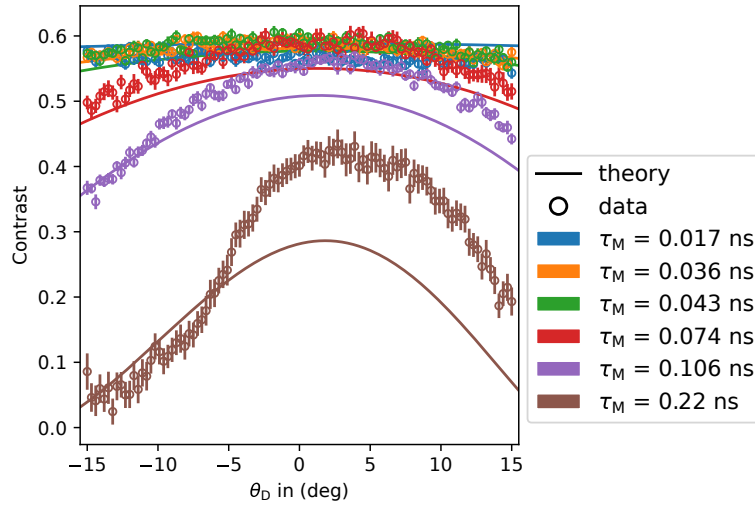


Figure 4.9: The contrast in diffraction mode. The contrast in dependence of the detector angle θ_D is shown. The lines show the expected contrast, following equation (3.58). The circles show the measured data. Each colour correspond to one of the six different echo times τ_{MIEZE} , whose labels are given on the right.

detector angle has been already observed in the forward scattering geometry, section 4.4. Nevertheless, while the contrast can be reduced by several influences like geometry (see section 3.6), misconfiguration of the RF-flipper or misalignment of the components, an increase of the contrast by external influences should not be possible. The contrast which is distinctly higher than predicted in section 3.6, can not be explained, yet.

4.6 Reduction Factor in TAS

For the triple axis mode, the analyser stage was taken into operation and was adjusted to the same wavelength $\lambda \approx 4.33 \text{ \AA}$ or wavevector $k_f = 1.45 \text{ \AA}^{-1}$, respectively. As the analyser crystal is HOPG as well, the same scattering angle $2\Theta = 80.47^\circ$ as in section 4.5 has been used. The same measurements as in diffraction mode (section 4.5) have been carried out, but in the triple axis configuration, as illustrated in figure 4.10. As the reduction factors strongly depend on the width of the sample, a not completely illuminated sample would lead to higher than expected contrast. To ensure the higher contrast does not originate from a under illuminated sample, the measurement was carried out for two different slit sizes. Once, the slit was maximally opened to $120 \times 120 \text{ mm}^2$, while the other time the slit size of previous experiments $20 \times 20 \text{ mm}^2$ was applied.

The measurements are shown in figure 4.11. Similarly as in section 4.5, the measured contrast is given by the circles, where the colours refer to the applied echo times as labelled on the right. The results are in general similar to those without analyser (section 4.5): The angular dependence increases with increasing echo times, the peak of maximum contrast is shifted, following prediction of the calculation of section 3.6, illustrated by the solid

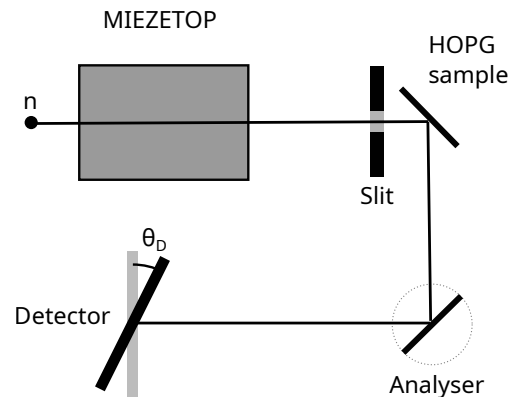


Figure 4.10: Schematics of the triple axis setup. The neutron beam passes the MIEZETOP and gets elastically scattered by a HOPG square-plate. The beam is reflected under the same Bragg condition by the analyser. The resulting contrast is measured against the detector angle. The slit defines the beam shape.

line. Again, especially for longer echotimes τ_{MIEZE} , the measured contrast is higher than the theory suggests. The relative deviation of the calculated contrast and the measured one is of the same order as in the diffraction mode. Similar to the results of section 4.4 and section 4.5, the contrast reduces more drastically with deviation from the optimal detector angle than the theoretically expected. The different slit sizes do not significantly influence the behaviour of the contrast and, thus, the sample is fully illuminated.

Even though, there is no explanation for the increased contrast, the results are promising that the MIEZE technique can be used for inelastic scattering experiments offering high resolution. As the contrast after two elastic scattering processes remains higher than expected, the accessible range in echotime can be extended. Nevertheless, it is inevitable to enlarge distances between components in the MIEZE setup in order to improve the initial contrast. Further a moveable detector or the recently presented subtraction coil [52] can improve the to adjustment of the MIEZE condition and increase the initial contrast.

4.7 Summary

The characterisation of the adiabatic transition between the polariser and the $\pi/2$ -flipper showed that there are two negative influences to the initial contrast (figure 4.3). The field of the B_0 coils is still present in the $\pi/2$ -flipper and, thus, the $\pi/2$ flip is disturbed. Further the adiabatic transition is either incomplete or not slow enough (adiabatic parameter $E < 10$) and, consequently, the polarisation is not fully parallel to the beam. Both influences originate from the spatial restrictions and hamper the polarisation or initial contrast, respectively.

The MIEZE measurement on graphite powder showed that the contrast in dependence of the detector angle decreases more drastically than expected, especially in forward

4 First measurements of MIEZETOP

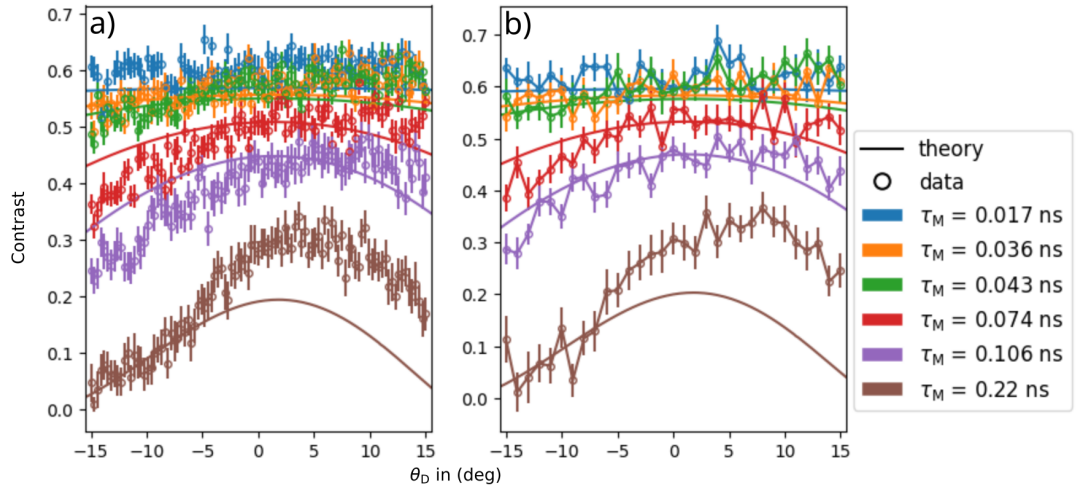


Figure 4.11: The contrast of the TAS mode in dependence of the detector angle θ_D is shown. The lines show the expected contrast, following equation (3.58). The reduction factor of the analyser is treated the same way as the HOPG sample. The circles show the measured data. Each colour corresponds to one of the six different echo times τ_{MIEZE} , whose labels are given on the right. Figure a) shows the data measured with a neutron beam of the shape $120 \times 120 \text{ mm}^2$, figure b) shows the data measured with a neutron beam of the shape $20 \times 20 \text{ mm}^2$.

scattering. The measurements in diffraction and TAS mode showed that contrast does not decrease as much as expected by theoretical calculations. The difference of reduction of the contrast between calculation and measurements can not be explained, yet.

However, the presented results demonstrated the general suitability of the MIEZETOP setup for spectroscopy with neutrons.

5 BaCdVO(PO₄)₂

Presently, there are over hundred different known compositions of vanadates [53]. Vanadium compounds show a variety of physical and chemical properties which are suitable for various applications. Typical applications are the layered lithium vanadates, which are used as electrode material in lithium batteries [54] or bismuth vanadate oxides, which are used as solid electrolytes in fuel cells [55]. Among the magnetic vanadates, especially the low dimensional spin systems have attracted great interest as they reveal extraordinary magnetic ordering such as one-dimensional (1-D) chains, zigzag chains, ladders, and dimers [56]. In this context, the high-temperature superconducting vanadates, which have been found by Anderson [57, 58], increased the interest, due to their square lattice system.

Some of the square lattice vanadates exhibit quasi two dimensional (Q2D) magnetic systems with nearest neighbour (NN) and next nearest neighbour (NNN) interaction of similar magnitude [59]. This is in contradiction to the expected fast decrease of the interaction strength with increasing distance as they couple via super exchange [60].

The exact magnetic order of a 2D square lattice depends on the ratio of the NN interaction and NNN interaction. However, in case of antiferromagnetic interaction between NNN, a 2D square lattice system is frustrated. Depending on type (ferromagnetic or antiferromagnetic) and strength of the NN interaction, the system exhibits different types of order, namely Néel antiferromagnetism (NAF), columnar antiferromagnetism (CAF) and ferromagnetism (FM). This will be explained in more detail in section 5.1. The different types ordering are illustrated in figure 5.1.

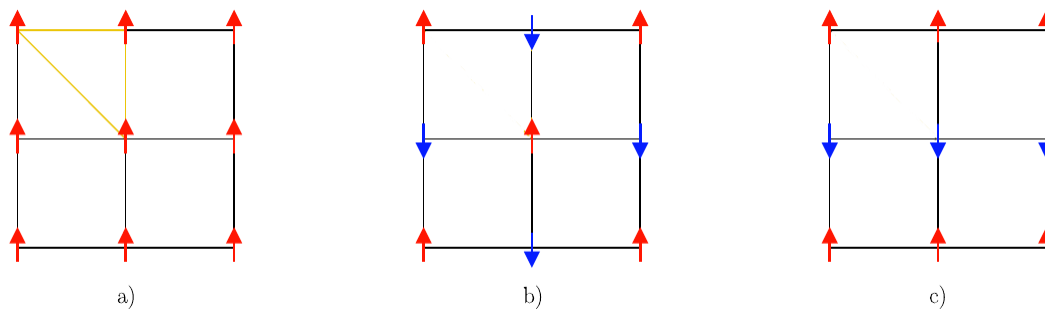


Figure 5.1: Different types of magnetic order. a) FM b) NAF c) CAF

The first two prototypes of a Q2D frustrated square lattice were Li₂VOSiO₄ and Li₂GeSiO₄ [61, 62, 63]. Their square lattice consists of vanadium oxides, where the V⁴⁺

ion with ($S = \frac{1}{2}$) is located in the centre of an O_5 square pyramid. The vanadium oxide pyramids are connected via the SiO_4 or GeO_4 tetrahedra, respectively, and thereby build the square lattice plane. These planes are separated by the Li ions [64]. Both compounds order antiferromagnetically in a columnar fashion [61, 62, 63, 65, 66, 67, 68, 69]. In contrast to them, there are other materials with a square lattice structure that order Néel antiferromagnetic, though, e.g. $VOMoO_4$ and $PbVO_3$ [70, 71, 72].

In this context the family of vanadate phosphates $AA'VO(PO_4)_2$ (with $A, A' = Pb, Zn, Sr, Ba, Cd$) [62, 63, 73, 74, 75, 76] have raised interest. It has been argued that these square lattice systems are frustrated as well, but with the NN interaction being ferromagnetic, while the NNN coupling stays antiferromagnetic. Among the vanadate phosphates, $BaCdVO(PO_4)_2$ is expected to show strong magnetic frustration as the competing NN and NNN interactions are very close to each other. By applying an external field, $BaCdVO(PO_4)_2$ is expected to exhibit a spin nematic phase, where neighbouring spins dimerise into antiferroquadrupolars.

In the following the $J_1 - J_2$ model for two dimensional systems is introduced. Thereafter the physical properties of $BaCdVO(PO_4)_2$, the material of investigation, is described and subsequently the experimental procedure is explained. Finally the obtained results are presented and discussed.

5.1 $J_1 - J_2$ model

The $J_1 - J_2$ model is very common for antiferromagnetic Heisenberg square lattices, where the interaction of nearest neighbours (J_1) and the next nearest neighbours (J_2) are included. J_1 and J_2 are the respective coupling constants, illustrated in figure 5.2. Conventionally,

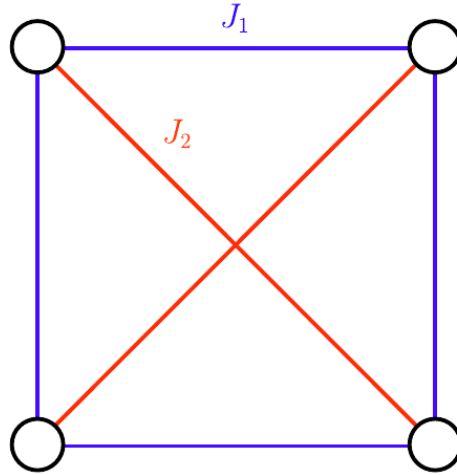


Figure 5.2: $J_1 - J_2$ square lattice. Square lattice of magnetic ions showing NN coupling constant J_1 and NNN coupling constant J_2 . Figure obtained from [77].

negative values refer to ferromagnetic and positive values to antiferromagnetic interaction.

In this specific model the focus lies on just one adjustable parameter, the ratio of $\alpha = \frac{J_2}{J_1}$. This appears rather simple but offers a rich phase diagram including Néel antiferromagnetic phase (NAF) with $\frac{J_2}{J_1} \ll 1$, a columnar antiferromagnetic phase (CAF) phase, with $\frac{J_2}{J_1} \gg 1$ and a spin-gapped phase for intermediate coupling [78]. This model provides many applications, e.g. the simple spin-gapped phase might provide a realisation of Anderson's resonating valence bond (RVB) model.

In the following this model is presented in more detail, starting from the well-known two dimensional Heisenberg antiferromagnet on a square lattice with $J_1 > 0$. Thereafter the frustrating interaction $J_2 > 0$ is included and by that, the change of the magnetic properties is discussed. This model is then generalised by considering ferromagnetic interactions as well and, thus, providing the basis for the complete $J_1 - J_2$ phase diagram, determined by $\alpha = \frac{J_1}{J_2}$.

5.1.1 Two-Dimensional square lattice Heisenberg antiferromagnet

We consider an infinite square lattice with a lattice constant a , where the magnetic moments are located at the corners. In case of pure NN interactions the Hamiltonian is given by

$$\mathcal{H} = J_1 \sum_{i,j}^{\text{NN}} \mathbf{S}_i \mathbf{S}_j, \quad (5.1)$$

where J_1 is the exchange interaction strength and $\sum_{i,j}^{\text{NN}}$ denotes the sum over all nearest neighbours i, j . The ground state for $J_1 > 0$ of this system is a two dimensional NAF, as shown in figure 5.3 and all spins are aligned antiferromagnetically. The ordering vector in this state is $\mathbf{k} = (\frac{1}{2}, \frac{1}{2})$. Due to strong quantum fluctuations, as proven by Mermin and

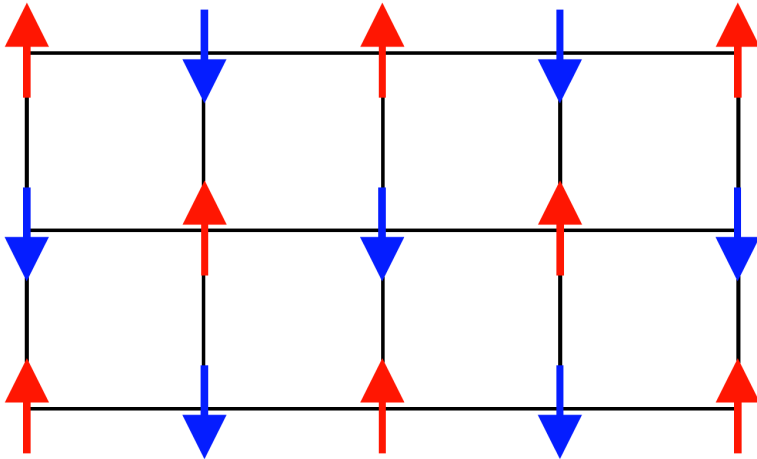


Figure 5.3: Néel antiferromagnetic structure on a square lattice. Figure obtained from [77]

Wagner, Néel ordering is only possible in long range at the temperature $T_N = 0$ K for the isotropic 2D Heisenberg model [79].

Nevertheless, real systems are usually not described by such an ideal model. Pure two dimensional systems are difficult to realise and in reality there is usually a weak interaction J_\perp perpendicular to the planes, which stabilises the antiferromagnetic square lattice. These systems are called Quasi-two-dimensional (Q2D) materials and the Néel temperature is $T_N > 0$. In this Q2D one would expect that the Néel temperature is in the same order as the weakest coupling constant J_\perp , but the observed Néel temperature in Q2D, systems is actually in the order of J_1 , instead of J_\perp . Thus, the phase transition is driven by the intra-layer interactions. Siurakshina et al. [80] presented a theoretical background for the dependence of T_N in a Heisenberg antiferromagnet with a strong spatial anisotropy within the $J_1 - J_2$ model. These results agree well with the experimental observations of Q2D systems.

If one considers an additional antiferromagnetic interaction between NNN, J_2 , the two dimensional system exhibits frustrated interactions, due to the competing couplings of J_1 and J_2 . The two couplings in a square lattice are illustrated in figure 5.2. The Hamiltonian is then supplemented by NNN interactions and becomes

$$\mathcal{H} = J_1 \sum_{i,j}^{\text{NN}} \mathbf{S}_i \mathbf{S}_j + J_2 \sum_{i,k}^{\text{NNN}} \mathbf{S}_i \mathbf{S}_k, \quad (5.2)$$

the second sum $J_2 \sum_{i,k}^{\text{NNN}}$ denotes the sum over all next nearest neighbours. If one now considers that J_1 is strongly dominating ($J_1 \gg J_2$), the NNN interaction is negligible and acts as a small perturbation. Thus the NN interactions lead to an antiferromagnetic ordering as described above, where J_2 was not included (figure 5.3). In this case the frustration introduced by J_2 has no crucial impact on the system.

In the opposite case, when $J_1 = 0$ and $J_2 \neq 0$, the magnetic system splits into two interpenetrating, independent sublattices. These sublattices are rotated by 45° compared to the square lattice and enlarged by a factor of $\sqrt{2}$. The magnetic ordering of this sub-lattice is of the same NAF type, illustrated in figure 5.4 a. Due to the lack of interaction with the NN the magnetic moments of the two sublattices order independently. The two systems can be rotated with respect two each other without any cost in energy, hence, the system in the ground state is degenerated.

Villain's principle of order by disorder stated [81, 82, 83], that by introducing a small perturbation by the NN coupling $J_1 \ll J_2$, the two sublattices are losing their independency and the system gains energy by partially satisfying J_1 . Thus, the spins are aligned antiferromagnetically in one direction and ferromagnetically in the other, as illustrated in figure 5.4 b. The ordering vector is then $\mathbf{k} = (0, \pm\frac{1}{2})$ or $\mathbf{k} = (\pm\frac{1}{2}, 0)$ and the spin rotational symmetry of an antiferromagnet and the 90° rotational symmetry of the square lattice are broken.

Already Shender [84] used this order by disorder theory to explain the experimental data on $Mn_3Cr_2Ge_3O_{12}$. He considered magnetic materials in which it is possible to separate two antiferromagnetic sub-lattices that are placed relative to each other such that the molecular field of the first sub-lattice ions and the one of the second cancel each other. In an analysis beyond the framework of molecular-field theory, where fluctuations were taken into account, a small exchange interaction between the spins of both sub-lattices

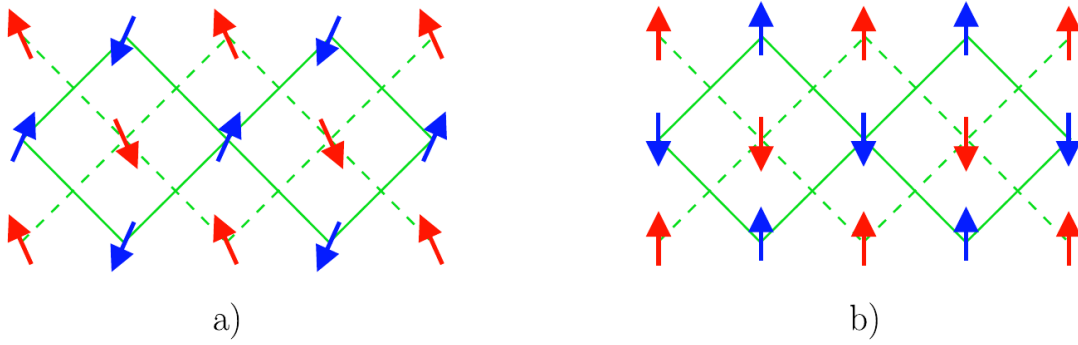


Figure 5.4: Spin structures on a square lattice for the case of $J_1 \ll J_2$ illustrating a) two independent Néel sublattices with an infinite degeneracy $J_1 = 0$, and (b) a columnar antiferromagnetic structure by introducing a small J_1 . Figure obtained from [77].

lead to coupling. The system can gain energy by making these fluctuations coplanar to the neighbouring site. Further Brückel et al. [85, 86, 87] has presented similar behaviour in $(\text{Fe}_x\text{Ga}_{1-x})\text{Ca}_3\text{Ge}_3$, where this behaviour has been observed as a spin wave gap and a splitting of the acoustic magnon branch.

In the intermediate case, where neither J_1 nor J_2 are strongly dominating the ground state properties are determined by the ratio of $\alpha = \frac{J_2}{J_1}$. Classically ($S = \infty$), one would expect a first order phase transition exactly at $\alpha = 0.5$ from NAF ($\alpha < 0.5$) to CAF ($\alpha > 0.5$). At $\alpha = 0.5$ any state with a total spin of zero for an elementary square unit cell would be a ground state of the system, but it does not necessarily include long range spin order.

Quantum mechanically, zero-point fluctuations come into play, which destabilise the ordered state depending on the magnitude of the spin S and the frustration α . If $\alpha \approx 0.5$, the frustration of the system can become so dominant that fluctuations might be able to break down any long range order and the system can exhibit a spin liquid state [88, 89, 90, 91]. The exact ground state of these disordered phases have been studied with many different approaches, e.g. numerical exact diagonalisations [92, 93], field theoretical methods [94, 95, 96] or Dimer-Series Expansions [97, 98, 99], and these approaches predict the disordered regime in the range $0.34 < \alpha < 0.65$. In this ground state, without long range order, the system decreases its energy by dimerisation-like short-range formation of spin singlets between neighbours. These first-neighbour dimers can form various patterns in the lattice, each corresponding to a different valence bond crystal. The simplest scenario is a regular pattern. More specifically, even if there is no long range spin order, there is a long range order in dimers. Green-function Monte Carlo calculations have raised questions about the exact structure of these dimers in the intermediate highly frustrated state. Depending on the reference it yields different results [100, 101]. Finally Sushkov et al [102] claimed that they have solved this problem and presented a phase diagram for frustrated antiferromagnets. This phase diagram was calculated as a function of the frustration parameter α , for a $S = \frac{1}{2}$ system at $T = 0$ with J_1, J_2 antiferromagnetic. They have

found 4 critical points $\alpha = 0.34, 0.38, 0.5, 0.6$. Whereas the phase transition at $\alpha = 0.6$ is of first order, the other three are second order phase transitions. For $0.34 < \alpha < 0.38$ the state is predicted to be a columnar dimerised Néel state, for $0.38 < \alpha < 0.5$ a columnar dimerised spin liquid, and for $0.5 < \alpha < 0.6$ a columnar dimerised spin liquid with plaquette type modulation, visualised in figure 5.5. Even though, there are several theoretical predictions of this ground state, due to the lack of experimental data the intermediate frustrated region remains still an open question.

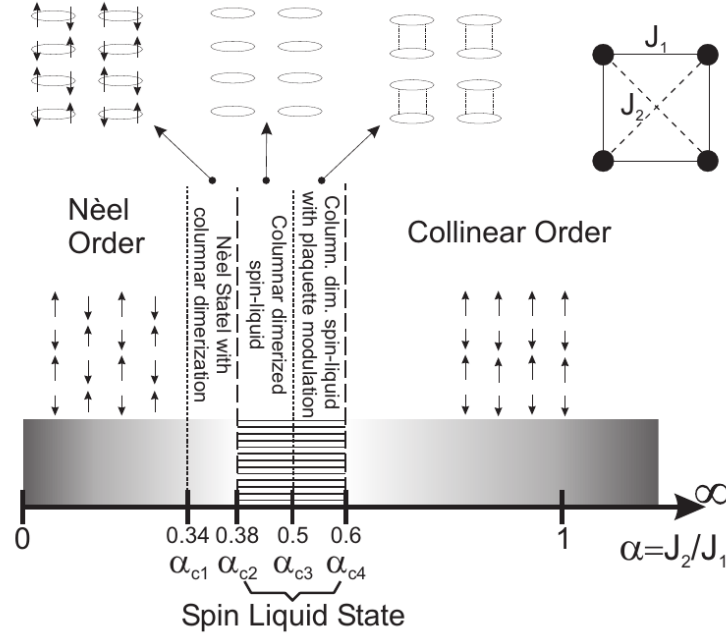


Figure 5.5: Theoretical calculated phase diagram of the $J_1 - J_2$ -model by Sushkov et al. [102]. Figure obtained from [103].

5.1.2 Generalisation of the $J_1 - J_2$ -model

For the generalisation of the phase diagram of the $J_1 - J_2$ -model one has to introduce ferromagnetic interactions. This is a less prominent case than the pure antiferromagnetic $J_1 - J_2$ -model and was first introduced by Shannon et al. [78] and then experimentally observed by Skoulatos et al. [74]. The simplest case is if both J_1 and J_2 are ferromagnetic ($J_1, J_2 < 0$) and the system is a ferromagnet, where J_2 enforces the ferromagnetic structure figure 5.6 a.

Furthermore, if J_1 is antiferromagnetic ($J_1 > 0$) and J_2 ferromagnetic ($J_2 < 0$), J_2 enforces the systems structure as well, resulting in a non-frustrated NAF square lattice, figure 5.6 b. The opposite case, if J_1 is ferromagnetic and J_2 is antiferromagnetic, the system is frustrated, as in $J_1, J_2 > 0$, as either J_1 or J_2 are not fully satisfied figure 5.6 c. One refers to such a system as a *frustrated ferromagnet*.

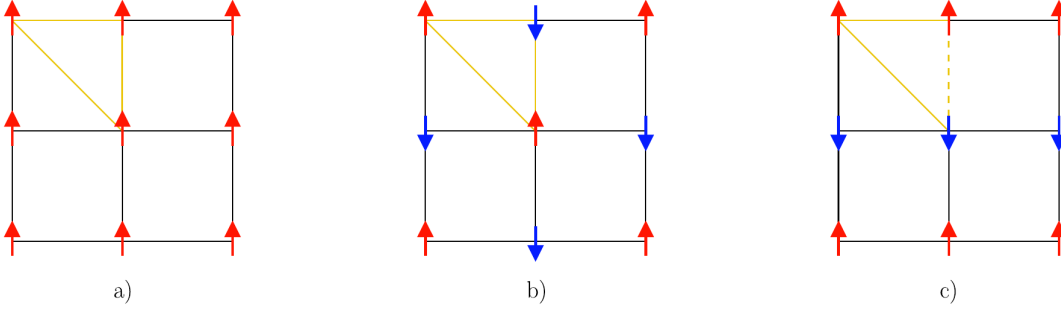


Figure 5.6: Spin frustration and order in a square lattice for a) a uniform ferromagnet ($J_1, J_2 < 0$), (b) NAF with $J_1 > 0$ and $J_2 < 0$ with no frustration and (c) a frustrated FM with $J_1 < 0$ and $J_2 > 0$. Continuous yellow lines are used for ‘satisfied’ spin pairs while the dashed one indicates the frustrated pairs. Figure obtained from ref. [77].

Analogous to the antiferromagnetic case $J_1, J_2 > 0$, the frustrated system $J_1 < 0, J_2 > 0$ has two extreme ground states, where either J_1 or J_2 vanish. On the one hand, if $|J_2| \ll |J_1|$ the system is a ferromagnet, as shown in figure 5.6 a), on the other hand, if J_2 is strongly dominating, the ground state is columnar due to the same reasons as in the antiferromagnetic square lattice case discussed above. In frustrated ferromagnets, one might expect an intermediate regime with strong frustration as well. The difference in the frustrated ferromagnet to the antiferromagnet is the behaviour of the magnetisation. In contrast to the case $J_1, J_2 > 0$, where the total magnetisation is zero independent of α , in the $J_1 < 0, J_2 > 0$ regime the total magnetisation changes from maximum (ferromagnetism) to zero (antiferromagnetism) with respect to α . The regime where J_1 is strongly dominating the magnetisation is the maximised, while the magnetisation of a CAF phase is zero as J_2 dominates. Theoretically, Dmitriev, Krivnov and Ovchinnikov [104, 105] claimed that the transition from a ferromagnet to a columnar antiferromagnet is expected to be quite abrupt at $|\alpha| = 0.5$.

However, in a more recent work of Shannon et al. [106], numerical calculation on an extended Hamiltonian, including cyclic interaction terms, were performed. The calculation predicts a spin liquid phase in a frustrated ferromagnet that exhibits spin nematicity. Since the $J_1 - J_2$ -model only depends on the relative ratio $\frac{J_2}{J_1}$ of the two coupling constants, one can rephrase these parameters, J_1 and J_2 , as

$$J_c = \sqrt{J_1^2 + J_2^2} \text{ and } \Phi = \tan^{-1} \left(\frac{J_2}{J_1} \right), \quad (5.3)$$

where the Φ is the frustration angle and J_c is the overall energy scale. This allows to draw a circular phase diagram including the three phase NAF, CAF and FM, which is shown in figure 5.7. Additionally the known spin liquid phase around $\alpha \approx 0.5$ and further, the new spin nematic phase around $\alpha \approx -0.5$ is illustrated.

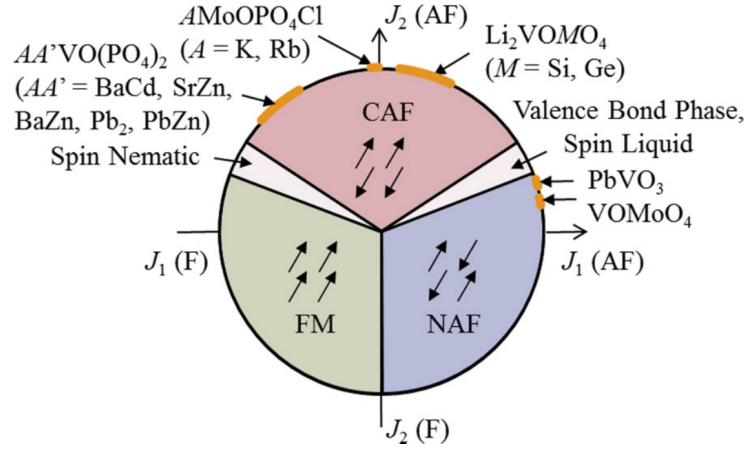


Figure 5.7: Circular phase diagram of the $J_1 - J_2$ -model. The areas show the different types of ordering in dependence of the ratio $\alpha = \frac{J_2}{J_1}$. Conventionally positive J values correspond to antiferromagnetic interaction (AF) and negative to ferromagnetic (FM). Further the spin nematic and spin liquid phase are labelled which lie in the corresponding transition region. Known compounds, where the $J_1 - J_2$ model is applicable, are noted on the circular phase diagram. Figure obtained from ref. [107].

5.1.3 Spin nematic

Nematicity is a term that is usually connected to liquid crystals, like they are used in liquid crystal display (LCD) TVs. In the nematic phase a system orders only in one dimension and is random in the other two. The most common example for the nematic phase are a liquid of rods, where all rods are parallel.

A similar effect can be considered for spin systems. The simplest spin nematic phase is the $S = 1$ state. The $S = 1$ state has 3 projection on the z -axis $m = 1, 0, -1$, where $m = \pm 1$ is considered as spin up $|1, 1\rangle$ or spin down $|1, -1\rangle$.

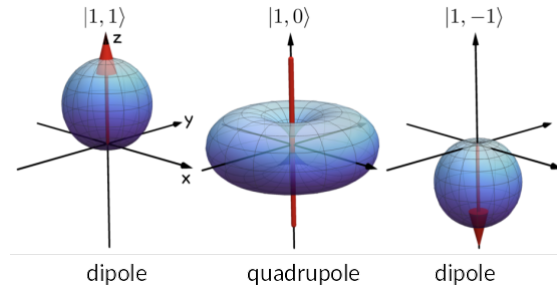


Figure 5.8: The 3 different projections of the $S = 1$ state. Left and right correspond to spin up and spin down state, respectively. The center one is the quadrupole state. The blue surface is the probability distribution. Figure is taken from ref. [108]

Figure 5.8 shows the three projections. The blue volume is the probability distribution

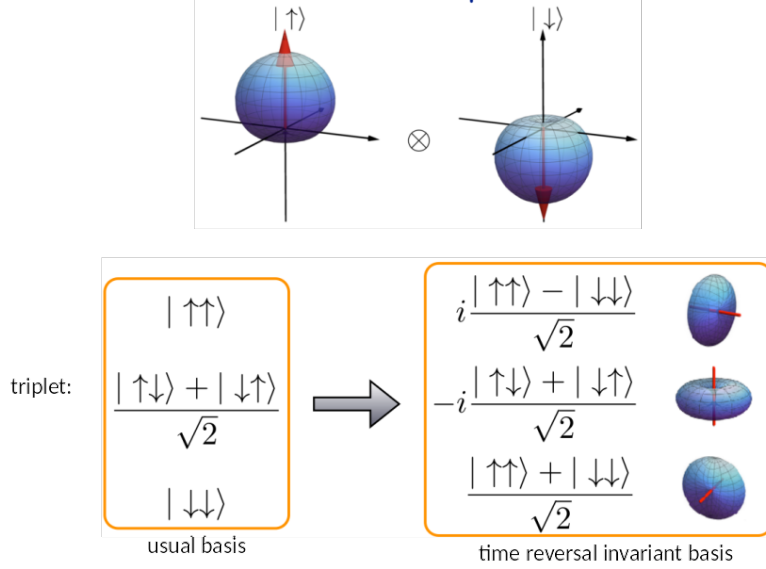


Figure 5.9: Two $S = 1/2$ spin states can build a triplet state. A system with two bonding $S = 1/2$ spins has three basis states with a total spin angular momentum of $s = 1$. A basis transformation results into three orthogonal quadrupole states. Figure is taken from ref. [108].

for the spin direction. For $m = \pm 1$ the probability distribution is above or below the $x - y$ plane. The average spin direction is indicated by the red arrow. In contrast to the dipole, the spin state $m = 0$, namely the quadrupole state, lies in average in the $x - y$ plane, but never along the z -axis. The axis with no possible spin state, which has no specific direction is called a director, as opposed to a vector, which has a pointing direction. A system consisting of these quadrupoles can exhibit long range order, where the time reversal and translational symmetry is preserved but the spin rotational symmetry is broken with anisotropic spin fluctuations. This is the spin analogy of a liquid crystal [109].

Figure 5.9 shows a different possible realisation of spin quadrupoles, compared to the previous $S = 1$ case. In case of a frustrated magnet with $S = \frac{1}{2}$, a spin nematic phase can still occur. This can be realised by two neighbouring spins bound together and build triplet state, leading to the term bond-spin nematic. [106, 110, 111, 112]. In a $S = \frac{1}{2}$ system, which consists of a spin up and a spin down state, the triplet state obtained by the bonding of the two spin states is usually given by the basis

$$|\uparrow\uparrow\rangle, \frac{|\downarrow\uparrow\rangle + |\uparrow\downarrow\rangle}{\sqrt{2}}, |\downarrow\downarrow\rangle. \quad (5.4)$$

By the transformation of this basis into a time reversal invariant basis one obtains [109]

$$i\frac{|\uparrow\uparrow\rangle - |\downarrow\downarrow\rangle}{\sqrt{2}}, -i\frac{|\downarrow\uparrow\rangle + |\uparrow\downarrow\rangle}{\sqrt{2}}, \frac{|\uparrow\uparrow\rangle + |\downarrow\downarrow\rangle}{\sqrt{2}}, \quad (5.5)$$

resulting into three orthogonal quadrupole states. These quadrupole states can exhibit long range order. The simplest order of such a spin nematic phase is the onsite quadrupolar spin order, where spin fluctuations show an anisotropy regarding their different axes. This type of spin nematic is called ferroquadrupolar, since the fluctuations form a quadrupole moment of \mathbf{S} with a common axis on all sites [113]. More generally, quadrupole moments prefer to select orthogonal axes, resulting in a antiferroquadrupolar. Antiferroquadrupolar ordering is illustrated in figure 5.10.

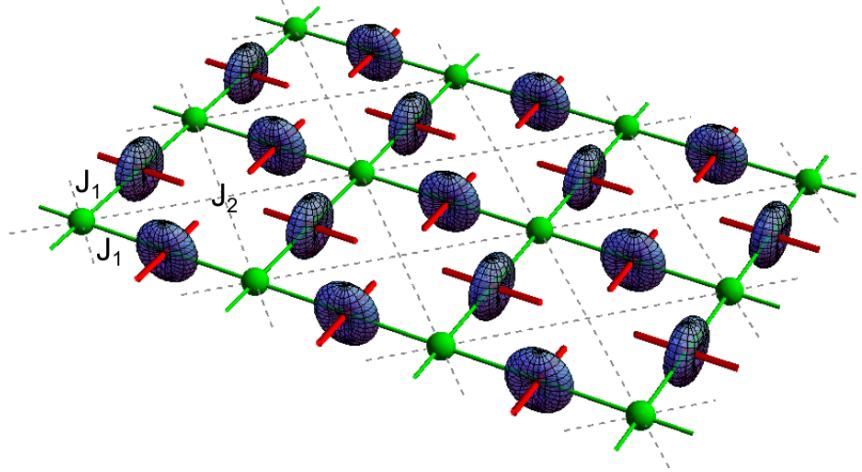


Figure 5.10: Two-sublattice, bond-centered spin nematic state. The ordering of this type can be found in spin-1/2 frustrated ferromagnets in applied magnetic field. The green spheres represent a magnetic ion that bonds with the neighbouring spin into quadrupoles. The resulting quadrupolar spin fluctuations are visible in the probability distribution for spin fluctuations on the bonds of the lattice, here represented by a blue surface. The red rods represents the corresponding director. Figure obtained by ref. [109]

However, the time reversal invariance makes the spin nematic states “invisible” for the most common probes of magnetism, as they do not exhibit magnetic Bragg peaks or a static splitting of lines in NMR spectra [17]. In thermodynamic measurements, e.g. heat transport, the phase transition behaves like a AFM transitions. Since spin nematics are expected to exhibit a linearly dispersing goldstone mode [109], the spin nematic state might be detected by inelastic neutron scattering.

Spin-nematic order is known to occur close to saturation in the spin- $\frac{1}{2}$ $J_1 - J_2$ model on a square lattice for ferromagnetic J_1 and antiferromagnetic J_2 [106, 110, 114]. This model is believed to describe a number of quasi-two-dimensional magnets, including $\text{BaCdVO}(\text{PO}_4)_2$. Among the vanadate phosphates $\text{BaCdVO}(\text{PO}_4)_2$ is a possible candidate to exhibit such a spin nematic phase [115]. The H-phase diagram of $\text{BaCdVO}(\text{PO}_4)_2$ is illustrated in figure 5.11. By applying an external magnetic field one can change the favorable phase of $\text{BaCdVO}(\text{PO}_4)_2$ from antiferromagnetism to ferromagnetism passing the spin nematic phase.

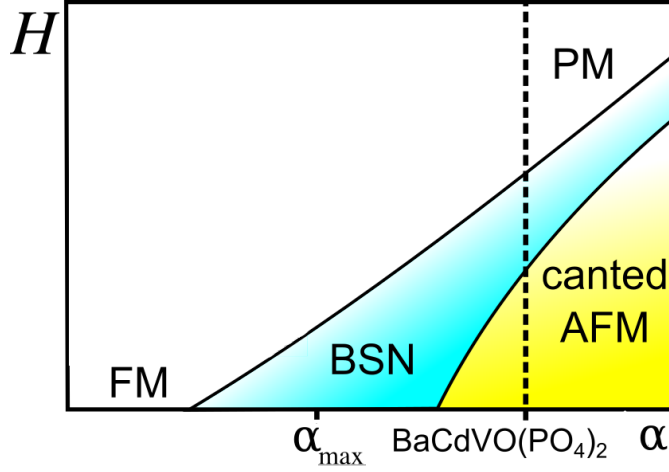


Figure 5.11: H-Phase diagram of J_1 - J_2 model systems. The external magnetic field in dependency of r . The parameter r denotes the ratio of $\frac{J_1}{J_2}$. The dashed line shows the expected location of BaCdVO(PO₄)₂. Figure is adapted from ref. [59]

5.2 BaCdVO(PO₄)₂

BaCdVO(PO₄)₂ belongs to the group of vanadium phosphates AA'VO(PO₄)₂, which present a realisation of frustrated ferromagnets [62, 63, 73, 75, 76]. These compounds crystallise in layered structures, where the V⁴⁺ ($S = \frac{1}{2}$) ions arrange in a square lattice. This square lattice layer consists of VO₅ square pyramids, which are linked via PO₄ tetrahedra [76]. These tetrahedra take the transmitting role for superexchange interactions for both NN and NNN. Metal cations and additional PO₄ tetrahedra are separating these square lattice layers. The structure of BaCdVO(PO₄)₂ is illustrated in figure 5.12. Among the vanadate phosphates, frustrated square lattices were found for AA' = Pb₂, SrZn and BaZn. All of them order magnetically as CAF. First Nath et al. [76] identified via heat capacity measurements a phase transition in BaCdVO(PO₄)₂ at around $T_N \approx 1$ K for magnetic fields $H < 3.5$ T. Further Ref. [76] reported that the system saturates at fields $H \gtrsim 4$ T. These results were interpreted as a model with NN exchange $J_1 \approx -3.6$ K and NNN exchange $J_2 \approx 3.2$ K. Hereby the low-field ordered state is assumed to be a canted AFM with propagation vector $q_{sq} = (1/2, 0)$ [78, 116]. Povarov et al. [117] have extended the magnetic phase diagram of BaCdVO(PO₄)₂ by thermodynamic measurements and thereby, filled the gaps at fields close to saturation and low temperatures $T_N < 1$ K, where the spin liquid phase is expected. They found a high spin fluctuating regime around $H = 4$ T, but the exact nature of the low-temperature phase stays elusive.

By using a combination of neutron-scattering and AC susceptibility measurements performed in the range of $0 < H < 4.5$ T, Skoulatos et al. [59] recently identified the ground state as an unusual “up-up-down-down” antiferromagnet. This is an evidence of strong frustration, but also that the $J_1 - J_2$ -model is not sufficient to describe this system properly. Further they showed that this order breaks down at $B = 3.8$ T and saturation

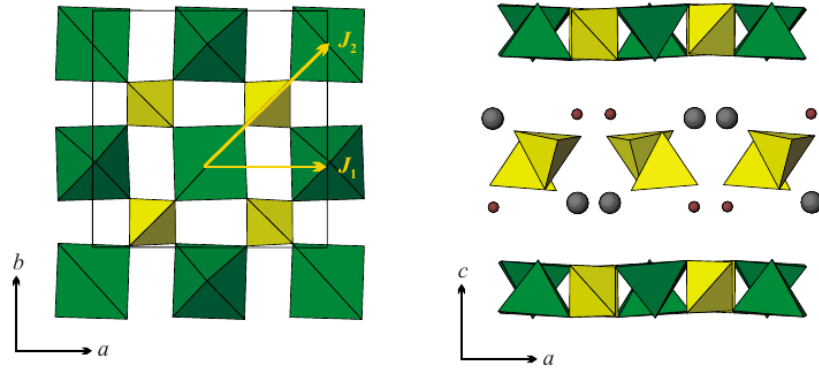


Figure 5.12: Crystal structure of $\text{BaCdVO}(\text{PO}_4)_2$: single $\text{VO}(\text{PO}_4)$ layer are shown in the left figure while the stacking of the layers are shown in the right figure. The superexchange interactions J_1 and J_2 are given by the arrows. Larger and smaller spheres denote Ba and Cd cations, respectively. Obtained from ref. [76].

is reached at $B \gg 4.5 \text{ T}$.

More recent results by Bhartiya et al. [118] revealed that the crystal structure is not the expected usual square lattice, but instead showed that the crystal structure is of lower dimensionality than expected. The magnetic ordering is a 2D collinear ferromagnet, which orders up-up-down-down. This leads to alternating interactions along one direction and the previous defined $J_1 - J_2$ -model has to be extended. Hereby each J_1 and J_2 have to be distinguished by symmetry and direction. Hence, J_1 and J_2 splits into $J_1^a, J_1^b, J_1^a, J_1^b$ and $J_2^+, J_2^-, J_2^+, J_2^-$, respectively, as illustrated in figure 5.13. Based on that Bhartiya et al. [119] have presented full-scale neutron measurements in the saturation regime of $\text{BaCdVO}(\text{PO}_4)_2$. With the collected data and by the use of a global model developed by Smerald [120] they were able to fit the spin wave dispersion and by that, obtained values for the eight coupling constants at high magnetic fields in the saturated phase. The most general Hamiltonian of such a system, that includes small spatial deviations of the V^{4+} within the square lattice, is given by

$$\mathcal{H} = \sum_{i,j} J_{i,j} \mathbf{S}_i \mathbf{S}_j - h \sum_i S_i^z \quad (5.6)$$

where i, j runs over all NN and NNN bonds and \mathbf{S} is the spin-1/2 operator. The $J_{i,j}$ are the corresponding eight coupling parameters. The resulting spin wave dispersion of this system consists of two branches corresponding to two crystallographic in-equivalent V^{4+} sites [119]

$$\hbar\omega_q = \frac{A_q + A'_q}{2} \pm \sqrt{\frac{A_q - A'_q}{2} + |B_q|^2}, \quad (5.7)$$

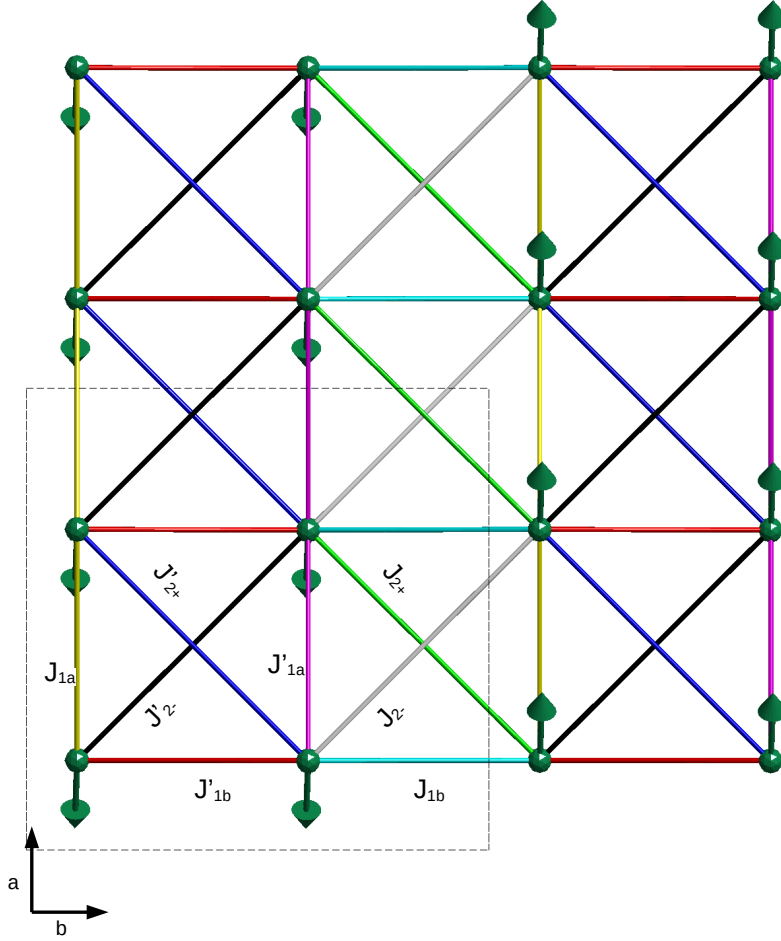


Figure 5.13: The magnetic unit cell in the a, b plane of $\text{BaCdVO}(\text{PO}_4)_2$. $\text{BaCdVO}(\text{PO}_4)_2$ orders as a collinear antiferromagnet with an up-up-down-down magnetic structure where pairs of rows are parallel ordered but the paired rows are ordered antiparallel with respect to each other. This leads to in total 8 different coupling constants including nearest and next nearest neighbours. Nearest neighbours are indexed by '1' while next nearest neighbours are indexed by '2'. The coupling constants along the ferromagnetic ordering are labelled by 'a' and the one along the antiparallel ordering by 'b'. The coupling constants within a paired row are primed. The \pm are introduced to distinguish between the two next nearest neighbours within one square.

where

$$\begin{aligned}
A_q &= \tilde{h} - J_{1a}(1 - \cos(\mathbf{q}\mathbf{a})) \\
A'_q &= \tilde{h} - J'_{1a}(1 - \cos(\mathbf{q}\mathbf{a})) \\
2B_q &= (J_{1b}e^{iqb} + J'_{1b}e^{-iqb}) \\
&\quad + (J_{2+}e^{-i(qa-qb)} + J'_{2+}e^{i(qa-qb)}) \\
&\quad + (J_{2-}e^{i(qa+qb)} + J'_{2-}e^{-i(qa+qb)}) \\
\tilde{h} &= g\mu_B\mu_0 H - \frac{1}{2}(J_{1b} + J'_{1b} + J_{2+} + J_{2-} + J'_{2+} + J'_{2-}).
\end{aligned}$$

The labelling of the coupling constants J is the same as given in figure 5.13, a and b are the different crystal directions in the square lattice plane. H is the applied magnetic field. This model was used to fit our powder spectra data as well to fit the high saturated field data by Bhartiya et al. [119]. If this model can be applied to a extended data set and verified for different magnetic fields, one could get a deeper insight into the system. Further, this might open the possibility of studying the spin liquid phase in more detail.

5.3 Experimental procedure

The production of the powder sample is described in [76]. They were prepared by the solid-state reaction technique using BaCO₃, CdO, V₂O₃, V₂O₅, and (NH₄)₂HPO₄. First, the intermediate compound BaCdP₂O₇ was prepared by firing the stoichiometric mixture of BaCO₃ and (NH₄)₂HPO₄ at 950 °C in air for 48 h. Thereafter, stoichiometric amounts of BaCdP₂O₇, V₂O₃, and V₂O₅ were grinded, pelletised, and annealed in dynamic vacuum (10⁻⁵ mbar) or evacuated in a sealed quartz tube (10⁻² mbar) at 800 °C for 30 h.

The neutron scattering experiments were performed on the time-of-flight (TOF) instruments LET and IN5 at ISIS, Oxfordshire, United Kingdom and ILL, Grenoble, France, respectively, with applied field. The polycrystalline specimen was placed in a cylindrical hollow wall aluminium container, to reduce the absorption but still maintaining the cylindrical geometry. The cylinder had a diameter of 25 mm with a hollow space in the wall of 2 mm. Cadmium coverage at the top and bottom of the cylinder reduced the Al scattering. All measurements were performed at 40 mK. Varying fields up to 8 T were applied and various wavelengths have been selected, between 5.5 Å and 10 Å. Thereby one obtains powder spectra which were used to fit the a model.

5.4 Results and Discussion

The powder spectra of the TOF measurements are shown in the first column of figure 5.14. Measurements were performed at various magnetic fields between 0 T and 8 T, but only the measurements at $B = 0$ T and $B = 8$ T had a signal to noise ratio where a further analysis was possible. Further the measurements were performed for various incident wavelengths ranging from $\lambda = 3.5$ Å to $\lambda = 10$ Å. For $B = 0$ T, a wavelength of $\lambda = 6.5$

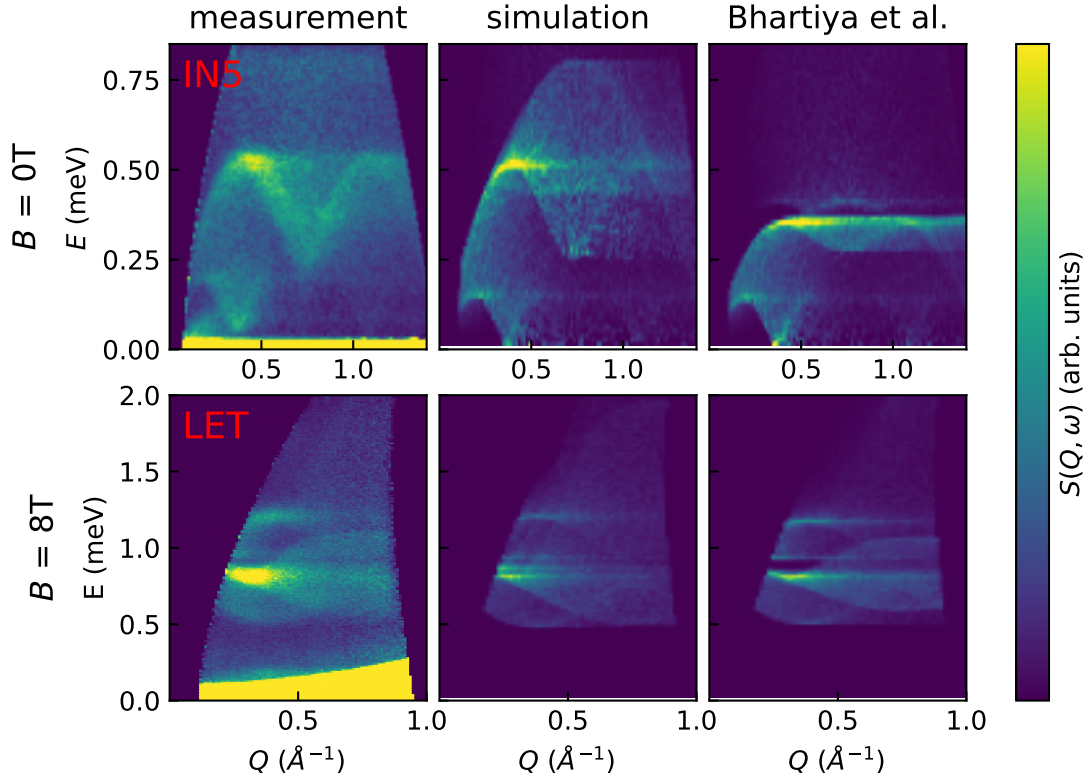


Figure 5.14: Measured data obtained at IN5 or LET (first column), simulated powder spectrum (second column) and the simulation with the parameter from Bhartiya et al. (third column). First row corresponds to the 0T and the second row to 8T

\AA yielded the best match to the system's energy scale and signal to noise ratio, whereas for $B = 8\text{ T}$, a wavelength of $\lambda = 5.5\text{ \AA}$ was found as an optimum.

The dispersion relation equation (5.7), described in section 5.2 was used as the model to fit the powder data obtained from the TOF measurements at $B = 0\text{ T}$ and $B = 8\text{ T}$ at LET and IN5, respectively. The fitting procedure of the powder spectra was done using the SpinW library in MATLAB [121]. Since the calculation was very performance consuming, the fit was performed on the supercomputer "deep-thought" with help from Georg Brandl. The coupling terms that were obtained by the fitting procedure are shown in table 5.1. With these parameters and the SpinW library in MATLAB, the powder spectra of $\text{BaCdVO}(\text{PO}_4)_2$ were simulated for 0 T and 8 T, which is shown in the second column of figure 5.14.

Concurrently to the powder measurements performed by us, Bhartiya et al. performed triple axis spectroscopy at IN12, ILL, Grenoble, France and Multi-Axis Crystal Spectrometry (MACS) at National Institute of Standards and Technology, Gaithersburg, Maryland, USA on a single crystal of $\text{BaCdVO}(\text{PO}_4)_2$ in the fully saturated phase $B = 9\text{ T}$ [118, 119]. By using the same dispersion relation (equation (5.7)) as model, they fitted the data of

coupling constant	powder (meV)	Bhartiya et al. [119] (meV)
J_{1a}	-0.75 ± 0.08	-0.135
J'_{1a}	-0.82 ± 0.09	-0.614
J_{1b}	-0.94 ± 0.10	-0.314
J'_{1b}	-0.87 ± 0.09	-0.464
J_{2+}	0.75 ± 0.08	0.384
J'_{2+}	0.41 ± 0.05	0.039
J_{2-}	0.64 ± 0.07	0.361
J'_{2-}	0.18 ± 0.02	0.181

Table 5.1: Coupling constants of obtained by the fitting procedure on the powder spectra of $B = 0$ T and $B = 8$ T and coupling constants of obtained by single crystal measurements at $B = 9$ T by Bhartiya et al. (uncertainties have not been provided).

the single crystal measurement. The obtained parameters by Bhartiya et al. show a large discrepancy to the parameters obtained by our fitting procedure (see table 5.1). Using SpinW and the parameters reported by Bhartiya et al., powder spectra for $B = 0$ T and $B = 8$ T were simulated, which is shown in the third column of figure 5.14.

The powder spectra in figure 5.14 of $\text{BaCdVO}(\text{PO}_4)_2$ could be nearly perfectly reproduced by the simulated spectra using the parameter set as obtained by our fitting procedure. If one considers the background that is present in real experiments, the measurement and simulation match very well for both fields, $B = 0$ T and $B = 8$ T. The strong signal close to $E = 0$ in the measurements originates from elastic scattering and is not included in the simulation.

By comparing the powder spectra obtained by parameter set of Bhartiya et al. with the powder spectra of our parameter set (listed in table 5.1), one sees that both yield nearly identical spectra in the saturated field region at $B = 8$ T. However the simulation of our parameter set shows a small splitting around $E \approx 0.9$ meV, which is not present in the spectrum of Bhartiya et al., but such details are not distinguishable with the given resolution of the TOF spectrometer used by us and the present background. In contrast, the simulated spectra at $B = 0$ T do not agree in the regime of $E > 0.2$ meV. The disadvantage in TOF measurements on powder samples is that one measures $|Q|$ and thus, the dispersion relations of all directions that fulfil $|Q|$ at once. The fact that several dispersions are seen in one measurement make the analysis more difficult and further, there might not only exist one parameter set that can reproduce the observed spectra, especially if one considers the background and a limited resolution. Hence, although the parameter set obtained by us and the parameter set by Bhartiya et al. differ, both parameter sets can generate a nearly identical powder spectrum. Generally a single crystal measurement as done by Bhartiya et al. is more reliable for the analysis of the spin wave dispersion. However, the parameter set by Bhartiya et al. is not able to describe the powder spectrum at $B = 0$ T. Since the single crystal measurement was only done in the saturated field phase and only covers a limited regime in the reciprocal space, it might not

be sufficient to identify the correct parameter set for the dispersion relation equation (5.7) of $\text{BaCdVO}(\text{PO}_4)_2$.

In contrast, the dispersion relations of the single crystal data were simulated as measured by Bhartiya et al., using the parameter set that was obtained by the analysis of the TOF powder data. The simulations of the dispersion relations are shown in the first two rows of figure 5.15 and are compared to the model with parameters as given by Bhartiya et al. in the latter two rows of figure 5.15. Some of the dispersions show a similar trend (figure 5.15 $c \leftrightarrow m$, $d \leftrightarrow n$, $g \leftrightarrow q$), but most of them are very different. Although our parameter set was obtained at different fields, it also does not describe the dispersion properly, since our parameter set cannot reproduce the dispersion relation of the single crystal measurements.

In order to obtain a better insight into the magnetic system of $\text{BaCdVO}(\text{PO}_4)_2$, it is inevitable to use a more extensive data set to determine the correct coupling constants. The super computer Deep Thought is right now out of operation, but as soon as it is available again, a new fitting procedure is prepared including the measurements on the single crystal obtained by Bhartiya et al. as well as the powder spectra obtained by our TOF measurements. Nevertheless, extensive measurements on the single crystal at different fields, especially $B = 0 \text{ T}$, would provide a more reliable basis for a spin wave analysis.

5.5 Summary

Measurements of a $\text{BaCdVO}(\text{PO}_4)_2$ powder sample were presented and compared to the single crystal data obtained by Bhartiya et al. [119]. By fitting of the dispersion relation (equation (5.7)) to the powder spectra, coupling constants were obtained which were able to reproduce the $B = 0 \text{ T}$ and the $B = 8 \text{ T}$ powder spectra in a simulation. However, the parameter set that is obtained by fitting a powder spectrum is not necessarily unique. A concurrently published analysis of the spin wave dispersion of a $\text{BaCdVO}(\text{PO}_4)_2$ single crystal in the saturated phase yielded a set of coupling constants which differs from the set obtained by us. The simulation of the powder spectra using the coupling constants of Bhartiya et al. showed that the parameter set is able to reproduce the measured spectra at $B = 8 \text{ T}$, but not the $B = 0 \text{ T}$ powder spectra. In contrast, our parameter set was used to simulate the dispersion of the single crystal data of Bhartiya et al. which was not successful either. Both parameter sets only agree with a limited data set, but do not successfully describe all available data.

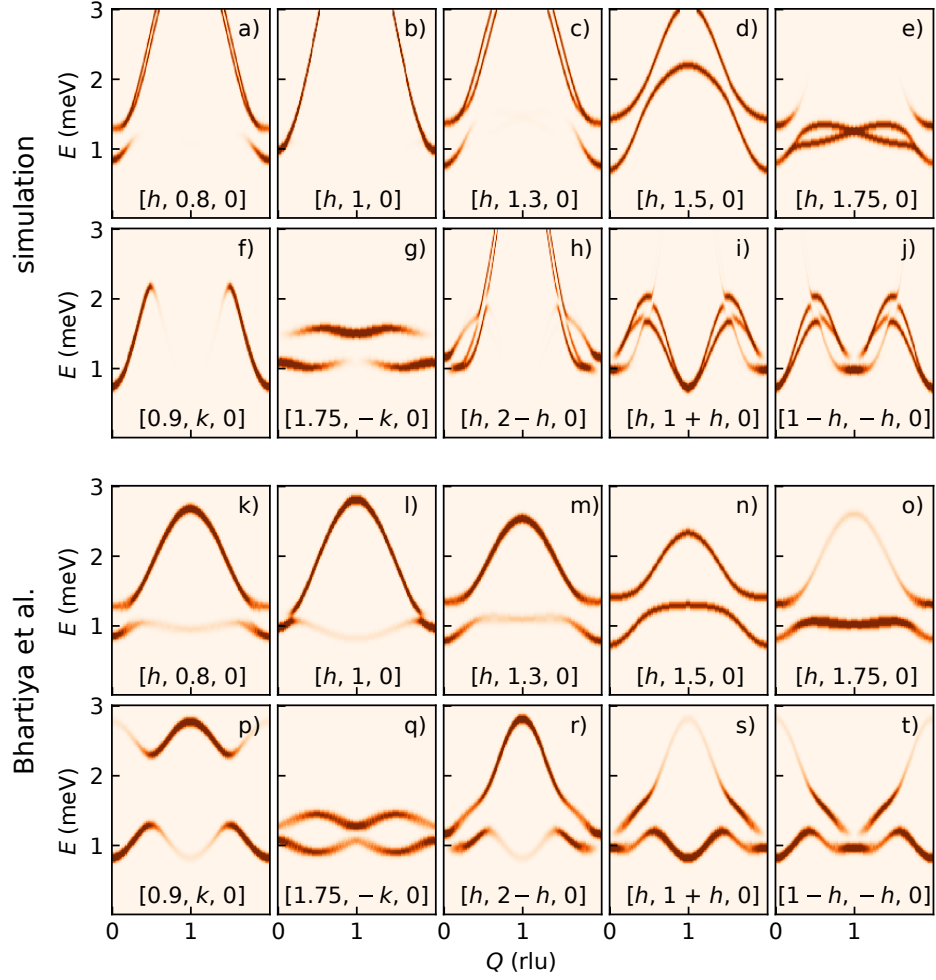


Figure 5.15: Dispersion of the spin wave of $\text{BaCdVO}(\text{PO}_4)_2$ as measured by ref. [119]. The figures (a-j) are the simulated spin wave dispersions of a $\text{BaCdVO}(\text{PO}_4)_2$ single crystal using the exchange couplings obtained by our powder measurements, which are listed in table 5.1. The spin wave dispersions were simulated according phase space (E, \mathbf{Q}) , which was measured by ref. [119]. The figures (j-t) are the spin wave dispersions simulated in the same phase space using the exchange couplings of ref. [119], which is listed in table 5.1.

6 CuMnSb

CuMnSb is a so-called "half-Heusler" compound. Fritz Heusler discovered in 1903 the first compound Cu_2MnAl , which exhibited - at that time - surprisingly ferromagnetism, although none of the constituents is magnetic. Nowadays, more than 1000 different Heusler compounds are known, exhibiting a variety of magnetic and electronic properties, which can be often predicted by counting the valence electrons [122, 123]. Over 250 of the "Heuslers" are semiconductors with a band gap varying from 0 to ≈ 4 eV [124]. Some "Heuslers" express several kinds of magnetic behaviour, like magneto-optical, magneto-caloric, magneto-electrical and magneto-structural characteristics. Especially the half-metallic ferromagnets are a crucial element of interest in the field of spintronics [125, 126, 127, 128].

The half-Heusler and full-Heusler compounds differ by composition with the nomenclature of XYZ for half-Heusler and X_2YZ for full-Heusler materials. The X and Y atoms, usually transition metals, possess cationic character, whereas Z is often an element from the main group of the periodic table and is seen as the anionic counterpart.

Full-Heuslers crystallise in the $L2_1$ cubic structure with space group $\text{Fm}\bar{3}m$, with all four atoms ordered in a face-centered cubic (fcc) lattice, but each is shifted by a quarter of the cube's diagonal with respect to each other resulting in four fcc sub-lattices at $(0, 0, 0)$, $(1/4, 1/4, 1/4)$, $(1/2, 1/2, 1/2)$ and $(3/4, 3/4, 3/4)$. In contrast to the full-Heuslers, a half-Heusler compound crystallises in the $C1_b$ structure with space group $\text{F}\bar{4}3m$, which is equal to a full-Heusler, except one of the four fcc sub-lattices not being occupied. Consequently half-Heuslers lack a centre of inversion [122].

The half-Heusler CuMnSb is one of few in the group of magnetic Heuslers that orders type-II antiferromagnetic, making it unique among Heuslers based on 3d-transition metal as of the time of writing [19]. CuMnSb has raised interest as a possible candidate of a half-metallic ferromagnet [129], but was identified as a compensated semimetal via electronic structure calculations by Jeong et al. [130]. Furthermore, Jeong et al. argued that there are possibly two competing interactions mechanisms, namely local-moment and itinerant magnetism that is realised by the heavy conduction electrons and the light valence band holes. In combination with the low Néel temperature of $T_N \approx 55$ K, this intimates that there is magnetic frustration within this compound. Additionally, theoretical calculations of Maca et al [18] indicated that the magnetic ground state of CuMnSb is more complex than initially assumed and it is assumed that the type-II antiferromagnetism is stabilised by defects in the crystal, namely, Mn antisites on Cu lattice, and Mn interstitials. Regnat et al [22] observed in a high quality single crystal a canting of the spins away from the antiferromagnetic ordering direction at temperatures below $T^* = 34$ K, indicating also a more complex magnetic ground state. In order to obtain insight into the interplay of local-moment and itinerant ferromagnetism and thus, determine magnetic properties of

tailored Heusler compounds, it is inevitable to understand the magnetic interactions in CuMnSb that are responsible for the ordering. In this context, inelastic neutron scattering is the technique of choice to quantify the exchange coupling constants by the analysis of the dispersion of the spin wave.

In the following the structural and magnetic properties of CuMnSb are introduced. Thereafter the results of triple axis spectroscopy are presented, which were measured by Georg Brandl at EIGER, PSI, Villigen, Switzerland. The obtained data was fitted by a spinwave model, which is based on analysis of the spin wave dispersions in the transition metal oxides CoO, MnO, NiO and FeO, since these oxides order type-II antiferromagnetic as well. By fitting the model, we obtained the coupling constants of neighbouring spins, where neighbours up to the 4th order were taken into account.

6.1 Structural and Magnetic Properties of CuMnSb

As described above, half-Heusler compounds crystallise in $C1_b$, space group $F\bar{4}3m$, with a lattice constant of $a = 6.07 \text{ \AA}$, shown in figure 6.1 a) [19, 131, 132]. Castelliz found that doping NiMnSb with Cu on the Ni site gradually reduces the observed ferromagnetism [131], but it took more ten years until Endo et al. [19] identified the ordering in CuMnSb as antiferromagnetic and, further, identified CuMnSb as the very first antiferromagnetic Heusler material. By using AC-susceptibility measurements on a polycrystalline sample, Endo et al. found a Neél-temperature of $T_N = 55 \text{ K}$, a Curie-Weiss-temperature $\Theta_{CW} = -160 \text{ K}$ and a fluctuating moment of $5.6 \mu_B/\text{Mn}$. Other publications on powder of CuMnSb [20, 21] reported various Neél-temperatures ($50 \text{ K} - 62 \text{ K}$), Curie-Weiss temperatures ($-250 \text{ K} - -120 \text{ K}$), and effective fluctuating moments ($6.3 \mu_B/\text{Mn} - 5.2 \mu_B/\text{Mn}$). The varying magnetic properties are most likely related to structural defects.

Foster et al. [133] was the first, who studied the magnetic structure of CuMnSb via neutron powder diffraction on a polycrystalline sample. They confirmed the antiferromagnetic structure and reported a magnetic moment of $\mu = 3.9 \mu_B/\text{Mn}$. Furthermore, they showed that the magnetic structure of CuMnSb is a type-II antiferromagnet, with the magnetic space group $R\bar{3}c$. A type-II antiferromagnet only orders antiferromagnetically in one dimension, while the other two dimensions order ferromagnetically. In a crystal, this results in planes, where the in-plane magnetic moment exhibit ferromagnetic order, while the stacked planes order antiferromagnetically with respect to the neighbouring planes. In CuMnSb, the planes of ferromagnetic order are the $\{111\}$ planes, and the antiferromagnetic stacking is along the $[111]$ direction, as visualized in figure 6.1 b). In figure 6.1 b), the Mn sub-lattice is shown, since in CuMnSb only Mn ions carry a magnetic moment. The magnetic space group $R\bar{3}c$ of the Mn sub-lattice is shared with the well-known and understood transition metal oxides MnO, FeO, NiO and CoO.

The type-II antiferromagnetic structure intimates a frustrated system, since nearest neighbour interactions are never satisfied. Further the large ordered moments, the commensurate spin order [133], and the high saturation field suggest local-moment magnetism. In contrast to that, the high metallic conductivity [134], the low transition temperature T_N and the independence of T_N on the applied magnetic field strength

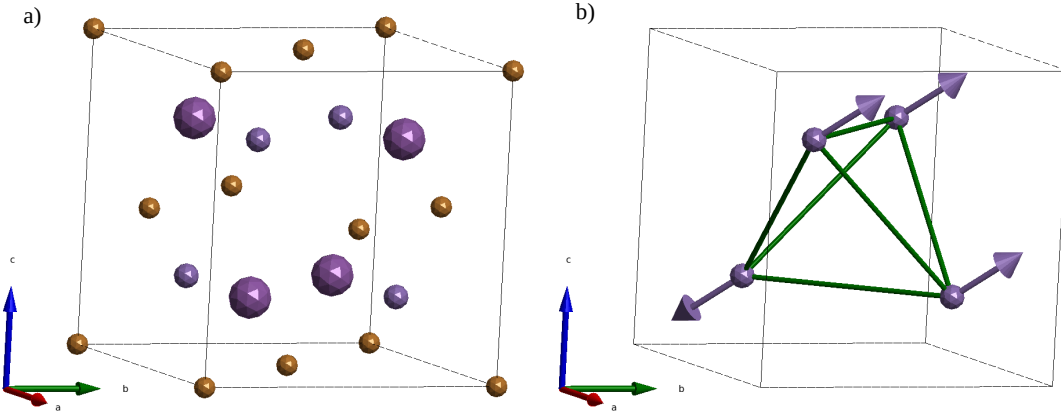


Figure 6.1: Unit cell of CuMnSb. a) crystal structure of CuMnSb. The brown spheres representing Cu-sites, the big purple Sb and the small purple Mn. b) Mn atoms and magnetic moments. The unit cell only including the Mn²⁺ ions with the respective magnetic moments, since only the Mn contributes to the magnetic moment. The magnetic structure is a type-II antiferromagnet with the stacking direction [111].

[135] suggests itinerant magnetism. Further the absence of an inversion symmetry may give rise to spin orbit coupling. Electronic structure calculations of Jeong et al. [130] yielded that CuMnSb is of semimetallic nature, i.e. a zero-gap semiconductor with a small overlap between the conduction and the valence band. Jeong et al. stated, that the antiferromagnetic phase can be heuristically described as a self-doped Cu¹⁺Mn²⁺Sb³⁻ system, where the heavy mass electrons and light valence mass holes independently mediate magnetic interaction between neighbouring spins. These two mechanisms possibly raise competing local-moment and itinerant magnetism as it is known in EuB₆ [136].

The *ab initio* calculations based on a Heisenberg model performed by Máca et al. [18] suggests that type-II antiferromagnetism might not be the ground state of a perfect CuMnSb crystal, instead a way more complex structure is expected. They report that the experimentally observed antiferromagnetic structure is stabilised by point defects. Already small concentrations of Mn interstitials or Mn antisites on a Cu position in the order of a few percent promote the antiferromagnetic ordering in the $\langle 111 \rangle$ direction [18]. Furthermore geometric frustration may also play a role as the ratio $f = -\Theta_{CW}/T_N \approx 3$ and systems with $f > 1$ are considered as frustrated [137].

Regnat et al. [22] reported the first results on a high-quality single crystal. It was grown as part of the PhD thesis of Andreas Bauer at the Physics Department of the Technical University of Munich using the optical floating-zone technique. The magnetisation of CuMnSb was measured along different crystal orientations versus the temperature at various fields ranging from 1-9 T. Regnat et al. argued, that the field independence of T_N and the small absolute magnetisation in combination with the weak anisotropy rather hint for strong isotropic exchange interactions, in favour of the previously discussed itinerant

magnetism. Further, an additional phase transition at $T^* = 34$ K below $T_N = 55$ K was reported, independent of applied field strength and direction, observed by magnetisation measurements. Their sample was characterised by a fluctuating moment of $\mu \approx 4 \mu_B/\text{Mn}$ and a Curie-Weiss temperature of $\Theta_{CW} = -160$ K.

With powder neutron diffraction prior results were confirmed and moreover the magnetic structure of the additional phase was revealed. The magnetic space group changes from $R[\text{I}]3c$ to $C[\text{B}]c$, more precisely, the spin orientation is slightly canted from $\langle 111 \rangle$ by $\delta \approx 14^\circ$ [22]. This result does agree with the calculations by Máca [18] suggesting that collinear antiferromagnetism is not the ground state of *CuMnSb* and underlines the importance of defects and disorder, stabilising long-range order.

6.2 Measurement strategies

The interaction mechanism of the antiferromagnetic phase in *CuMnSb* has a multitude of unresolved issues and to understand the magnetic ground state it is inevitable to quantise the coupling constants within the magnetic phase. The coupling constants can be determined by measuring the dispersion of the spin waves and finding a descriptive model. Since a high-quality single crystal is available, TAS is a very good tool as it is possible to measure precisely specific directions in reciprocal space, which is necessary to fit precisely a model for the spin wave dispersion to the acquired data. A big data set, which covers a broad range in reciprocal space is of advantage since one avoids overfitting or multiple parameter sets yielding similar results. The measurements presented in the following paragraphs were carried out by Georg Brandl on a TAS at EIGER, PSI, Villigen, Switzerland. The momentum transfer $\mathbf{Q} = (h, k, l)$ is given in reciprocal lattice units (rlu), where $1 \text{ rlu} = 1.032 \text{ \AA}^{-1}$ for *CuMnSb* with a lattice constant of $a = 6.088 \text{ \AA}$.

First, the temperature dependence of the energy of a single magnon was measured to see if the additional phase is visible in the magnon excitation energy as reported by Regnat et al. [22] and to determine the transition temperature T^* of the additional phase and the Néel-temperature T_N . For that, the momentum transfer in TAS was kept fixed at $\mathbf{Q} = (0.55, 0.5, 0.5)$ rlu, where one observes a strong magnon mode. The energy transfer was scanned from -5 meV to 10 meV at every temperature step. The temperature was increased in steps of 5 K ranging from 5 K up to 65 K.

For the characterisation of the spin canted phase at low temperatures, the dispersion of the magnon mode was measured at $T \approx 2$ K. In total ten different paths in \mathbf{Q} were scanned and at each \mathbf{Q} point the energy was scanned. Thus, a two dimensional (E, Q) -map may be created for every of the ten \mathbf{Q} scans. The typical step size along the paths in \mathbf{Q} is $\delta q = 0.05$ rlu, where q is the varying parameter within the three components of \mathbf{Q} . The energy scans were typically performed from 0 meV to 12 meV with a step size of $\delta E = 0.5$ meV. The measurement of the energy loss was omitted, since any inelastic signal is strongly reduced due to the Bose factor. All scans were performed in the reciprocal plane formed by the vectors $[100]$ and $[011]$, because it allows simultaneous access to the $[100]$, $[011]$, and $[111]$ directions. The ten Q -scans, that are displayed in figure 6.2, were chosen such, that a large area is covered. However, the magnetic form factor decreases

6.3 Temperature dependence of magnon excitation energy

rapidly with increasing \mathbf{Q} , limiting the range of reciprocal space that is useful for magnon measurements [23].

Every line in figure 6.2 corresponds to a scanned (E, \mathbf{Q}) -map, whose paths in \mathbf{Q} are listed on the right hand side with 'q' as varying parameter. The blue dots are the reciprocal lattice points of the nuclear lattice. The black lines denote the first Brillouin zone around the (111) position, while the Brillouin zone of neighbouring cells are separated by the dashed lines.

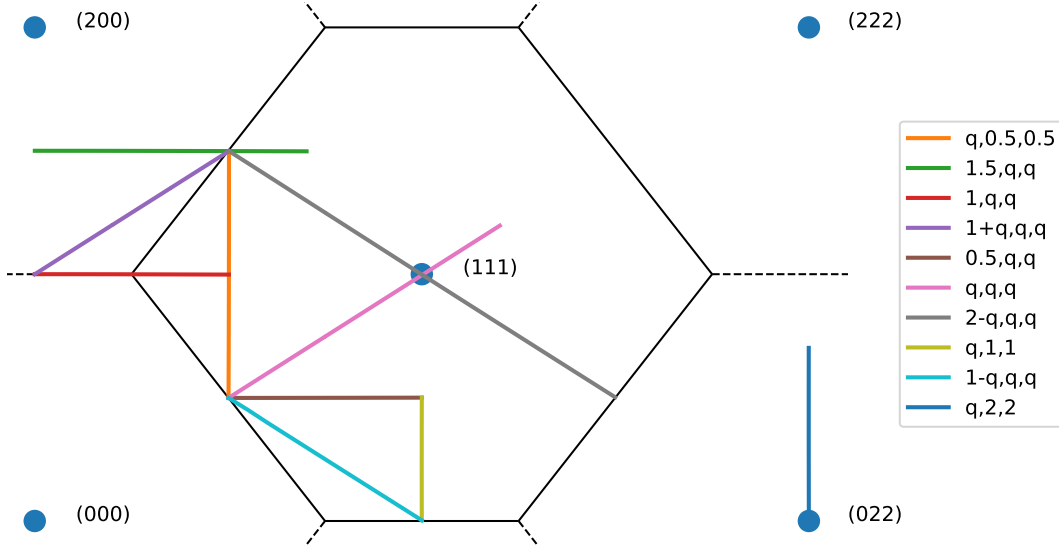


Figure 6.2: A two dimensional projection of the $\langle 100 \rangle\text{-}\langle 011 \rangle$ reciprocal lattice plane. The coloured lines correspond to the performed (E, \mathbf{Q}) scans and are labelled on the right legend. The parameter q denotes which components of \mathbf{Q} are varied within the scan. The blue dots are the reciprocal lattice points of the nuclear lattice. The black lines denote the first Brillouin zone of the (111) point, while the Brillouin zone of neighbouring cells are separated by the dashed lines.

6.3 Temperature dependence of magnon excitation energy

The sixteen energy scans performed at every temperature are displayed in appendix B.1. One exemplary energy scan, which was done at $T = 32.5$ K, is shown in figure 6.3 (a). The blue dots show the measured intensity in dependence of the energy transfer. At $E = 0$, there is the incoherent signal with two broader peaks next to it, one on the energy gain side the other on the energy loss side, originating from inelastic scattering. Close to the incoherent peak, there is a very sharp and strong signal at $E \approx 0.34$ meV, which is identified as a spurious signal. In figure 6.3 (b) the same energy scan is shown after removal of the spurious signal at $E \approx 0.3$ meV. Figure 6.3 (c) shows all energy scans that were performed at different temperatures, which are summarised in a temperature-energy

map. The measured intensity is encoded by the colour scale on the right. The intensity of the inelastic signal on the energy gain side is higher compared to the energy loss side, due to the Bose factor. The blue dots display the peak positions of the inelastic signal on the energy gain side. With increasing temperature, the inelastic peak position shifts towards smaller energy transfers until it becomes $E = 0$ at $T_N = 57$ K. At $T^* \approx 34$ K, there is a small kink in the dependence of the peak position on T .

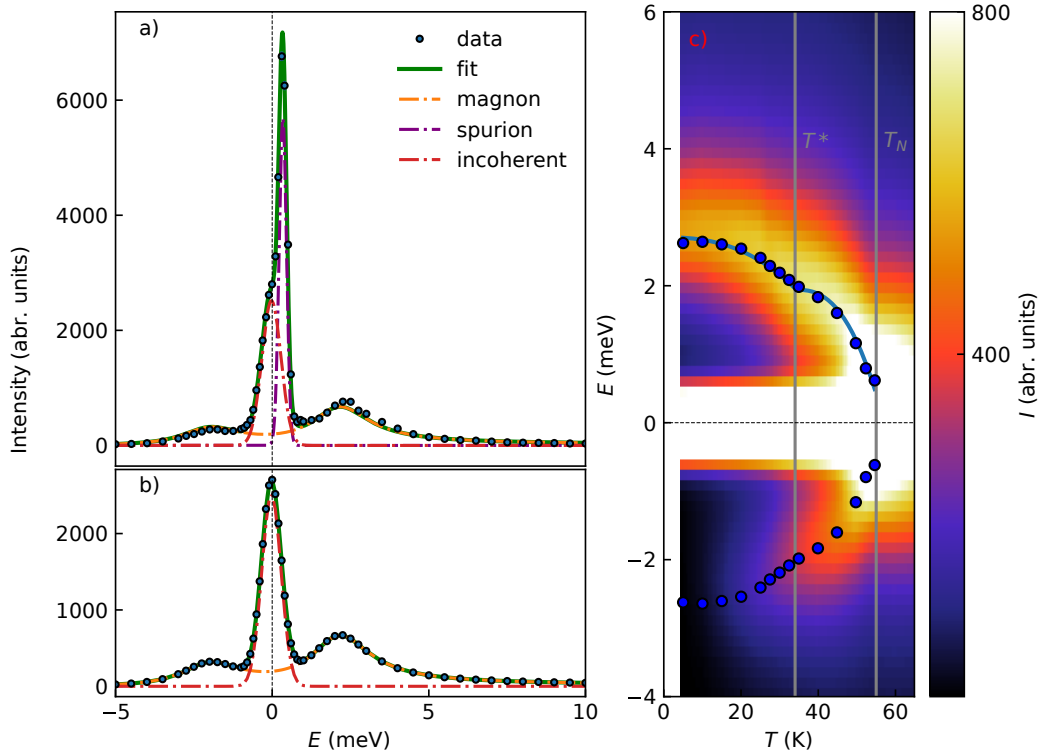


Figure 6.3: Temperature-energy scan at $Q = (0.5, 0.5, 0.5)$. a) typical energy scan is shown. The blue dots are the intensity in dependence of the energy transfer. The dashed lines indicate the following components: The magnon mode (orange), the incoherent scattering (red) and the spurious signal (purple). The green solid line corresponds to the sum of all components. b) The same energy scan as in a) is shown, but – for better visualisation – the fitted spurious is subtracted from the data and the model. c) Intensity of all energy scans in dependence of the temperature. The energy scans for the different temperatures are summarised as a interpolated colour map. Hereby, the spurious signal is also subtracted. The blue dots indicate the peak positions of the magnon mode, which were obtained by the fitting procedure of the energy scans. The blue line is the fitted model of the two magnetic phases with different structures.

6.3 Temperature dependence of magnon excitation energy

The energy scans are modelled for every applied temperature. The model

$$I_{\text{model}}(E, \mathbf{Q}) = I_{\text{inc}}(E) + I_{\text{spurion}}(E) + I_{\text{magnon}}(E) + C, \quad (6.1)$$

consists of four contributions: The incoherent scattering is described by a Gaussian function

$$I_{\text{inc}}(E) = I_{0,\text{inc}} \times \exp\left(-\frac{E^2}{2\sigma_{\text{inc}}^2}\right), \quad (6.2)$$

the spurious signal, also described by a Gaussian function

$$I_{\text{spurion}}(E) = I_{0,\text{spurion}} \times \exp\left(-\frac{(E - E_{\text{spurion}})^2}{2\sigma_{\text{spurion}}^2}\right). \quad (6.3)$$

The inelastic scattering by the magnon excitation $I_{\text{magnon}}(E)$, is described by the spectral weight function as defined in equation (2.32),

$$I_{\text{magnon}}(E) = \frac{1}{2\pi} \langle n + 1 \rangle I_{0,\text{Lorentz}} \times \left(\frac{\Gamma}{(E - E_0(T))^2 + \Gamma^2} + \frac{\Gamma}{(E + E_0(T))^2 + \Gamma^2} \right), \quad (6.4)$$

and a constant background C , which is assumed to be independent of E and T . The incoherent signal $I_{\text{inc}}(E)$ originates from random fluctuations of the scattering length among the crystal sites and is a property of the material [23]. In general, incoherent scattering is nearly isotropic and assumed to be temperature independent within the measured temperature range. The spurious signal $I_{\text{spurion}}(E)$ at $E = 0.34$ meV is not necessarily associated with the sample itself, it can also be a systematic contamination originating from the instrumental setup. Typical origins of spurious contamination are among others higher-order neutrons, unwanted reflections and artefacts of resolution function or sample environment. A detailed explanation can be found in chapter 6 'Spurious peaks' in ref. [23]. The spurions observed in our experiments were identified as a Bragg tail from the magnetic Bragg peak at $Q = (0.5, 0.5, 0.5)$, as the position in E fits very well with where one would expect the magnetic Bragg tail and the intensity of the spurion decreases with increasing temperature. Furthermore, the signal was also measured in a monitor placed after the analyser, thus excluding it to be caused by a phonon. This monitor records the full scattered intensity without the filtering effect of the analyser crystal. As the signal is quite strong, it is most likely of elastic nature and not fully filtered by energy selection at the analyser. Due to instrumental resolution effects at our measurement position, one measures this elastic signal at seemingly finite energies.

For the fitting procedure, the $I_{\text{inc}}(E)$ (equation (6.2)) was fitted consistent for the whole data set, such that the intensity $I_{0,\text{inc}} = 2514 \pm 33$ (arb. units) and $\sigma_{\text{inc}} = 0.300 \pm 0.004$ meV are the same for all temperatures. The spurious signal $I_{\text{spurion}}(E)$ (equation (6.3)) is in terms of peak position $E_{\text{spurion}} = 0.340 \pm 0.001$ meV and peak width $\sigma_{\text{spurion}} = 0.120 \pm 0.001$ meV temperature independent, whereas the peak amplitude

decreases with increasing temperature. The magnon mode $I_{\text{magnon}}(E)$ (equation (6.4)) is the only contribution that shows temperature dependence in peak position, peak width and amplitude and is fitted with all parameters individually for every temperature. An typical example of the fitting result is shown in figure 6.3 (a) and (b) for the energy scan at $T = 32.5$ K. The three different fitted contributions are presented by the coloured, dashed lines, where the magnon is represented by the orange, the spurion by the green and incoherent scattering by the red line. The solid green line is the sum of all aforementioned contributions. All fits with the respective temperatures are shown in figure B.1.

The excitation energy of the magnon mode correlates with the magnetisation of the specimen and thus, is temperature dependent, too [60]. The energy of the magnon mode is proportional to a $T^{\frac{5}{2}}$ power law

$$E(T) \sim \left(1 - \left(\frac{T}{T_N}\right)^{5/2}\right), \quad (6.5)$$

where T_N is Néel-temperature. The small kink in the magnon mode at $T^* \approx 34$ is associated with additional phase transition of spin canting, as already reported by Regnat et al. [22]. In order to describe the magnon mode over the two different magnetic phases, a phenomenological model was applied, that includes the additional phase transition and is expressed as

$$E(T) = \begin{cases} A_1 \times \left(1 - \left(\frac{T}{T^*}\right)^{5/2}\right) + A_2, & \text{for } T < T^* \\ A_2 \times \left(1 - \left(\frac{T}{T_N}\right)^{5/2}\right) & \text{for } T^* < T < T_N \end{cases}, \quad (6.6)$$

with the amplitudes A_1 and A_2 , the Néel-temperature T_N and the transition temperature for the canted phase T^* . The resulting fit of the model is shown in figure 6.3 (c). The fit yields $A_1 = 0.73 \pm 0.05$ meV, $A_2 = 1.97 \pm 0.04$ meV, $T^* = 34.2 \pm 1.3$ K for the spin canting transition and $T_N = 57 \pm 1$ K for the Néel-temperature. With a reduced $\chi^2 = 1.15$, the applied model describes the data very well. The fitting results agrees perfectly with the reported results on CuMnSb by Regnat et al [22]. Especially the noticeable transition at $T^* = 34$ was reproduced at the very same temperature as the magnetisation measurements of Regnat et al.. This structural change agreed very well with the theoretical consideration of Maca et al. [18], that at low temperatures, the magnetic system of CuMnSb takes a more energetically favourable ground state. The two competing magnetic mechanisms predicted by electronic structure calculations of Jeong et al. [130] are possible explanation for the present frustration and the resulting phase transition at low temperatures.

6.4 Dispersion

In the following, first the analysis of the energy scans along different Q -paths is described. Subsequently a model describing the dispersion is presented. Based on the excitation energies of the magnon mode obtained by the fits of the energy scans, the model is fitted

to the measured magnon mode. Thereafter the thereby obtained results are presented and discussed.

6.4.1 Energy Scans

The 116 energy scans performed for different \mathbf{Q} values are displayed in appendix B.2. Four exemplary energy scans performed at are shown in figure 6.4. The blue dots show the measured intensity in dependence of the energy transfer. The hollow blue circles are data points that are not taken into account for the later fitting procedure, as these are contributions of either the incoherent signal at $E = 0$ or a spurious signal, which disturb the later fit of the magnon. The small inset in the top left corner shows the position of the energy scan in the reciprocal space. The exact Q -point, where the energy scan was performed is shown in the top right.

For the analysis of the dispersion of the magnon mode, all energy scans of the different \mathbf{Q} directions were modelled. In comparison to section 6.3, the model includes only the magnon mode

$$I_{\text{model}}(E, \mathbf{Q}) = I_{\text{magnon}}(E) \quad (6.7)$$

which analogous to equation (6.4) is described by the spectral weight function. In contrast to section 6.3, the incoherent and spurious signal were not included in the model, since in the displayed measurements the step size in energy was bigger and only positive energy transfers were measured. Hence, the incoherent and spurious scattering are only represented by three data points next to $E = 0$ and are present as one strong, sharp peak, which makes any later analysis attempt unreasonable. Instead, the three data points close to $E = 0$ are excluded from the fitting procedure and the model does not consider any incoherent contribution. Furthermore, a few energy scans show a sharp small peak, as it is visible in figure 6.4 at $Q = (1.4, 0.6, 0.6)$ at $E \approx 9$ meV. This peak shifts linearly with a very steep slope to higher energy as the distance to $Q = (1, 1, 1)$ increases. This mode was identified as a spurious Bragg tail originating from the elastic nuclear scattering at $\mathbf{Q} = (1, 1, 1)$ and is – similar to the Bragg tail in section 6.3 – visible in the monitor after the analyser. For the same reasons as for the strong peaks close to $E = 0$, this mode was also carefully excluded, in order to not disturb the fitting process. The energy scan in figure 6.4 for $Q = (1.2, 1.2, 1.2)$ is the only energy scan that shows this atypical shape of two separated sharp peaks. This spectral feature is not understood.

As fitting routine the 'lmfit' package in python was used [138]. The fitting procedure of this model converged well and the results of all fits are presented in appendix B.2, each labelled with the respective Q position. A resolution function of the instrument was not included, because it would not have a significant influence as the magnon peak is very broad. The fit usually agrees very well with the measurements, as shown in figure 6.4 for $Q = (0.5, 0.5, 0.5)$. If the magnon mode comes close to $E = 0$ meV, there is no clearly visible peak, however, the peak tails are sufficient for a reasonable fit, as one can see in figure 6.4 at $Q = (0.1, 2, 2)$. For a few energy scans, the measured peak has rounded compared to the spectral weight function, as it is visible in figure 6.4 at $Q = (1.4, 0.6, 0.6)$. One possible explanation that this mode consists of two very close modes, which are not distinguishable, however fitting two Lorentzian peaks did not improve the results.

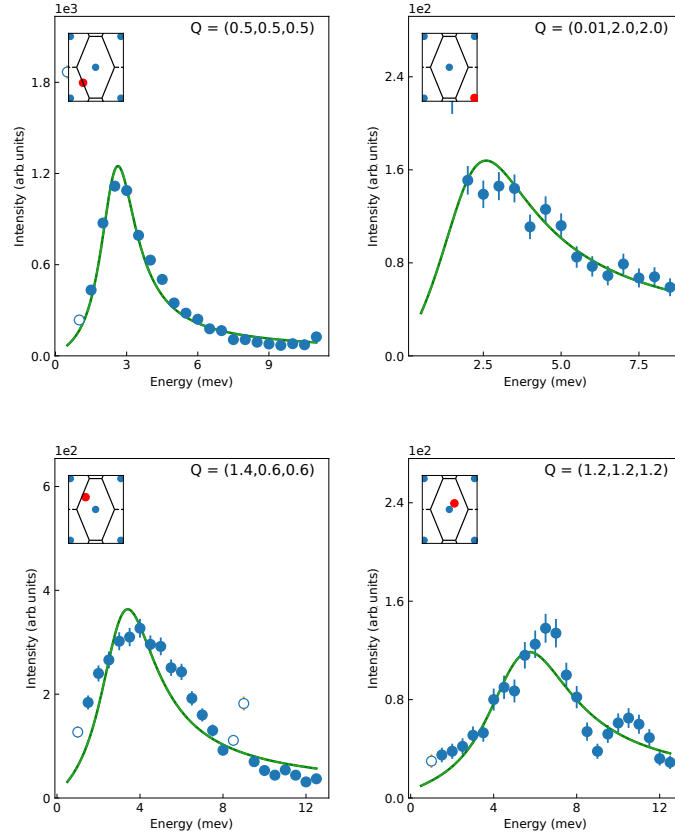


Figure 6.4: Exemplary energy scans at the given Q -positions. The dots show the measured intensity in dependence of the energy transfer. The hollow blue circles are data points that are not taken into consideration in the fitting procedure. The green solid line denotes the result of the fitting procedure. The small inset in the top left corner shows the position of the energy scan in the reciprocal space. Each scan is labelled with the exact Q -point, where the energy scan was performed.

Another possible explanation is that the spectral weight function is not sufficient in the form as it was applied. However, since the resulting fit agrees well with amplitude and peak position, the results were still taken into account in the further analysis of the magnon mode, but with the according higher error.

The amplitude of the magnon mode versus Q is shown in figure 6.5. The amplitude directly correlates with the magnetic structure factor and is fitted by Lorentzian functions, which describes the obtained amplitudes very well with the magnetic structure factor being high at $Q = (0.5, 0.5, 0.5)$, $Q = (1.5, 0.5, 0.5)$ and $Q = (0.5, 1.5, 1.5)$, while vanishing at $Q = (1, 1, 1)$. Less stronger local maxima of the magnetic structure factor are found at $Q = (1, 1, 1)$, $Q = (0.4, 1, 1)$, $Q = (1, 0.5, 0.5)$, $Q = (0, 2, 2)$ and $Q = (0.5, 2, 2)$.

The line width of the magnon mode is expected to be correlated with the magnon

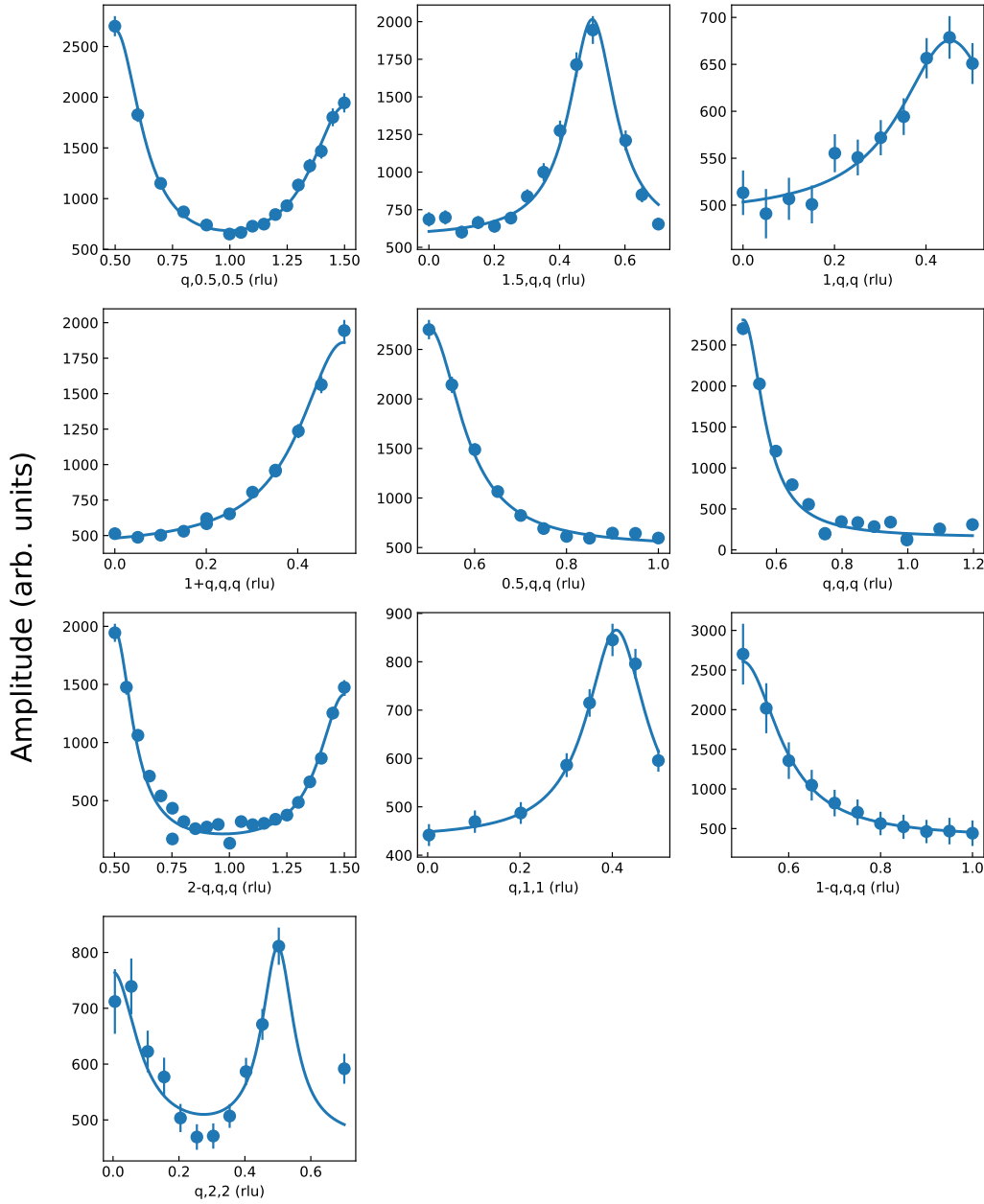


Figure 6.5: Amplitude of the magnon mode. The blue dots show the amplitude of the magnon signal in dependence of the momentum \mathbf{Q} . The amplitudes were obtained by fitting the energy scans, shown in appendix B.2, with spectral weight function equation (6.4). The amplitudes are fitted with Lorentzian functions.

energy. The results obtained by the fitting procedure, given in appendix B.3, show that in most directions the magnon line width is correlated with the magnon energy. However, in the directions $\mathbf{Q} = [1, q, q]$, $\mathbf{Q} = [1 + q, q, q]$ and $\mathbf{Q} = [1 - q, q, q]$ the magnon line width

and magnon energy appear uncorrelated or even partly anticorrelated. Until now no descriptive model could be developed, which can explain this behaviour. Further, including the resolution function of the instrumental setup is inevitable for the development of a line width model.

6.4.2 Model of Spin Wave Dispersion

For the analysis of the dispersion of the spin wave, a model was developed, which was already successfully applied for the well-known materials NiO [139], MnO [140, 141], and FeO [142]. These metal oxides are likewise CuMnSb type-II antiferromagnets, where the antiferromagnetic planes stack along [111]-direction. Furthermore, they could have been all described by a nearly identical spin wave model, even though the models are written down in different forms within the literature. The very first formalism to describe the spin wave dynamics of collinear antiferromagnetism was introduced by Lines [143] for MnO. Following ref. [143], the Hamiltonian for spin waves is expressed as

$$\mathcal{H} = \sum_j \sum_{\langle i, \delta_j \rangle} J_j \mathbf{S}_i \mathbf{S}_{i+\delta_j} + \sum_i D_1 (S_i^x)^2 + \sum_i D_2 (S_i^y)^2. \quad (6.8)$$

Hereby the z -axis is assumed to lie along the spin direction [111], whereas the y - and x -axis lie in the [111]-plane. \sum_i runs over all the spins in the lattice and $\sum_{\langle i, \delta_j \rangle}$ denotes the sum of all distinct pairs at \mathbf{r}_i and $\mathbf{r}_i + \delta_j$, coupled through an exchange interaction J_i . The index j increases with the order of neighbouring spins, e.g. $j = 1$ denote the nearest neighbours and $j = 2$ the next nearest neighbours, etc. D_1 and D_2 are the anisotropy factors which correspond to the strength of the out-of-plane and in-plane anisotropy, respectively.

By introducing the spin-wave creation and annihilation operators of Holstein and Primakoff the Hamiltonian can be diagonalised [143, 144]. The resulting dispersion relation of the magnon mode is given by [139, 141]

$$E(\mathbf{Q})_{sw}^{\pm} = S \cdot \left[(A(\mathbf{Q}) \mp B(\mathbf{Q}) + 2D_1) (A(\mathbf{Q}) \pm B(\mathbf{Q}) + 2D_2) \right]^{\frac{1}{2}}, \quad (6.9)$$

where

$$A(\mathbf{Q}) = \sum_j^{\uparrow\uparrow} \sum_{\delta_j} J_j e^{i\mathbf{Q}\delta_j} + \sum_j^{\downarrow\uparrow} z_j J_j - \sum_j^{\uparrow\uparrow} z_j J_j, \quad (6.10)$$

and

$$B(\mathbf{Q}) = \sum_j^{\downarrow\uparrow} \sum_{\delta_j} J_j e^{i\mathbf{Q}\delta_j}. \quad (6.11)$$

As the 12 nearest neighbours in a type-II antiferromagnet are split into two sets of 6 parallel and 6 antiparallel spins, the sums are performed over these two set individually. Hereby, the $\uparrow\uparrow$ and $\downarrow\uparrow$ above the summation indicate the sum over parallel or antiparallel spins. The anisotropy terms D_1 and D_2 are the only terms that lift the degeneracy of

$E(\mathbf{Q})_{\pm}$. The integer z_j is the number of equivalent neighbours and the total spin of the Mn^{2+} ions is $S = \frac{5}{2}$. In the metal oxides, only the nearest and next nearest neighbours are considered to contribute significantly to the spin wave dispersion [139, 140, 141, 142]. Thus, equations (6.10) and (6.11) can be expressed as

$$\begin{aligned} A(\mathbf{Q}) &= 6J_1^+ - 6J_1^- + 2J_1^- C_1 + 6J_2 \\ B(\mathbf{Q}) &= 2J_1^+ C_2 + 2J_2 C_3 \end{aligned} \quad (6.12)$$

where, with $\mathbf{Q} = (q_x, q_y, q_z)$,

$$\begin{aligned} C_1 &= \cos(\pi(q_x - q_y)) + \cos(\pi(q_y - q_z)) + \cos(\pi(q_z - q_x)) \\ C_2 &= \cos(\pi(q_x + q_y)) + \cos(\pi(q_y + q_z)) + \cos(\pi(q_z + q_x)) \\ C_3 &= \cos(2\pi q_x) + \cos(2\pi q_y) + \cos(2\pi q_z) \end{aligned} \quad (6.13)$$

Following the notation of Lines [143], the interactions of the nearest neighbours are J_1^+ and J_1^- , where the plus sign denotes coupling between antiparallel neighbours and the minus sign between parallel neighbours. For more distant neighbours such in-equivalences were omitted. Even though, a model up to the second order was sufficient for modelling of the spin wave dispersion in transition metal oxides, it might be not for CuMnSb. Since, for CuMnSb characteristics of different interaction mechanisms were reported, e.g. itinerant exchange [130, 135], the applied model might be insufficient as the interaction range might exceed the next nearest neighbours. In this context, the introduced model was expanded by more distant neighbours of order 3 and 4. Thus, equations (6.10) and (6.11) are expressed as [139]

$$\begin{aligned} A(\mathbf{Q}) &= 6J_1^+ - 6J_1^- + 6J_2 + 2J_1^- C_1 + 2J_3 C_4 - 12J_4 + 2J_4 C_6 \\ B(\mathbf{Q}) &= 2J_1^+ C_2 + 2J_2 C_3 + 2J_3 C_5 \end{aligned} \quad (6.14)$$

where C_1 , C_2 and C_3 are the same as given in equation (6.13). C_4 , C_5 and C_6 are

$$\begin{aligned} C_4 &= 2 \left[\cos(\pi(q_x + q_y)) \cos(2\pi q_z) \right. \\ &\quad + \cos(\pi(q_y + q_z)) \cos(2\pi q_x) \\ &\quad \left. + \cos(\pi(q_z + q_x)) \cos(2\pi q_y) \right] \\ C_5 &= 2 \left[\cos(\pi(q_x - q_y)) \cos(2\pi q_z) \right. \\ &\quad + \cos(\pi((q_y - q_z)) \cos(2\pi q_x) \\ &\quad \left. + \cos(\pi((q_z - q_x)) \cos(2\pi q_y) \right] \\ C_6 &= 2 \left[\cos(2\pi q_x) \cos(2\pi q_y) \right. \\ &\quad + \cos(2\pi q_y) \cos(2\pi q_z) \\ &\quad \left. + \cos(2\pi q_z) \cos(2\pi q_x) \right]. \end{aligned} \quad (6.15)$$

The inclusion of more distant neighbours results contribute terms to the dispersion model, that are able to describe higher frequency Fourier components in the magnon dispersion.

6.4.3 Magnon Dispersion

Both, the 2nd order as well as the 4th order model were fit to the dispersion of the magnon. The resulting parameters are shown in table 6.1. The respective fits of the

coupling constant	NN and NNN (meV)	up to 4th NN (meV)
J_1^+	0.066 ± 0.005	0.104 ± 0.005
J_1^-	0.063 ± 0.004	0.086 ± 0.004
J_2	0.210 ± 0.003	0.327 ± 0.012
J_3		0.092 ± 0.004
J_4		0.033 ± 0.004
D_1	0.152 ± 0.010	0.080 ± 0.006
D_2	0.146 ± 0.004	0.066 ± 0.002
red. χ^2	11.5	5.2

Table 6.1: Results obtained in the fitting process. The model of the first column includes only the nearest neighbours (NN) and the next nearest neighbours (NNN). The model of the second column include up to the fourth next neighbours.

model equation (6.14) are illustrated together with the measured data in figure 6.6. The colours of the dispersions given as solid lines are following the same pattern as in figure 6.2 and the path in reciprocal space is illustrated in the small inset in the upper left corner. The gray-scaled background shows intensity of the (E, \mathbf{Q}) -map. The blue dots are the peak positions of the magnon mode, which were obtained from the fits of the energy scans. The Miller indices above the figure show the respective reciprocal lattice points along the path in \mathbf{Q} . For most of the \mathbf{Q} -directions the fitting procedure worked well, however, for $[q, \frac{1}{2}, \frac{1}{2}]$, $[q, 1, 1]$ and $[q, 2, 2]$ the model does not yield a optimal match. One notes, that only one of the two modes is plotted, since the anisotropy factors D_1 and D_2 are small compared to the exchange couplings. The modes $E(\mathbf{Q})_{sw}^-$ and $E(\mathbf{Q})_{sw}^+$ only differ in the vicinity of magnetic Bragg peaks, their difference in energy is $\Delta E(\mathbf{Q})_{sw}^\pm < 0.15$ meV, and are, thus, nearly degenerate in the measured range.

Comparing the two different models, the reduced χ^2 of the 4th order model decreased more than half in comparison to the 2nd order model, that includes only nearest and next nearest neighbours. Although no exact Bayesian model evaluation was performed, the smaller reduced χ^2 and the well fitted data suggest, that the expansion of the model is valid.

The deviation of the fit and the data along the paths $[q, \frac{1}{2}, \frac{1}{2}]$, $[q, 1, 1]$ and $[q, 2, 2]$ might be due to fact that the model is optimised for transition metal oxides exhibiting the magnetic space group R[1]3c, while in CuMnSb, as mentioned in section 6.1, the magnetic moments are slightly tilted from $[1, 1, 1]$ to the direction $[0, 1, 1]$ by an angle of $\delta \approx 14^\circ$, resulting in the magnetic space group C[B]c and indicating a different ground state. Furthermore, the in-equivalence of parallel and antiparallel neighbours was only considered for nearest neighbour interaction.

The coupling constant J_2 is larger, but of the same order of magnitude as J_1^\pm . Although

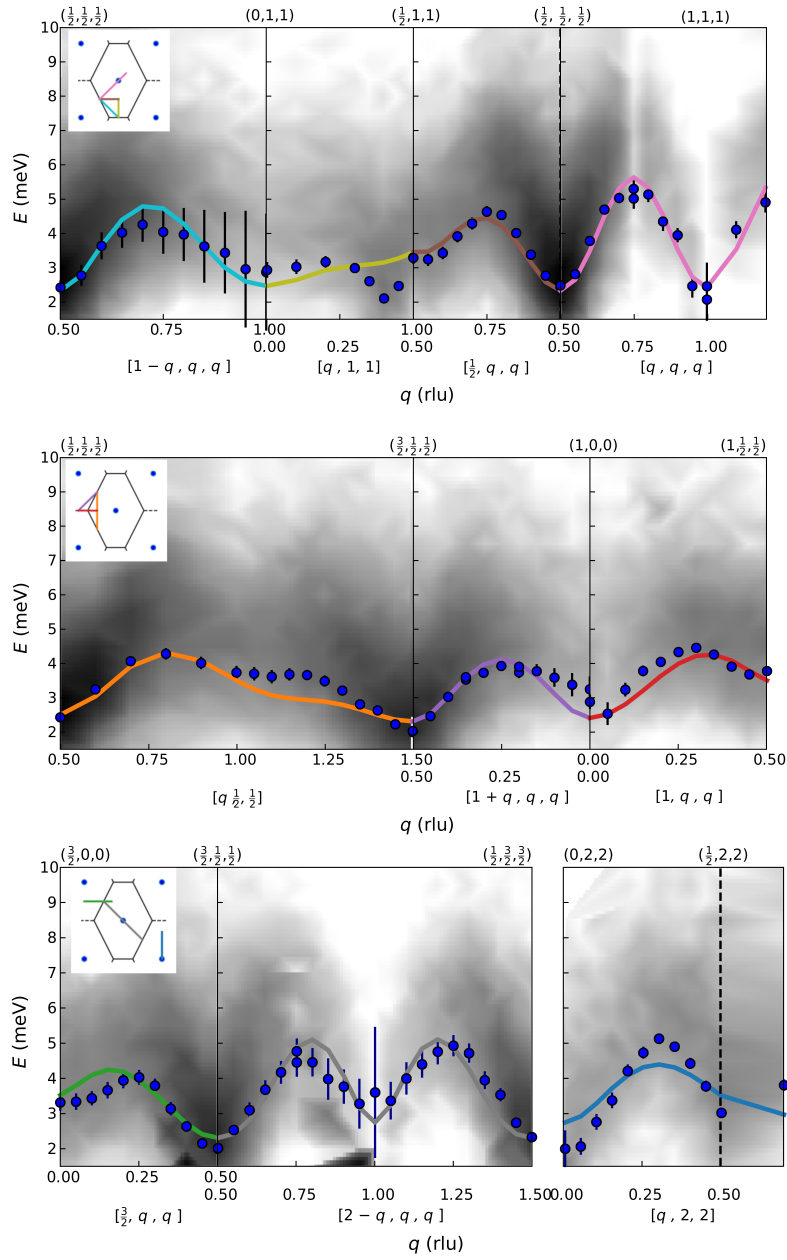


Figure 6.6: Results of the spin wave model. The colour map in the background indicates the measured intensity $S(E, Q)$ in grey scale, where darker indicates higher intensity. The blue data dots are the respective peak positions. The fitted spin wave modes are given by the coloured lines. The path in reciprocal space is given in the small inset in the upper left corner. Above the reciprocal lattice points are indicated. Below the specific direction is labelled, where 'q' is the varying parameter.

it is necessary that $J_2 > J_1^\pm$ to obtain type-II antiferromagnetism, the closeness of these values indicates strong frustration. This might be the origin of the low transition temperature compared to transition metal oxides even though the exchange constants are of a similar order of magnitude. J_3 is of the same size as J_1^\pm , which again shows that it is necessary to include more distant neighbours compared with the transition metal oxides. The coupling constant between the 4th nearest neighbours J_4 is with $J_4/J_2 \approx 0.1$ small compared to the most dominant coupling constant J_2 and gives just local small corrections to the model's fit. Nevertheless, the contributions of the 3rd and 4th order neighbours lead to significant improvement and are therefore not negligible. This shows, that a local-moment magnetism is not sufficient to describe the magnetic interactions of CuMnSb as the interaction range suggests an interaction mechanism of longer range. The strong frustration might originate from the two competing mechanism predicted by Jeong et al. [130]. The very small contribution of the out-of-plane and in-plane anisotropy D_1 and D_2 are agreeing excellently with the reported weak anisotropy of ref. [22]. Even though the obtained anisotropy is quantitatively small, it has a significant impact on the energy gap of the spin wave dispersion in the applied model. The two branches of E_{sw}^\pm are only separated by the anisotropy terms as it can be seen in equation (6.9). Although the two branches are not distinguishable within the resolution of a triple axis measurement, the small splitting of the magnon modes $\Delta E(\mathbf{Q})_{sw}^\pm < 0.15$ meV serves as a possible explanation for the broad peak of the measured signal as one comes closer to the magnetic Bragg peaks.

A possible option to improve the spin wave model would be to include the symmetry breaking of the spin canting and to implement possible antisymmetric exchange interactions. Since the corresponding Hamiltonian would drastically increase in complexity, in a future investigation numerical calculations would be of advantage. To take even more distant neighbours into account, would results in higher frequent Fourier components than already included in equation (6.15) to the model. However, since the model follows in general the trend of the measured data, higher orders would lead to more fitting parameters than can be justified by the data and are therefore not reasonable. Furthermore, spin-flip dependent measurements would be also advantageous, in order to distinguish between spin wave excitations and lattice vibrations.

6.5 Summary

The results of inelastic neutrons scattering on the high-quality single crystal CuMnSb are reported. Temperature dependent energy scans of magnon mode showed in general the expected temperature dependence of a magnon mode. However, a kink in the energy temperature curve reveals an additional phase transitions inside the magnetic phase, which can be described by a simple phenomenological model. The observed kink agrees perfectly with the change in the magnetic space group R[1]3c to C[B]c as reported by ref. [22], corresponding to a canting of the magnetic moments in the crystal.

The analysis of the spin wave dispersion is performed for low temperatures data, where ten different paths in Q were measured. The measurement of the spin waves along

each \mathbf{Q} -directions results in a (E, \mathbf{Q}) -map revealing the energy dispersion of the magnon mode for the corresponding direction. Due to the similar magnetic structure of a type-II antiferromagnet with the metal oxides, the same Hamiltonian is used and fitted globally to the data, where interactions up to the 4th nearest neighbours are included. The obtained parameters showed that the system is magnetically frustrated, which explains the low transition temperature of CuMnSb compared to other known systems and may be related to the spin canting at T^* . The fact that up to the 4th next neighbours need to be included into the model, shows that CuMnSb has indeed partially contributions of long range interaction mechanisms, i.e. itinerant interaction. This conclusion agrees well with the considerations of Jeong et al. [130] of two different competing interaction mechanism.

7 Conclusion

In many magnetic materials the mechanisms of the underlying interactions are still not fully understood. Neutron scattering is the technique of choice to study magnetism on a microscopic scale as one is able to obtain quantitatively the exchange interaction between of neighbouring spins. However, with the increasing complexity in magnetic solids, one often reaches the limits of established neutron techniques, i.e. resolution, accessible energy and momentum range or applicable environment. The development of new, more sophisticated scattering techniques becomes necessary to deepen the insight into the condensed matter magnetism.

In this context, the development and the implementation of the MIEZE add-on for the triple axis spectrometer MIRA is presented in chapter 2. The combination of the MIEZE technique with a TAS drastically improves the energy resolution, while maintaining the resolution and accessible range in momentum. Especially, for magnon excitations at small momentum transfers, where the excitation energy is small, a high energy resolution is necessary. Further, with spin echo techniques the line width can be measured. Thereby one can investigate quasielastic processes or determine the lifetime of an inelastic excitation. The performance of the MIEZE technique strongly depends on the initial contrast, as for this spectrometric method the transferred energy is deduced from the reduction of the initial contrast. In chapter 3, the first test results of the MIEZETOP performance were evaluated. The tests showed that the adiabatic transition between the polariser and the $\pi/2$ -flipper was not fully performed, due the strong spatial restriction of the setup. Further, for increasing echotimes τ_{MIEZE} , the magnetic fields of the B_0 coils of the RF-flippers reach into the respective $\pi/2$ -flippers next to the RF-flipper, disturbing the flipping procedure. These two factors reduce the initial contrast and, thus, reduce the accessible range in echotime τ_{MIEZE} and quality of the MIEZE spectroscopy. Additionally, MIEZE in diffraction and triple axis mode in comparison to forward scattering was analysed. The different scattering geometries are expected to reduce the initial contrast, because the path length across the cross section of the neutron differs. In both configurations, the dependency of the contrast with respect to the detector angle showed the expected behaviour. However, the overall reduction factor was practically not applying at all and the measured contrast was higher than expected. Only for long echotimes, there was a significant reduction in contrast, but still less than expected. Even though, there was no explanation yet found, this shows that the combination of MIEZE and TAS is in principle possible and might offer an even better performance than expected. Unfortunately, due to the temporal shut-down of the FRM2 reactor operation, no further experiments could be performed.

Nevertheless, future improvements are inevitable, especially for the adiabatic transition and the mutual disturbance of the coils, as it would drastically boost the performance of

7 Conclusion

the setup since the initial contrast is the most limiting factor. The simplest approach is to stretch the MIEZE setup, which would, however, reduce the flexibility of the whole instrument. A different approach is to shield the magnetic fields, which would improve the situation of mutual disturbance of the B_0 coils, but the problems of the adiabatic transition would still be unanswered. Further a detector, which is movable along the beam direction, would improve the tuning procedure of the various MIEZE conditions and, thus, also increase the initial contrast.

Two materials, whose magnetic interaction is not fully understood are $\text{BaCdV}(\text{PO}_4)_2$ and CuMnSb . Both materials order antiferromagnetically and exhibit competing interactions resulting in magnetic frustration.

The quasi two dimensional antiferromagnet $\text{BaCdV}(\text{PO}_4)_2$ is a candidate for exhibiting a spin nematic phase, where competing interaction between the nearest and next nearest neighbours are expected to lead to a dimerisation of neighbouring spins. In chapter 4 the inelastic time-of-flight measurements of the powder sample $\text{BaCdV}(\text{PO}_4)_2$ at $B = 0$ T and $B = 8$ T are presented. By modelling the powder spectra, the exchange constants between nearest and next nearest neighbours were extracted. However, in comparison to concurrently performed single crystal measurements in magnetic saturation by Bhartiya et al., the coupling constants obtained by us do not agree with the single crystal measurements. Oppositely, the exchange couplings extracted by Bhartiya et al. do not agree with our $B = 0$ T measurements. Because both research groups used the same model for describing their measurements on the same material, the two different sets of parameters showed that both data sets were not sufficient to yield the correct exchange couplings. In this context, calculations are prepared, where the measurements of both research groups are included and will be performed as soon as the super computer "Deep Thought" at FRM2, Garching, Germany is available again. However, single crystal measurements at various magnetic fields would be advantageous to find the correct model describing the system. The spin nematic phase stays unrevealed.

In CuMnSb , the additional phase transition within the magnetic phase has been observed using temperature dependent triple axis measurements on a single magnon excitation and was described by a phenomenological model. The obtained transition temperatures $T_N = 57$ K and $T^* = 34$ K agree very well with other reported magnetisation measurements. The dispersion of the spin waves along ten different directions in reciprocal space at $T = 2$ K were described by a model based on the results of transition metal oxides MnO , FeO , CoO and NiO , which also order as a type II antiferromagnet. The model fitted the results well, except for one crystal direction. The origin of this difference might be of the slightly different symmetry in this direction due to the spin canting at $T^* = 34$ K. The obtained coupling constants showed that the magnetic phase of CuMnSb is strongly frustrated as nearest and more distant neighbours compete in their interaction. This explains the low T_N compared to the metal oxides, although the interactions strengths are of the same order of magnitude. Furthermore, the fact that neighbours up to the 4th order had to be included into the model suggests that CuMnSb does have an itinerant interaction mechanism, additionally to the characteristics of local-moment magnetism. However, in order to improve the results of the model, spin flip dependent neutron scattering experiments could be beneficial in order to separate magnetic modes and phonon modes.

Further the same measurements in the non-canted phase $T^* < T < T_N$ should be performed to evaluate the influence of the spin canting on the magnon mode. Additionally, a modified model that includes the spin canting lead to an improved modelling of the data.

Acknowledgement

Here I would like to express my sincere gratitude to the people who supported me during my time doing my dissertation. Without them this thesis would not have been possible:

- My supervisor Prof. Dr. Peter Böni. Thank you for the opportunity for working on this thesis. Especially, I want to thank you for the independent working atmosphere and your "always open-door" policy. It was a pleasure to discuss scientific problems with you or just having a little chat.
- My mentor Dr. Robert Georgii. Thank you for your never ending support and always open ear. I really appreciate that you minimised all political and bureaucratic barriers and that you were always available (even on weekend night time).
- The team of the RESEDA beamline at FRM2, in particular Dr. Christin Franz, for their help and support in all questions about MIEZE.
- Dr. Markos Skoulatos for the introduction into the BaCdV(PO₄)₂ project, the movie nights while having beam time and his culinary supply.
- Prof. Dr. Christian Pfeiderer and Dr. Andreas Bauer. Thank you for providing the CuMnSb data and the fruitful discussions.
- My colleagues and friends from E21. Thank you for the great time we spend together, the bike tours, the Chinese hot pot sessions and the fun we had during lunch and coffee time. Christoph Herb for the weekly road trips to Weihestephan. Ran Tang for the introduction to his culinary culture. Lukas Beddrich for our MIEZE discussions and data evaluations. Especially, I want to thank Alexander Book for his four years of IT, python, emotional support and over 15 years of deep friendship. I want to thank Stefan Giemsa for his assistance concerning all technical problems. I want to thank my former working student Daniel Prelipcean for being of great assistance.
- My family for their encouragement during my thesis.
- My wife for all of her never-ending love and support. You are my source of strength from which I can draw.

Bibliography

- [1] James Chadwick. The existence of a neutron. *Proceedings of the Royal Society of London. Series A, Containing Papers of a Mathematical and Physical Character*, 136(830):692–708, June 1932. doi: 10/c6djkk.
- [2] W. M. Elsasser. Sur la diffraction des neutrons lents par les substances cristallines. *Comptes rendus hebdomadaires des séances de l'Académie des sciences*, (202):1029, May 1936.
- [3] Hans Halban and Pierre Preiswerk. Preuve expérimentale de la diffraction des neutrons. *Comptes rendus hebdomadaires des séances de l'Académie des sciences*, (203):73.
- [4] Dana P. Mitchell and Philip N. Powers. Bragg Reflection of Slow Neutrons. *Physical Review*, 50(5):486–487, September 1936. doi: 10/fbs59j.
- [5] M. Louis Néel. Propriétés magnétiques des ferrites ; ferrimagnétisme et antiferromagnétisme. *Annales de Physique*, 12(3):137–198, 1948. ISSN 0003-4169, 1286-4838. doi: 10/gmcmvz.
- [6] C. G. Shull and J. Samuel Smart. Detection of Antiferromagnetism by Neutron Diffraction. *Physical Review*, 76(8):1256–1257, October 1949. doi: 10/dbn2sd.
- [7] F. Hippert, editor. *Neutron and X-ray Spectroscopy*. Springer, Dordrecht, 2006. ISBN 978-1-4020-3336-0 978-1-4020-3337-7.
- [8] Kurt Sköld and David L. Price, editors. *Neutron Scattering*. Number v. 23 in Methods of Experimental Physics. Academic Press, Orlando, 1986. ISBN 978-0-12-475965-7.
- [9] Stephen W. Lovesey and Stephen W. Lovesey. *Polarization Effects and Magnetic Scattering*. Number Stephen W. Lovesey ; Vol. 2 in Theory of Neutron Scattering from Condensed Matter. Clarendon Press, Oxford, reprinted (with corrections) edition, 1987. ISBN 978-0-19-852029-0 978-0-19-852017-7.
- [10] G. L. Squires. *Introduction to the Theory of Thermal Neutron Scattering*. Cambridge University Press, Cambridge, third edition edition, 2012. ISBN 978-1-107-64406-9.
- [11] F. Mezei, C. Pappas, and T. Gutberlet, editors. *Neutron Spin Echo Spectroscopy: Basics, Trends, and Applications*. Number 601 in Lecture Notes in Physics. Springer, Berlin ; New York, 2003. ISBN 978-3-540-44293-6.

Bibliography

- [12] T. Weber, J. Waizner, G. S. Tucker, R. Georgii, M. Kugler, A. Bauer, C. Pfleiderer, M. Garst, and P. Böni. Field dependence of nonreciprocal magnons in chiral MnSi. *Physical Review B*, 97(22):224403, June 2018. doi: 10.1103/PhysRevB.97.224403.
- [13] T. Weber, J. Waizner, G. S. Tucker, L. Beddrich, M. Skoulatos, R. Georgii, A. Bauer, C. Pfleiderer, M. Garst, and P. Böni. Non-reciprocal magnons in non-centrosymmetric MnSi. *AIP Advances*, 8(10):101328, October 2018. doi: 10.1063/1.5041036.
- [14] T. Weber, J. Waizner, P. Steffens, A. Bauer, C. Pfleiderer, M. Garst, and P. Böni. Polarized inelastic neutron scattering of nonreciprocal spin waves in MnSi. *Physical Review B*, 100(6):060404, August 2019. doi: 10.1103/PhysRevB.100.060404.
- [15] Robert Georgii and Tobias Weber. The Helical Magnet MnSi: Skyrmions and Magnons. *Quantum Beam Science*, 3(1):4, March 2019. ISSN 2412-382X. doi: 10.3390/qubs3010004.
- [16] H. T. Diep, editor. *Frustrated Spin Systems*. World Scientific, [Hackensack] New Jersey, 2nd edition edition, 2013. ISBN 978-981-4440-73-8.
- [17] A.F. Andreev and I.A Grishchuk. Spin Nematics. *Journal of Experimental and Theoretical Physics*, 87(2):467, August 1984.
- [18] F. Máca, J. Kudrnovský, V. Drchal, I. Turek, O. Stelmakhovych, P. Beran, A. Llobet, and X. Marti. Defect-induced magnetic structure of CuMnSb. *Physical Review B*, 94(9):094407, September 2016. doi: 10.1103/PhysRevB.94.094407.
- [19] Keizo Endo, Tetuo Ohoyama, and Ren'iti Kimura. Antiferromagnetism of CuMnSb. *Journal of the Physical Society of Japan*, 25(3):907–908, September 1968. ISSN 0031-9015. doi: 10.1143/JPSJ.25.907.
- [20] J. Bœuf, C. Pfleiderer, and A. Faißt. Low-temperature properties of the semi-Heusler compound CuMnSb. *Physical Review B*, 74(2):024428, July 2006. ISSN 1098-0121, 1550-235X. doi: 10.1103/PhysRevB.74.024428.
- [21] R. B. Helmholtz, R. A. de Groot, F. M. Mueller, P. G. van Engen, and K. H. J. Buschow. Magnetic and crystallographic properties of several C1_b type Heusler compounds. *Journal of Magnetism and Magnetic Materials*, 43(3):249–255, August 1984. ISSN 0304-8853. doi: 10.1016/0304-8853(84)90075-1.
- [22] A. Regnat, A. Bauer, A. Senyshyn, M. Meven, K. Hradil, P. Jorba, K. Nemkovski, B. Pedersen, R. Georgii, S. Gottlieb-Schönmeier, and C. Pfleiderer. Canted antiferromagnetism in phase-pure CuMnSb. *Physical Review Materials*, 2(5):054413, May 2018. ISSN 2475-9953. doi: 10.1103/PhysRevMaterials.2.054413.
- [23] Gen Shirane, Stephen M Shapiro, and John M Tranquada. Neutron Scattering with a Triple-Axis Spectrometer: Basic Techniques. page 285.

- [24] Léon Van Hove. Correlations in Space and Time and Born Approximation Scattering in Systems of Interacting Particles. *Physical Review*, 95(1):249–262, July 1954. ISSN 0031-899X. doi: 10.1103/PhysRev.95.249.
- [25] NIST Fundamental Constants Bibliographic Search. URL <https://physics.nist.gov/cuu/Constants/Citations/Search.html>.
- [26] Tapan Chatterji, editor. *Neutron Scattering from Magnetic Materials*. Elsevier, Amsterdam ; Boston, 1st ed edition, 2006. ISBN 978-0-444-51050-1.
- [27] L. D. Landau, E. M. Lifshits, L. P. Pitaevskiĭ, L. D. Landau, and L. D. Landau. *Statistical physics*. Number v. 5, 9 in Pergamon international library of science, technology, engineering, and social studies. Pergamon Press, Oxford ; New York, 1980. ISBN 978-0-08-023039-9.
- [28] Robert M. White. *Quantum Theory of Magnetism: Magnetic Properties of Materials*. Number 32 in Springer Series in Solid-State Sciences. Springer, Berlin, 3rd, completely rev. ed edition, 2007. ISBN 978-3-540-69025-2.
- [29] P. Böni, B. Roessli, D. Görlitz, and J. Kötzler. Damping of spin waves and singularity of the longitudinal modes in the dipolar critical regime of the Heisenberg ferromagnet EuS. *Physical Review B*, 65(14):144434, April 2002. ISSN 0163-1829, 1095-3795. doi: 10.1103/PhysRevB.65.144434.
- [30] Tasso Springer. *Quasielastic Neutron Scattering for the Investigation of Diffuse Motions in Solids and Liquids*. Number 64 in Springer Tracts in Modern Physics. Springer, Berlin, 1992. ISBN 978-3-540-05808-3 978-0-387-05808-5.
- [31] M. Bée. *Quasielastic Neutron Scattering: Principles and Applications in Solid State Chemistry, Biology, and Materials Science*. Adam Hilger, Bristol, England ; Philadelphia, 1988. ISBN 978-0-85274-371-3.
- [32] R. Georgii, T. Weber, G. Brandl, M. Skoulatos, M. Janoschek, S. Mühlbauer, C. Pfeleiderer, and P. Böni. The multi-purpose three-axis spectrometer (TAS) MIRA at FRM II. *Nuclear Instruments and Methods in Physics Research Section A: Accelerators, Spectrometers, Detectors and Associated Equipment*, 881:60–64, February 2018. ISSN 01689002. doi: 10.1016/j.nima.2017.09.063.
- [33] Joachim Wuttke, Alfred Budwig, Matthias Drochner, Hans Kämmerling, Franz-Joseph Kayser, Harald Kleines, Vladimir Ossovyi, Luis Carlos Pardo, Michael Prager, Dieter Richter, Gerald J. Schneider, Harald Schneider, and Simon Staringer. SPHERES, Jülich’s high-flux neutron backscattering spectrometer at FRM II. *Review of Scientific Instruments*, 83(7):075109, July 2012. ISSN 0034-6748, 1089-7623. doi: 10.1063/1.4732806.
- [34] F. Mezei. Neutron spin echo: A new concept in polarized thermal neutron techniques. *Zeitschrift für Physik A Hadrons and nuclei*, 255(2):146–160, April 1972. ISSN 0939-7922. doi: 10.1007/BF01394523.

Bibliography

- [35] R. Golub and R. Gähler. A neutron resonance spin echo spectrometer for quasi-elastic and inelastic scattering. *Physics Letters A*, 123(1):43–48, July 1987. ISSN 03759601. doi: 10.1016/0375-9601(87)90760-2.
- [36] C. Pappas, E. Lelièvre-Berna, P. Bentley, E. Bourgeat-Lami, E. Moskvina, M. Thomas, S. Grigoriev, and V. Dyadkin. Polarimetric neutron spin echo: Feasibility and first results. *Nuclear Instruments and Methods in Physics Research Section A: Accelerators, Spectrometers, Detectors and Associated Equipment*, 592(3):420–427, July 2008. ISSN 01689002. doi: 10.1016/j.nima.2008.04.078.
- [37] Christian Franz and Thorsten Schröder. RESEDA: Resonance spin echo spectrometer. *Journal of large-scale research facilities JLSRF*, 1:A14, August 2015. ISSN 2364-091X. doi: 10.17815/jlsrf-1-37.
- [38] Robert Georgii and Klaus Seemann. MIRA: Dual wavelength band instrument. *Journal of large-scale research facilities JLSRF*, 1:A3, August 2015. ISSN 2364-091X. doi: 10.17815/jlsrf-1-21.
- [39] Tobias Weber. *Dynamics at the Orbital Ordering Phase Transition in MgV_2O_4 and at the Ferromagnetic Phase Transition in $MnSi$* . PhD thesis, Technische Universität München, München, 2017. URL <http://mediatum.ub.tum.de?id=1339645>.
- [40] Nikolas Arend. *New Aspects of the MIEZE Technique and Verification of the Multi-level MIEZE Principle*. PhD thesis, Technical University Munich, Munich.
- [41] R. Gähler, R. Golub, K. Habicht, T. Keller, and J. Felber. Space-time description of neutron spin echo spectrometry. *Physica B: Condensed Matter*, 229(1):1–17, December 1996. ISSN 09214526. doi: 10.1016/S0921-4526(96)00509-1.
- [42] R. Golub, R. Gähler, and T. Keller. A plane wave approach to particle beam magnetic resonance. *American Journal of Physics*, 62(9):779–788, September 1994. ISSN 0002-9505, 1943-2909. doi: 10.1119/1.17459.
- [43] Thomas Keller, Robert Golub, and Roland Gähler. Neutron Spin Echo - A Technique for High-Resolution Neutron Scattering. In *Scattering*, pages 1264–1286. Elsevier, 2002. ISBN 978-0-12-613760-6. doi: 10.1016/B978-012613760-6/50068-1.
- [44] Jonas Kindervater. Fluctuation-induced magnetic phase transitions in Fe and MnSi studied by neutron scattering. page 163.
- [45] Ch. Schwink and O. Schörfpf. Solution of the Pauli-equation for neutrons in varying magnetic fields and its application to reflection and transmission at helical magnetic structures. *Zeitschrift für Physik B Condensed Matter and Quanta*, 21(3):305–311, September 1975. ISSN 0340-224X, 1434-6036. doi: 10.1007/BF01313312.
- [46] G. Brandl, R. Georgii, W. Häußler, S. Mühlbauer, and P. Böni. Large Scales - Long Times: Adding High Energy Resolution to SANS. *Nuclear Instruments and Methods in Physics Research Section A: Accelerators, Spectrometers, Detectors*

- and Associated Equipment*, 654(1):394–398, October 2011. ISSN 01689002. doi: 10.1016/j.nima.2011.07.003.
- [47] N. Martin. On the resolution of a MIEZE spectrometer. *Nuclear Instruments and Methods in Physics Research Section A: Accelerators, Spectrometers, Detectors and Associated Equipment*, 882:11–16, February 2018. ISSN 01689002. doi: 10.1016/j.nima.2017.11.021.
- [48] J. K. Jochum, A. Hecht, O. Soltwedel, C. Fuchs, J. Frank, E. Faulhaber, J. C. Leiner, C. Pfeiderer, and C. Franz. Oscillatory magnetic fields for neutron resonance spin-echo spectroscopy. *Measurement Science and Technology*, 32(4):045902, February 2021. ISSN 0957-0233. doi: 10/gmtv73.
- [49] Maro Köppe, Peter Hank, Joachim Wuttke, Winfried Petry, Roland Gähler, and Rémi Kahn. Performance and future of a neutron resonance spinecho spectrometer. *Journal of Neutron Research*, 4(1):261–273, December 1996. ISSN 1023-8166. doi: 10.1080/10238169608200092.
- [50] Jeremy C. Cook. Concepts and Engineering Aspects of a Neutron Resonance Spin-Echo Spectrometer for the National Institute of Standards and Technology Center for Neutron Research. *Journal of Research of the National Institute of Standards and Technology*, 119:55, April 2014. ISSN 2165-7254. doi: 10/gn937s.
- [51] T. Weber, G. Brandl, R. Georgii, W. Häußler, S. Weichselbaumer, and P. Böni. Monte-Carlo simulations for the optimisation of a TOF-MIEZE instrument. *Nuclear Instruments and Methods in Physics Research Section A: Accelerators, Spectrometers, Detectors and Associated Equipment*, 713:71–75, June 2013. ISSN 0168-9002. doi: 10.1016/j.nima.2013.03.010.
- [52] J. K. Jochum, A. Wendl, T. Keller, and C. Franz. Neutron MIEZE spectroscopy with focal length tuning. *Measurement Science and Technology*, 31(3):035902, December 2019. ISSN 0957-0233. doi: 10/gmxd83.
- [53] S Boudin, A Guesdon, A Leclaire, and M.-M Borel. Review on vanadium phosphates with mono and divalent metallic cations: Syntheses, structural relationships and classification, properties. *International Journal of Inorganic Materials*, 2(6):561–579, December 2000. ISSN 14666049. doi: 10.1016/S1466-6049(00)00074-X.
- [54] Thomas A. Chirayil, Peter Y. Zavalij, and M. Stanley Whittingham. A New Vanadium Dioxide Cathode. *Journal of The Electrochemical Society*, 143(9):L193, September 1996. ISSN 1945-7111. doi: 10.1149/1.1837083.
- [55] F. Abraham, J. C. Boivin, G. Mairesse, and G. Nowogrocki. The bimevox series: A new family of high performances oxide ion conductors. *Solid State Ionics*, 40–41: 934–937, August 1990. ISSN 0167-2738. doi: 10.1016/0167-2738(90)90157-M.
- [56] Yutaka Ueda. Vanadate Family as Spin-Gap Systems. *Chemistry of Materials*, 10(10):2653–2664, October 1998. ISSN 0897-4756. doi: 10.1021/cm980215w.

Bibliography

- [57] P. W. Anderson, G. Baskaran, Z. Zou, and T. Hsu. Resonating – valence-bond theory of phase transitions and superconductivity in La_2CuO_4 -based compounds. *Physical Review Letters*, 58(26):2790–2793, June 1987. ISSN 0031-9007. doi: 10/bf3hq4.
- [58] P. W. Anderson. The Resonating Valence Bond State in La_2CuO_4 and Superconductivity. *Science*, 235(4793):1196–1198, March 1987. ISSN 0036-8075, 1095-9203. doi: 10/bt426c.
- [59] M. Skoulatos, F. Rucker, G. J. Nilsen, A. Bertin, E. Pomjakushina, J. Ollivier, A. Schneidewind, R. Georgii, O. Zaharko, L. Keller, Ch Rüegg, C. Pfleiderer, B. Schmidt, N. Shannon, A. Kriele, A. Senyshyn, and A. Smerald. Putative spin-nematic phase in $\text{BaCdVO}(\text{PO}_4)_2$. March 2019. doi: 10.1103/PhysRevB.100.014405.
- [60] Stephen Blundell. *Magnetism in Condensed Matter*. Oxford Master Series in Condensed Matter Physics. Oxford University Press, Oxford ; New York, 2001. ISBN 978-0-19-850592-1.
- [61] P Millet and C Satto. Synthesis and structures of the layered vanadyl(IV) silico-germanates $\text{Li}_2\text{VO}(\text{Si}_{1-x}\text{Ge}_x)\text{O}_4$ ($x = 0, 0.5, 1$). *Materials Research Bulletin*, 33(9): 1339–1345, September 1998. ISSN 0025-5408. doi: 10.1016/S0025-5408(98)00122-6.
- [62] R. Melzi, S. Aldrovandi, F. Tedoldi, P. Carretta, P. Millet, and F. Mila. Magnetic and thermodynamic properties of $\text{Li}_2\text{VOSiO}_4$ A two-dimensional $S=1/2$ frustrated antiferromagnet on a square lattice. *Physical Review B*, 64(2):024409, June 2001. doi: 10.1103/PhysRevB.64.024409.
- [63] R. Melzi, P. Carretta, A. Lascialfari, M. Mambrini, M. Troyer, P. Millet, and F. Mila. $\text{Li}_2\text{VO}(\text{Si}, \text{Ge})\text{O}_4$, a Prototype of a Two-Dimensional Frustrated Quantum Heisenberg Antiferromagnet. *Physical Review Letters*, 85(6):1318–1321, August 2000. ISSN 0031-9007, 1079-7114. doi: 10/c579gq.
- [64] Serena C. Tarantino, Michele Zema, Tiziana Boffa Ballaran, and Paolo Ghigna. Room-temperature equation of state of $\text{Li}_2\text{VOSiO}_4$ up to 8.5 GPa. *Physics and Chemistry of Minerals*, 35(2):71–76, March 2008. ISSN 0342-1791, 1432-2021. doi: 10.1007/s00269-007-0199-x.
- [65] P. Carretta, N. Papinutto, C. B. Azzoni, M. C. Mozzati, E. Pavarini, S. Gonthier, and P. Millet. Frustration-driven structural distortion in VOMoO_4 . *Physical Review B*, 66(9):094420, September 2002. doi: 10.1103/PhysRevB.66.094420.
- [66] P. Carretta, R. Melzi, N. Papinutto, and P. Millet. Very-Low-Frequency Excitations in Frustrated Two-Dimensional $S=1/2$ Heisenberg Antiferromagnets. *Physical Review Letters*, 88(4):047601, January 2002. doi: 10.1103/PhysRevLett.88.047601.
- [67] H. Rosner, R. R. P. Singh, W. H. Zheng, J. Oitmaa, and W. E. Pickett. High-temperature expansions for the J_1 - J_2 Heisenberg models: Applications to ab initio

- calculated models for $\text{Li}_2\text{VO}_2\text{SiO}_4$ and $\text{Li}_2\text{VO}_2\text{GeO}_4$. *Physical Review B*, 67(1):014416, January 2003. doi: 10.1103/PhysRevB.67.014416.
- [68] H. Rosner, R. R. P. Singh, W. H. Zheng, J. Oitmaa, S.-L. Drechsler, and W. E. Pickett. Realization of a Large J_2 Quasi-2D Spin-Half Heisenberg System: $\text{Li}_2\text{VO}_2\text{SiO}_4$. *Physical Review Letters*, 88(18):186405, April 2002. doi: 10.1103/PhysRevLett.88.186405.
- [69] A. Bombardi, J. Rodriguez-Carvajal, S. Di Matteo, F. de Bergevin, L. Paolasini, P. Carretta, P. Millet, and R. Caciuffo. Direct Determination of the Magnetic Ground State in the Square Lattice $S=1/2$ Antiferromagnet $\text{Li}_2\text{VO}_2\text{SiO}_4$. *Physical Review Letters*, 93(2):027202, July 2004. doi: 10.1103/PhysRevLett.93.027202.
- [70] A. Bombardi, L. C. Chapon, I. Margiolaki, C. Mazzoli, S. Gonthier, F. Duc, and P. G. Radaelli. Magnetic order and lattice anomalies in the J_1 - J_2 model system VOMoO_4 . *Physical Review B*, 71(22):220406, June 2005. doi: 10.1103/PhysRevB.71.220406.
- [71] Alexander A. Tsirlin, Alexei A. Belik, Roman V. Shpanchenko, Evgeny V. Antipov, Eiji Takayama-Muromachi, and Helge Rosner. Frustrated spin-1/2 square lattice in the layered perovskite PbVO_3 . *Physical Review B*, 77(9):092402, March 2008. doi: 10.1103/PhysRevB.77.092402.
- [72] Kengo Oka, Ikuya Yamada, Masaki Azuma, Soshi Takeshita, Kohki H. Satoh, Akihiro Koda, Ryosuke Kadono, Mikio Takano, and Yuichi Shimakawa. Magnetic Ground-State of Perovskite PbVO_3 with Large Tetragonal Distortion. *Inorganic Chemistry*, 47(16):7355–7359, August 2008. ISSN 0020-1669. doi: 10.1021/ic800649a.
- [73] E. E. Kaul, H. Rosner, N. Shannon, R. V. Shpanchenko, and C. Geibel. Evidence for a frustrated square lattice with ferromagnetic nearest-neighbor interaction in the new compound $\text{Pb}_2\text{VO}(\text{PO}_4)_2$. *Journal of Magnetism and Magnetic Materials*, 272–276:922–923, May 2004. ISSN 0304-8853. doi: 10/d9jm55.
- [74] M. Skoulatos, J. P. Goff, N. Shannon, E. E. Kaul, C. Geibel, A. P. Murani, M. Enderle, and A. R. Wildes. Spin correlations in the frustrated square lattice $\text{Pb}_2\text{VO}(\text{PO}_4)_2$. *Journal of Magnetism and Magnetic Materials*, 310(2, Part 2): 1257–1259, March 2007. ISSN 0304-8853. doi: 10/c4v84m.
- [75] M. Skoulatos, J. P. Goff, C. Geibel, E. E. Kaul, R. Nath, N. Shannon, B. Schmidt, A. P. Murani, P. P. Deen, M. Enderle, and A. R. Wildes. Spin correlations and exchange in square-lattice frustrated ferromagnets. *EPL (Europhysics Letters)*, 88(5):57005, December 2009. ISSN 0295-5075, 1286-4854. doi: 10.1209/0295-5075/88/57005.
- [76] R. Nath, A. A. Tsirlin, H. Rosner, and C. Geibel. Magnetic properties of $\text{BaCdVO}(\text{PO}_4)_2$: A strongly frustrated spin-1/2 square lattice close to the quantum critical regime. *Physical Review B*, 78(6):064422, August 2008. ISSN 1098-0121, 1550-235X. doi: 10.1103/PhysRevB.78.064422.

Bibliography

- [77] Markos Skoulatos. *Spin Correlations and Orbital Physics in Vanadates*. PhD thesis, March 2008.
- [78] N. Shannon, B. Schmidt, K. Penc, and P. Thalmeier. Finite temperature properties and frustrated ferromagnetism in a square lattice Heisenberg model. *The European Physical Journal B*, 38(4):599–616, April 2004. ISSN 1434-6028, 1434-6036. doi: 10.1140/epjb/e2004-00156-3.
- [79] N. D. Mermin and H. Wagner. Absence of Ferromagnetism or Antiferromagnetism in One- or Two-Dimensional Isotropic Heisenberg Models. *Physical Review Letters*, 17(22):1133–1136, November 1966. doi: 10/c7bj43.
- [80] L. Siurakshina, D. Ihle, and R. Hayn. Magnetic order and finite-temperature properties of the two-dimensional frustrated Heisenberg model. *Physical Review B*, 64(10):104406, August 2001. doi: 10/bmd43r.
- [81] J. Villain. A magnetic analogue of stereoisomerism : Application to helimagnetism in two dimensions. *Journal de Physique*, 38(4):385–391, April 1977. ISSN 0302-0738, 2777-3396. doi: 10/cbhpf.
- [82] J. Villain, R. Bidaux, J.-P. Carton, and R. Conte. Order as an effect of disorder. *Journal de Physique*, 41(11):1263–1272, 1980. ISSN 0302-0738. doi: 10.1051/jphys:0198000410110126300.
- [83] Christopher L. Henley. Ordering due to disorder in a frustrated vector antiferromagnet. *Physical Review Letters*, 62(17):2056–2059, April 1989. doi: 10/cx547m.
- [84] E.F. Shender. Journal of Experimental and Theoretical Physics. *Journal of Experimental and Theoretical Physics*, January 1982. URL <http://www.jetp.ras.ru/cgi-bin/e/index/e/56/1/p178?a=list>.
- [85] Th. Brückel, C. Paulsen, K. Hinrichs, and W. Prandl. Ordering due to disorder in an antiferromagnet with continuously degenerate Néel ground state: A combined neutron diffraction and magnetization study of $(\text{Fe}_x\text{Ga}_{1-x})_2\text{Ca}_3\text{Ge}_3\text{O}_{12}$. *Zeitschrift für Physik B Condensed Matter*, 97(3):391–401, September 1995. ISSN 1431-584X. doi: 10/fp956x.
- [86] Th. Brückel, B. Dorner, A. G. Gukasov, V. P. Plakhty, W. Prandl, E. F. Shender, and O. P. Smirnow. Dynamical interaction of antiferromagnetic subsystems: A neutron scattering study of the spinwave spectrum of the garnet $\text{Fe}_2\text{Ca}_3(\text{GeO}_4)_3$. *Zeitschrift für Physik B Condensed Matter*, 72(4):477–485, December 1988. ISSN 1431-584X. doi: 10/cs4cm5.
- [87] Th. Brückel, B. Dorner, A. G. Gukasov, V. P. Plakhty, W. Prandl, E. F. Shender, and O. P. Smirnov. Dynamical sublattice interaction in the antiferromagnetic garnet $\text{Fe}_2\text{Ca}_3(\text{GeO}_4)_3$ as studied by neutron scattering. *Physica B: Condensed Matter*, 156–157:308–310, January 1989. ISSN 0921-4526. doi: 10/b2m9zv.

- [88] P. Chandra and B. Douçot. Possible spin-liquid state at large S for the frustrated square Heisenberg lattice. *Physical Review B*, 38(13):9335–9338, November 1988. doi: 10/ccd2h9.
- [89] P. W. Anderson. An Approximate Quantum Theory of the Antiferromagnetic Ground State. *Physical Review*, 86(5):694–701, June 1952. doi: 10/fh8j3f.
- [90] Ryogo Kubo. The Spin-Wave Theory of Antiferromagnetics. *Physical Review*, 87(4):568–580, August 1952. doi: 10/bmj4p9.
- [91] Takehiko Oguchi. Theory of Spin-Wave Interactions in Ferro- and Antiferromagnetism. *Physical Review*, 117(1):117–123, January 1960. doi: 10/d6qq7p.
- [92] Matthieu Mambrini, Andreas Läuchli, Didier Poilblanc, and Frédéric Mila. Plaquette valence-bond crystal in the frustrated Heisenberg quantum antiferromagnet on the square lattice. *Physical Review B*, 74(14):144422, October 2006. doi: 10/bvvnbj.
- [93] P. Sindzingre. Spin-1/2 frustrated antiferromagnet on a spatially anisotropic square lattice: Contribution of exact diagonalizations. *Physical Review B*, 69(9):094418, March 2004. doi: 10/drgv5x.
- [94] N. Read and Subir Sachdev. Large- N expansion for frustrated quantum antiferromagnets. *Physical Review Letters*, 66(13):1773–1776, April 1991. doi: 10/drntvz.
- [95] N. Read and Subir Sachdev. Valence-bond and spin-Peierls ground states of low-dimensional quantum antiferromagnets. *Physical Review Letters*, 62(14):1694–1697, April 1989. doi: 10/ccr8c4.
- [96] Valeri N. Kotov, J. Oitmaa, Oleg P. Sushkov, and Zheng Weihong. Low-energy singlet and triplet excitations in the spin-liquid phase of the two-dimensional J_1 - J_2 model. *Physical Review B*, 60(21):14613–14616, December 1999. ISSN 0163-1829, 1095-3795. doi: 10/bvn7qr.
- [97] Martin P. Gelfand, Rajiv R. P. Singh, and David A. Huse. Zero-temperature ordering in two-dimensional frustrated quantum Heisenberg antiferromagnets. *Physical Review B*, 40(16):10801–10809, December 1989. doi: 10/cvszzj.
- [98] Martin P. Gelfand. Series investigations of magnetically disordered ground states in two-dimensional frustrated quantum antiferromagnets. *Physical Review B*, 42(13):8206–8213, November 1990. doi: 10/dpr3g5.
- [99] Rajiv R. P. Singh, Zheng Weihong, C. J. Hamer, and J. Oitmaa. Dimer order with striped correlations in the J_1 - J_2 Heisenberg model. *Physical Review B*, 60(10):7278–7283, September 1999. doi: 10/c6r57k.
- [100] M. S. L. du Croo de Jongh, J. M. J. van Leeuwen, and W. van Saarloos. Incorporation of density-matrix wave functions in Monte Carlo simulations: Application to the frustrated Heisenberg model. *Physical Review B*, 62(22):14844–14854, December 2000. doi: 10/ddk7vb.

Bibliography

- [101] Luca Capriotti and Sandro Sorella. Spontaneous Plaquette Dimerization in the J_1 - J_2 Heisenberg Model. *Physical Review Letters*, 84(14):3173–3176, April 2000. doi: 10/dqrzqm.
- [102] O. P. Sushkov, J. Oitmaa, and Zheng Weihong. Quantum phase transitions in the two-dimensional J_1 - J_2 model. *Physical Review B*, 63(10):104420, February 2001. doi: 10/dn2g9x.
- [103] Enrique Eduardo Kaul. *Experimental Investigation of New Low-Dimensional Spin Systems in Vanadium Oxides*. PhD thesis, October 2005.
- [104] A. A. Ovchinnikov, V. Ya. Krivnov, and D. V. Dmitriev. The ferromagnet-antiferromagnet transition in frustrated quantum spin models. *Synthetic Metals*, 85(1):1757–1760, March 1997. ISSN 0379-6779. doi: 10/fb85z5.
- [105] D. V. Dmitriev, V. Ya. Krivnov, and A. A. Ovchinnikov. Two-dimensional frustrated Heisenberg model: Variational study. *Physical Review B*, 55(6):3620–3626, February 1997. doi: 10/fxb8hn.
- [106] Nic Shannon, Tsutomu Momoi, and Philippe Sindzingre. Nematic Order in Square Lattice Frustrated Ferromagnets. *Physical Review Letters*, 96(2):027213, January 2006. doi: 10.1103/PhysRevLett.96.027213.
- [107] Hajime Ishikawa, Nanako Nakamura, Makoto Yoshida, Masashi Takigawa, Peter Babkevich, Navid Qureshi, Henrik M. Rønnow, Takeshi Yajima, and Zenji Hiroi. J_1 - J_2 square-lattice Heisenberg antiferromagnets with 4d1 spins: A MoOPO_4Cl ($A = \text{K, Rb}$). *Physical Review B*, 95(6):064408, February 2017. ISSN 2469-9950, 2469-9969. doi: 10/gkp562.
- [108] Andrew Smerald. Presentation on $\text{BaCdVO}(\text{PO}_4)_2$ spin nematic.
- [109] Andrew Smerald, Hiroaki T. Ueda, and Nic Shannon. Theory of inelastic neutron scattering in a field-induced spin-nematic state. *Physical Review B*, 91(17):174402, May 2015. ISSN 1098-0121, 1550-235X. doi: 10/gktd4s.
- [110] Hiroaki T. Ueda. Magnetic Phase Diagram Slightly below the Saturation Field in the Stacked J_1 - J_2 Model in the Square Lattice with the JC Interlayer Coupling. *Journal of the Physical Society of Japan*, 84(2):023601, February 2015. ISSN 0031-9015. doi: 10/gkn4qt.
- [111] Philippe Sindzingre, L. Seabra, Nic Shannon, and Tsutomu Momoi. Phase diagram of the spin-1/2 J_1 - J_2 - J_3 Heisenberg model on the square lattice with ferromagnetic J_1 . *Journal of Physics: Conference Series*, 145:012048, January 2009. ISSN 1742-6596. doi: 10/bc9669.
- [112] Andrey V. Chubukov. Chiral, nematic, and dimer states in quantum spin chains. *Physical Review B*, 44(9):4693–4696, September 1991. doi: 10/ckssb5.

- [113] H. T. Diep, editor. *Frustrated Spin Systems*. World Scientific, Hackensack, NJ, 2004. ISBN 978-981-256-091-9.
- [114] Hiroaki T. Ueda and Keisuke Totsuka. Ground-state phase diagram and magnetic properties of a tetramerized spin-1/2 J_1 - J_2 model: BEC of bound magnons and absence of the transverse magnetization. *Physical Review B*, 76(21):214428, December 2007. ISSN 1098-0121, 1550-235X. doi: 10/dr3rns.
- [115] N S Kini, E E Kaul, and C Geibel. $Zn_2VO(PO_4)_2$: An $S = 1/2$ Heisenberg antiferromagnetic square lattice system. *Journal of Physics: Condensed Matter*, 18(4):1303–1311, February 2006. ISSN 0953-8984, 1361-648X. doi: 10/fqbwmc.
- [116] Burkhard Schmidt, Nic Shannon, and M Zhitomirsky. High-field properties of frustrated 2D square lattice magnets. page 32.
- [117] K. Yu. Povarov, V. K. Bhartiya, Z. Yan, and A. Zheludev. Thermodynamics of a frustrated quantum magnet on a square lattice. *Physical Review B*, 99(2):024413, January 2019. doi: 10.1103/PhysRevB.99.024413.
- [118] V. K. Bhartiya, K. Yu. Povarov, D. Blosser, S. Bettler, Z. Yan, S. Gvasaliya, S. Raymond, E. Ressouche, K. Beauvois, J. Xu, F. Yokaichiya, and A. Zheludev. Presaturation phase with no dipolar order in a quantum ferro-antiferromagnet. *Physical Review Research*, 1(3):033078, November 2019. ISSN 2643-1564. doi: 10.1103/PhysRevResearch.1.033078.
- [119] V. K. Bhartiya, S. Hayashida, K. Yu. Povarov, Z. Yan, Y. Qiu, S. Raymond, and A. Zheludev. Inelastic neutron scattering determination of the spin Hamiltonian for $BaCdVO(PO_4)_2$. *Physical Review B*, 103(14):144402, April 2021. ISSN 2469-9950, 2469-9969. doi: 10.1103/PhysRevB.103.144402.
- [120] Andrew Smerald. Magnon binding in $BaCdVO(PO_4)_2$. *arXiv:2003.12747 [cond-mat]*, March 2020. URL <http://arxiv.org/abs/2003.12747>.
- [121] S. Toth and B. Lake. Linear spin wave theory for single-Q incommensurate magnetic structures. *Journal of Physics: Condensed Matter*, 27(16):166002, March 2015. ISSN 0953-8984. doi: 10/gkpg2q.
- [122] Tanja Graf, Claudia Felser, and Stuart S.P. Parkin. Simple rules for the understanding of Heusler compounds. *Progress in Solid State Chemistry*, 39(1):1–50, May 2011. ISSN 00796786. doi: 10.1016/j.progsolidstchem.2011.02.001.
- [123] Claudia Felser, Lukas Wollmann, Stanislav Chadov, Gerhard H. Fecher, and Stuart S. P. Parkin. Basics and prospective of magnetic Heusler compounds. *APL Materials*, 3(4):041518, April 2015. doi: 10/gnfsrq.
- [124] S. Sakurada and N. Shutoh. Effect of Ti substitution on the thermoelectric properties of (Zr,Hf)NiSn half-Heusler compounds. *Applied Physics Letters*, 86(8):082105, February 2005. ISSN 0003-6951. doi: 10/bhn768.

Bibliography

- [125] R. Y. Umetsu, K. Kobayashi, R. Kainuma, A. Fujita, K. Fukamichi, K. Ishida, and A. Sakuma. Magnetic properties and band structures of half-metal-type Co₂CrGa Heusler alloy. *Applied Physics Letters*, 85(11):2011–2013, September 2004. ISSN 0003-6951. doi: 10/btbcgf.
- [126] Thorsten Krenke, Eyüp Duman, Mehmet Acet, Eberhard F. Wassermann, Xavier Moya, Lluís Mañosa, and Antoni Planes. Inverse magnetocaloric effect in ferromagnetic Ni-Mn-Sn alloys. *Nature Materials*, 4(6):450–454, June 2005. ISSN 1476-1122. doi: 10/cpstbh.
- [127] R. Kainuma, Y. Imano, W. Ito, Y. Sutou, H. Morito, S. Okamoto, O. Kitakami, K. Oikawa, A. Fujita, T. Kanomata, and K. Ishida. Magnetic-field-induced shape recovery by reverse phase transformation. *Nature*, 439(7079):957–960, February 2006. ISSN 1476-4687. doi: 10/d84r23.
- [128] P. G. van Engen, K. H. J. Buschow, R. Jongebreur, and M. Erman. PtMnSb, a material with very high magneto-optical Kerr effect. *Applied Physics Letters*, 42(2):202–204, January 1983. ISSN 0003-6951. doi: 10/cvx9j7.
- [129] C. Pfeleiderer. Are Mn₃Si and CuMnSb antiferromagnetic half-metals? *Physica B: Condensed Matter*, 329–333(Part 2):1085–1086, May 2003. ISSN 0921-4526. doi: 10.1016/S0921-4526(02)02345-1.
- [130] T. Jeong, Ruben Weht, and W. E. Pickett. Semimetallic antiferromagnetism in the half-Heusler compound CuMnSb. *Physical Review B*, 71(18):184103, May 2005. doi: 10.1103/PhysRevB.71.184103.
- [131] L. Castelliz. Über eine Mischkristallreihe zwischen zwei ternären Vertretern des C1-Typs. *Monatshefte für Chemie und verwandte Teile anderer Wissenschaften*, 83(6):1314–1317, November 1952. ISSN 0343-7329, 1434-4475. doi: 10.1007/BF00913833.
- [132] H. Nowotny and B. Glatzl. Neue Vertreter ternärer Verbindungen mit C1-Struktur. *Monatshefte für Chemie und verwandte Teile anderer Wissenschaften*, 83(1):237–241, January 1952. ISSN 0343-7329, 1434-4475. doi: 10.1007/BF00897823.
- [133] R. H. Forster, G. B. Johnston, and D. A. Wheeler. Studies on the Heusler alloys—III. The antiferromagnetic phase in the Cu–Mn–Sb system. *Journal of Physics and Chemistry of Solids*, 29(5):855–861, May 1968. ISSN 0022-3697. doi: 10.1016/0022-3697(68)90147-9.
- [134] W. H. Schreiner and D. E. Brandão. Electrical resistivity of the C1_b alloy CuMnSb. *Solid State Communications*, 43(6):463–465, August 1982. ISSN 0038-1098. doi: 10.1016/0038-1098(82)91169-3.
- [135] Mathias Doerr, Julien Bœuf, Christian Pfeleiderer, Martin Rotter, Nadejda Kozlova, Dieter Eckert, Peter Kersch, Karl-Hartmut Müller, and Michael Loewenhaupt. Search for half-metallic antiferromagnetism using pulsed magnetic fields:

- Experimental investigation of Mn_3Si , CuMnSb and PdMnTe . *Physica B: Condensed Matter*, 346–347(Supplement C):137–141, April 2004. ISSN 0921-4526. doi: 10.1016/j.physb.2004.01.036.
- [136] J. Kuneš and W. E. Pickett. Kondo and anti-Kondo coupling to local moments in $\{\text{EuB}\}_6$. *Physical Review B*, 69(16):165111, April 2004. doi: 10.1103/PhysRevB.69.165111.
- [137] A P Ramirez. Strongly Geometrically Frustrated Magnets. *Annual Review of Materials Science*, 24(1):453–480, August 1994. ISSN 0084-6600. doi: 10/crd9tg.
- [138] Matt Newville, Renee Otten, Andrew Nelson, Antonino Ingargiola, Till Stensitzki, Dan Allan, Austin Fox, Faustin Carter, Michał, Dima Pustakhod, Lneuhau, Sebastian Weigand, Ray Osborn, Glenn, Christoph Deil, Mark, Allan L. R. Hansen, Gustavo Pasquevich, Leon Foks, Nicholas Zobrist, Oliver Frost, Alexandre Beelen, Stuermer, Kwertyops, Anthony Polloreno, Shane Caldwell, Anthony Almarza, Arun Persaud, Ben Gamari, and Benjamin F. Maier. Lmfit/lmfit-py 1.0.2. Zenodo, February 2021.
- [139] M. T. Hutchings and E. J. Samuelsen. Measurement of Spin-Wave Dispersion in NiO by Inelastic Neutron Scattering and Its Relation to Magnetic Properties. *Physical Review B*, 6(9):3447–3461, November 1972. ISSN 0556-2805. doi: 10.1103/PhysRevB.6.3447.
- [140] G. Pepy. Spin waves in MnO; from 4°K to temperatures close to TN. *Journal of Physics and Chemistry of Solids*, 35(3):433–444, January 1974. ISSN 00223697. doi: 10.1016/S0022-3697(74)80037-5.
- [141] Andrew L. Goodwin, Martin T. Dove, Matthew G. Tucker, and David A. Keen. MnO spin-wave dispersion curves from neutron powder diffraction. *Physical Review B*, 75(7):075423, February 2007. ISSN 1098-0121, 1550-235X. doi: 10.1103/PhysRevB.75.075423.
- [142] G. Kugel, B. Hennion, and C. Carabator. Dynamic properties of Wustite (Fe_{1-x}O). *Journal of Magnetism and Magnetic Materials*, 7(1-4):18–22, January 1978. ISSN 03048853. doi: 10.1016/0304-8853(78)90140-3.
- [143] M. E. Lines and E. D. Jones. Antiferromagnetism in the Face-Centered Cubic Lattice. II. Magnetic Properties of MnO. *Physical Review*, 139(4A):A1313–A1327, August 1965. ISSN 0031-899X. doi: 10.1103/PhysRev.139.A1313.
- [144] T. Holstein and H. Primakoff. Field Dependence of the Intrinsic Domain Magnetization of a Ferromagnet. *Physical Review*, 58(12):1098–1113, December 1940. doi: 10.1103/PhysRev.58.1098.
- [145] Batronix GmbH & Co KG. R&S® RTE1104. URL <https://www.batronix.com/versand/oszilloskope/Rohde-Schwarz-RTE1104.html>.

Bibliography

- [146] Niederspannungsnetzgeräte mit höchster Präzision. URL <https://www.heinzinger.de/netzgeraete/niederspannung/linear-geregelte-netzgeraete-ptn/>.

A Appendix: Electronic devices

A simplified circuit diagram for the MIEZE-setup is shown in figure A.1 as it was connected in the presented experiment. The DC current driven B_0 coils are omitted as their circuit plan is simple and well described in section 3.7.2. The RF-coils need a stable oscillating current with a specific frequency depending on the configured MIEZE time. This is realised by creating a resonant LC-circuit inside these coils. In order to realise a LC-circuit one needs are frequency generator, an amplifier and a capacitor with variable capacity.

Wave function generator The Keysight 33500B Series Waveform and the Agilent arbitrary waveform generators 33220A, depicted in Fig. 2.24 (top) are able to produce sinusoidal signals from 1 μ Hz to 20 MHz.

The Keysight generator acts as a trigger, which phase-locks the Agilent generators. Otherwise the detector's time channel would drift over time and therefore averaging and flattening the MIEZE signal. Further it determines one full sine period of MIEZE signal and the 16 time frames per oscillating intensity period. The choice of 16 time bins is arbitrary, nevertheless it is a sufficient amount for extracting the sinusoidal signal without reaching the limits of the device too early. The two Agilent generator are providing the driving frequency for the two RF-coils LC-circuit.

Amplifier To order to receive a sufficient field strength in the RF-coils an amplifier is required. Higher harmonics need to be sufficiently suppressed as well, in order to improve quality oscillating current in the coils.

The used amplifiers are the AG1017L by Agilent whose third harmonic is better than -20 dBc and any other harmonics > -28 dBc. The quantity dBc describes the power ratio of a signal to a carrier signal. For the tuning of the signal strength inside the RF-Coil, one can either vary the gain of the amplifier or the output of the frequency generator. In experiments it turned out that the latter method allowed a finer and faster adjustment of the oscillating field strength.

Variable Capacitor The design of the RF resonator circuit, and in particular that of the capacitance adaptation devices (C-boxes), has been adapted from the RESEDA instrument [48]. The eigenfrequency of a resonant LC-circuit is given by

$$\omega_0 = \frac{1}{\sqrt{LC}}, \quad (\text{A.1})$$

where L is the coil's inductance and C the capacity. The tuning of the eigenfrequency is achieved by varying the capacity of the resonant circuit. In MIEZE two capacitance

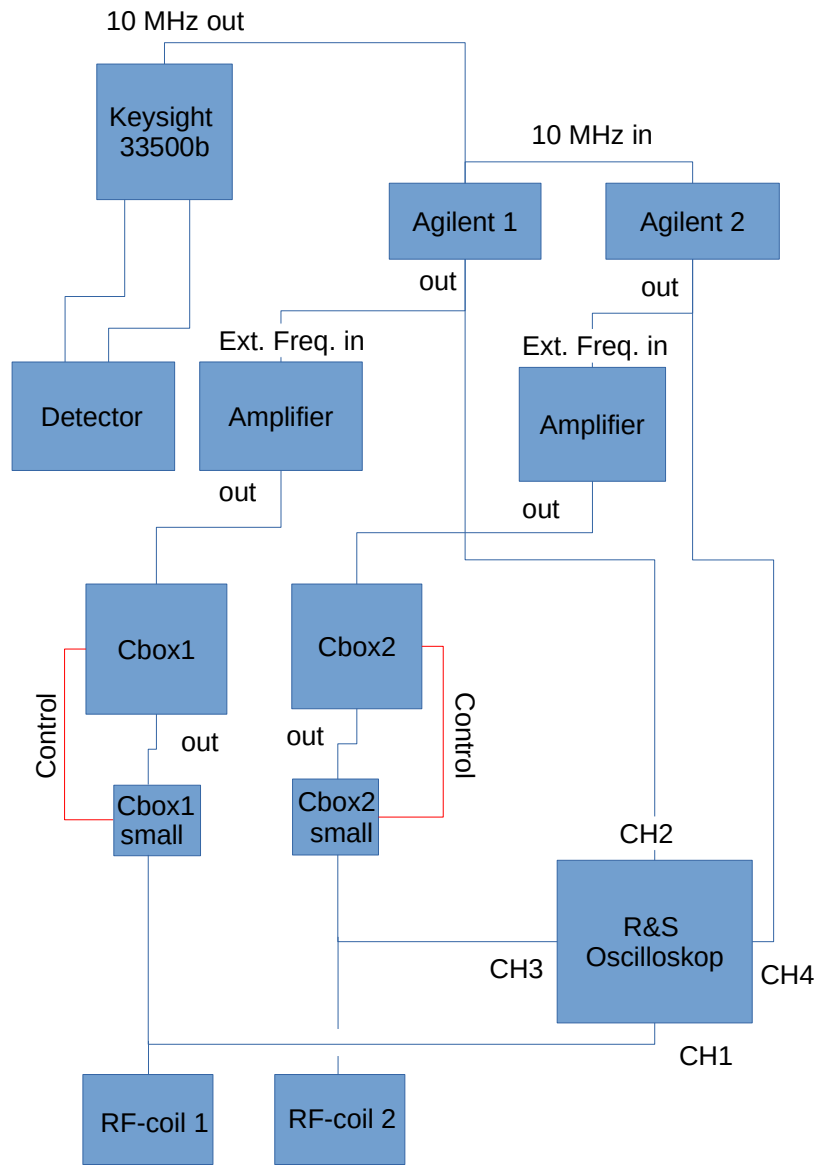


Figure A.1: The circuit diagram of the two RF-coils. It consists of three frequency generators. The Keysight sets the frequencies for the detector time channel and acts as a trigger for the other two Agilent frequency generators. Each RC current generated by the Agilents is amplified and coupled into the resonant circuit of the capacity box (cbox) and the RF-coil.

adaption devices (cbox) are needed, as the two RF-flippers have their own resonant circuit driven at different frequencies. Technically, the capacitance adaption device has three subunits, which are labelled by increasing numbers for both cboxes (Cbox1_1, Cbox1_2..., Cbox2_3). For simplicity, the three different subunits are referred as 'unit 1', 'unit 2' and 'unit 3'. Regarding the circuit diagram figure A.1, unit 1 and 2 are physically installed in the 'Cbox', while unit 3 is installed in 'Cbox1 small', since the latter one was added later in order to reach higher frequencies.

Each of these sub-units consists of a set of parallel connected capacitors with different capacities, where each capacitor can be activated independently. The capacity of the parallel connected capacitors sums up linearly

$$C_{\text{tot}} = \sum_i C_i. \quad (\text{A.2})$$

Each box covers a different range of capacitance and by the combination of all three of them one can increase the range of capacity. The covering range of the sub-units is given in table A.1. unit 1 and cbox 2 can be connected in parallel and in series configuration, while unit 3 is connected in series to the others. In series connection, the capacity sums inversely

$$\frac{1}{C_{\text{tot}}} = \sum_i \frac{1}{C_i}. \quad (\text{A.3})$$

In theory eigenfrequencies from ≈ 25 kHz up to ≈ 7 MHz can be achieved. However

Sub-unit	1	2	3
Range	10-1750 nF	0.22-17.18 nF	22-798 pF

Table A.1: Range of capacitance of the capacitor sub-units.

in reality parasitic capacities, e.g. coaxial cables, are limiting the maximal possible eigenfrequency. The highest achieved eigenfrequency was ≈ 1 MHz, which is sufficient for recent setup.

Oscilloscope An oscilloscope is used to assess the quality of the amplified oscillating signal in the RF coils. For this MIEZE setup the Rhode & Schwarz RTE1104 was used, which is a 4 channel oscilloscope with a bandwidth of 1 GHz, a sampling rate of 2.5 GSa/s per channel and is sensitive to signals down to -50dBmV which is sufficient for our purpose. Its capability of being integrated via Ethernet into the measurement system allows further to automatise the tuning of the RF coils [145].

DC power supply B_0 coils The DC power supplies must provide a high and sufficiently stabilized current to ensure that the accumulated phase of the neutrons does not vary. Due to the low resistance of the coils $R = 260$ m Ω the voltage is not a factor. The devices used for MIEZE measurements were Heinzinger PTN 3p 80-80 (80 V/80 A). They are highly stabilised and comply with these requirements [146].

B Appendix: CuMnSb

All performed temperature dependence scans are shown in figure B.1 as referred to in section 6.3. The blue dots are the measured intensity in dependence of the energy transfer. In the top right corner the respective temperature is shown. The solid green line displays the fit including all components, while the dashed lines show the different fitted components contributing to the fit.

In appendix B.2 all performed energy scans are shown as referred to in section 6.4.1. The blue dots are the measured intensity in dependence of the energy transfer. In the top right corner the respective reciprocal lattice point is shown, which is visualised together with the reciprocal lattice in top left corner. The solid green line displays the fit of the measured peak.

Appendix B.3 shows the magnon line width Γ in comparison with the excitation energy of the magnon obtained by the fits of the energy scans as referred to in section 6.4.1. The blue dots are the line widths in dependence of the momentum transfer, while the red dots refer to the energy of the magnon mode.

B.1 Temperature dependence of energy scans

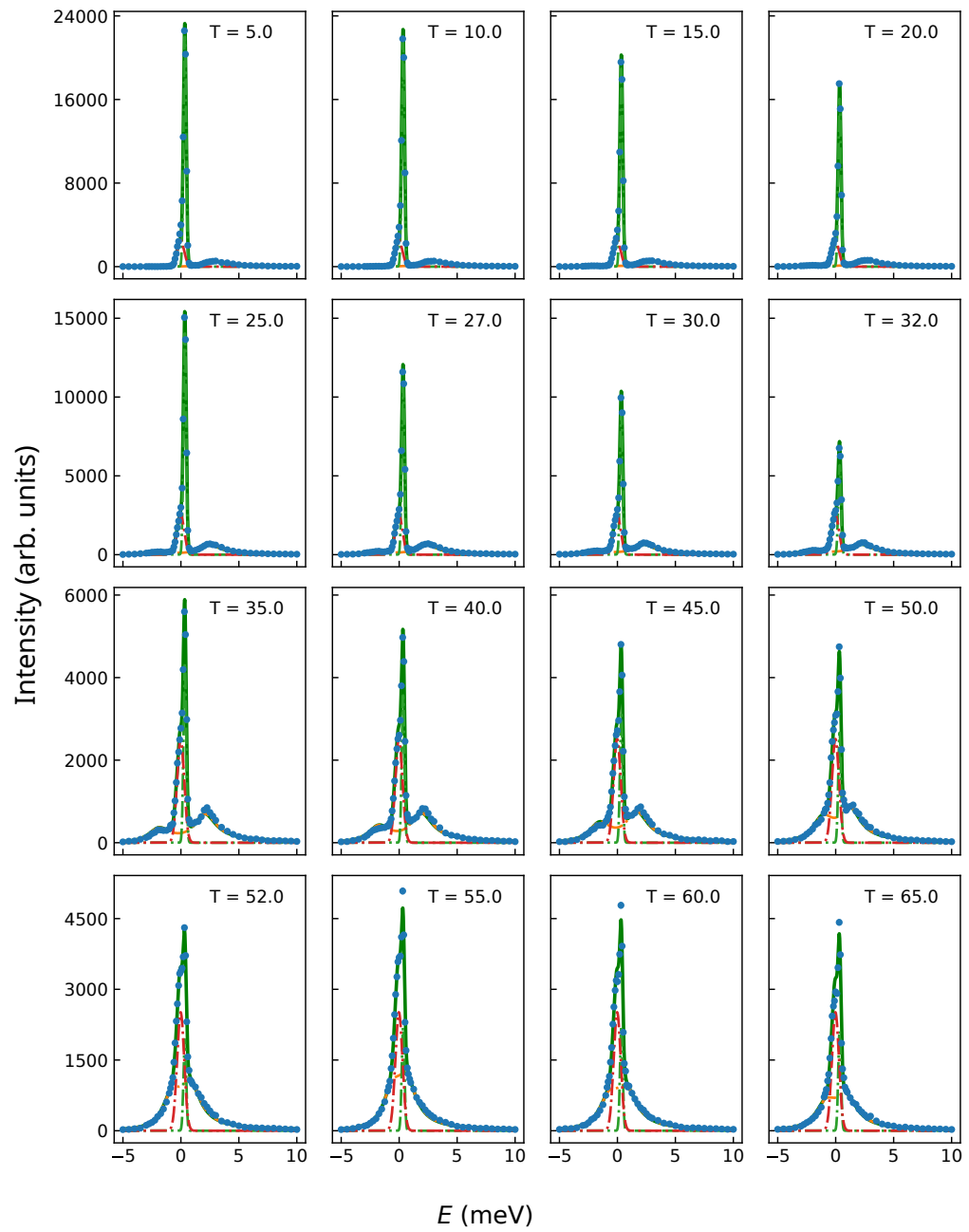


Figure B.1: Fits of the magnon mode at different temperatures. The labeling follows figure 6.3.

B.2 Energy scans at $T = 2$ K for different Q directions

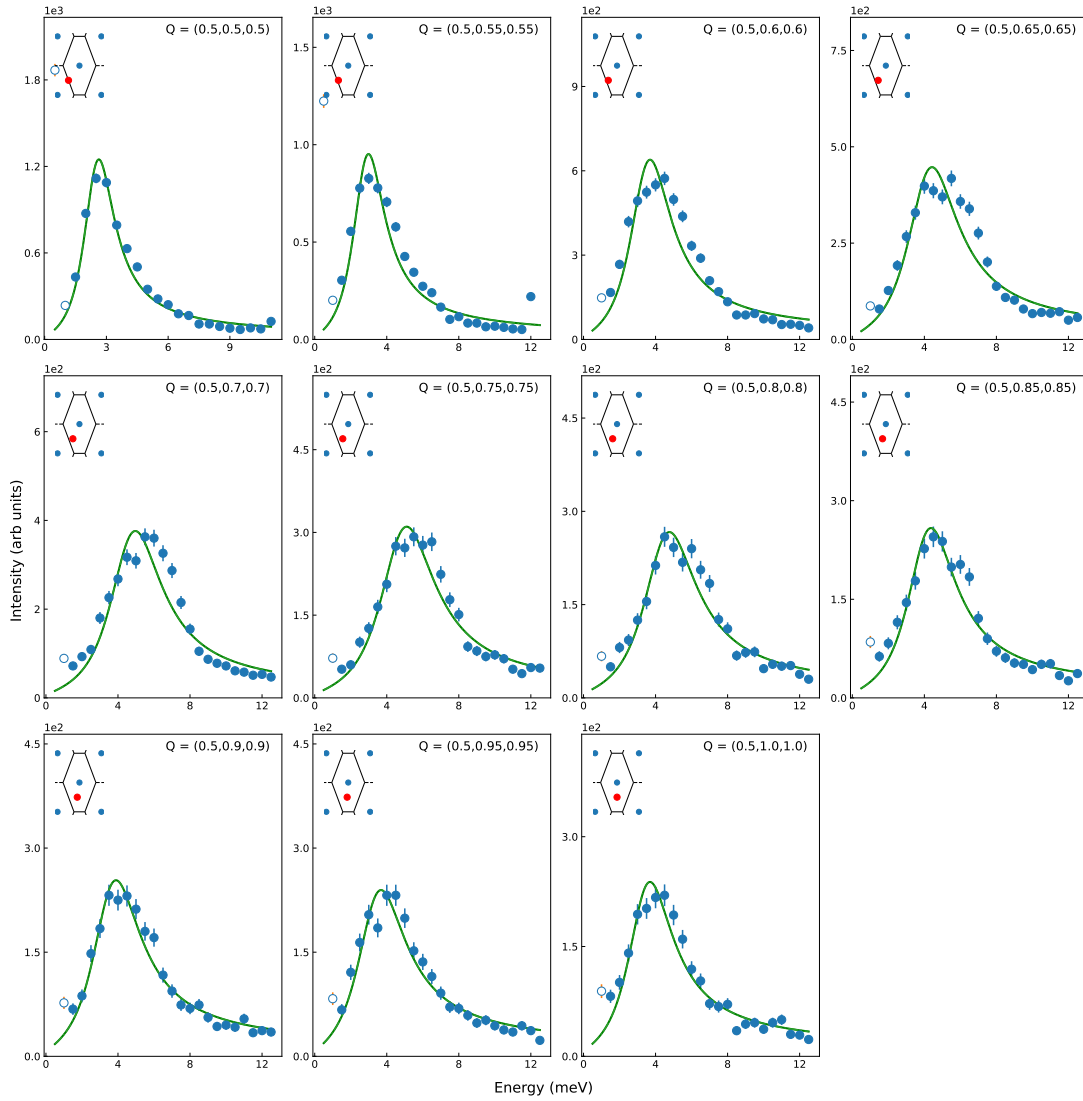


Figure B.2: Energy scans in direction $(0.5, q, q)$.

B Appendix: CuMnSb

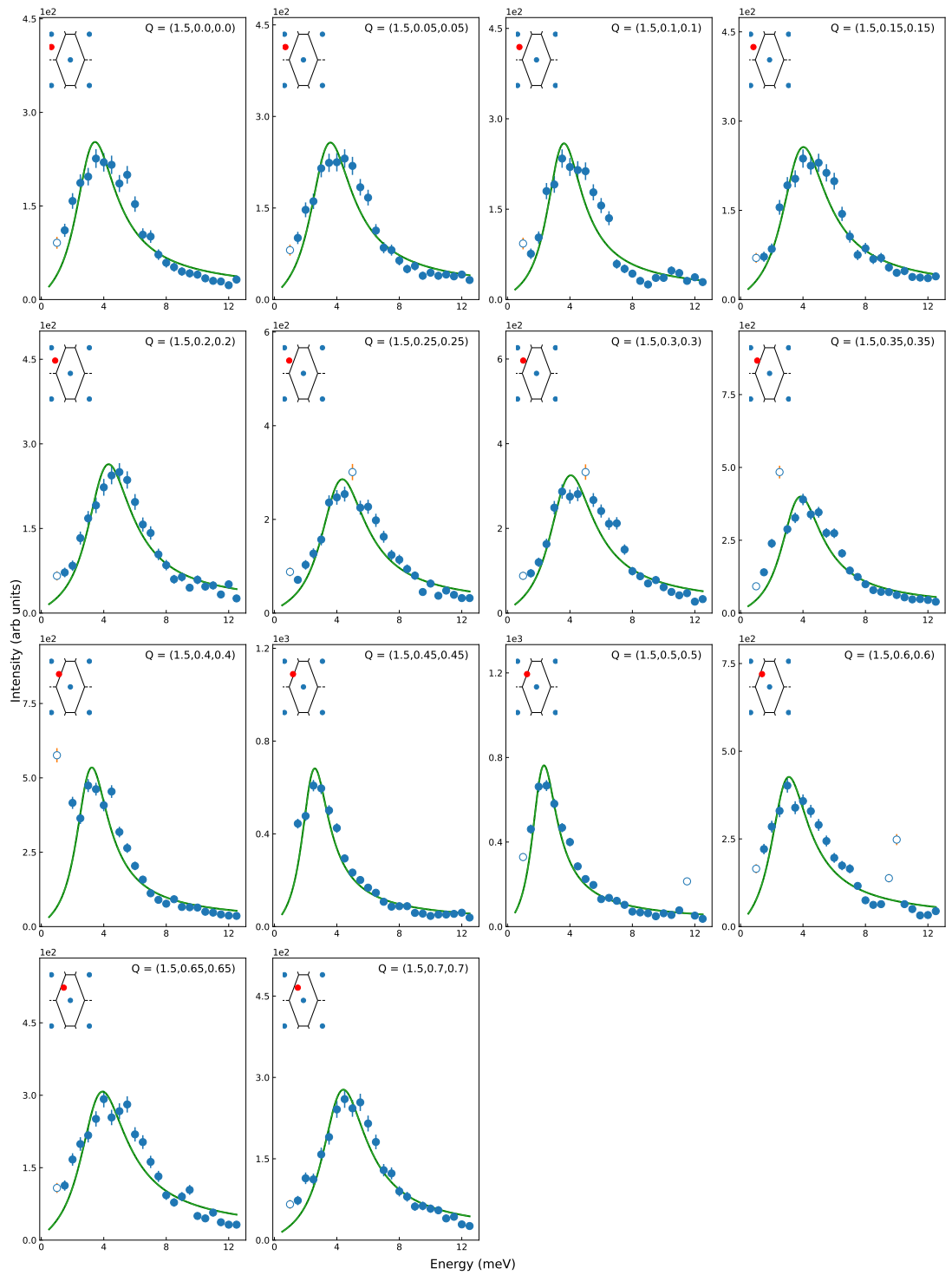


Figure B.3: Energy scans along $(1.5, q, q)$.

B.2 Energy scans at $T = 2$ K for different \mathbf{Q} directions

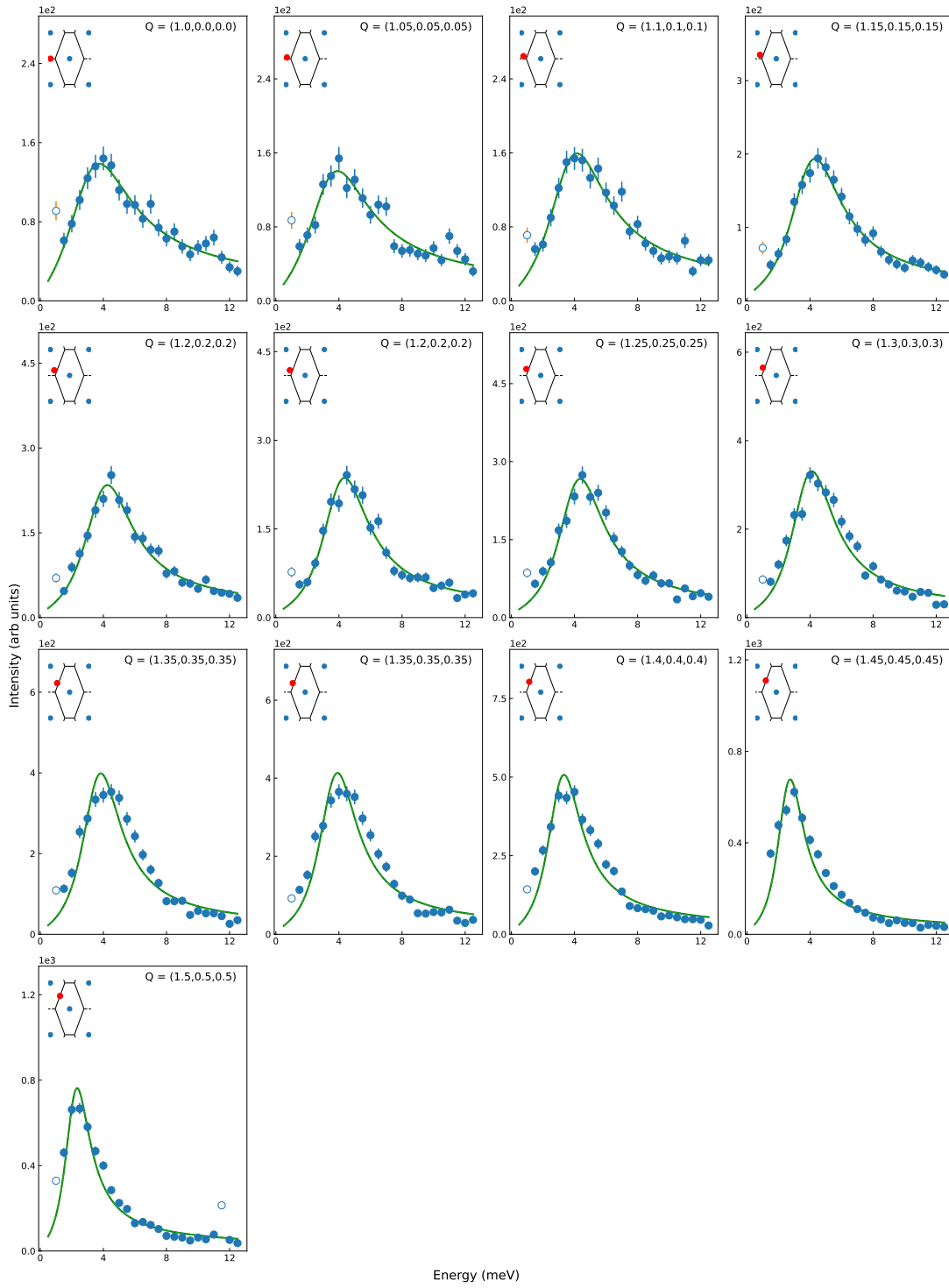


Figure B.4: Energy scans along $(1+q, q, q)$.

B Appendix: CuMnSb

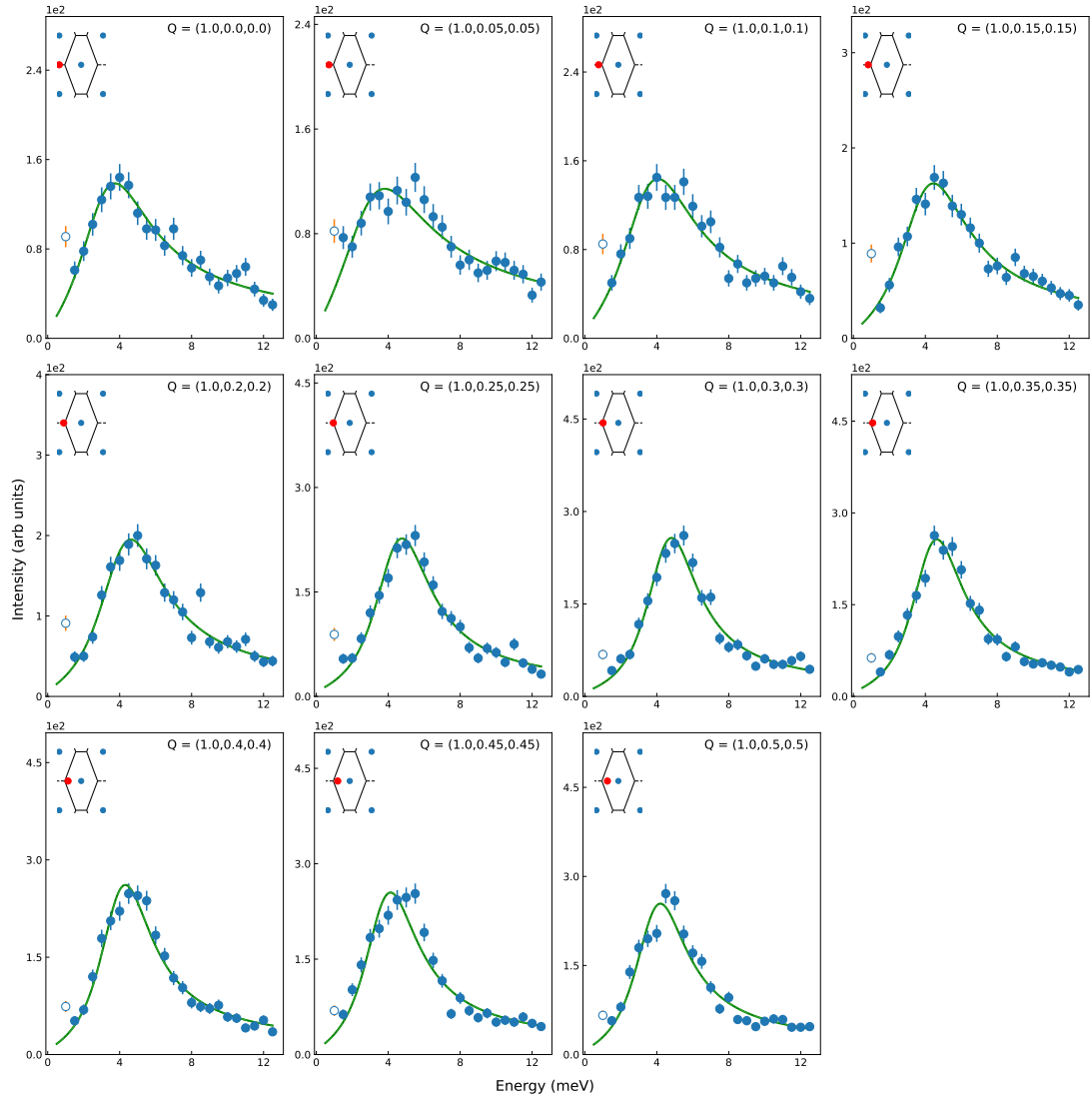


Figure B.5: Energy scans along $(1,q,q)$.

B.2 Energy scans at $T = 2$ K for different \mathbf{Q} directions

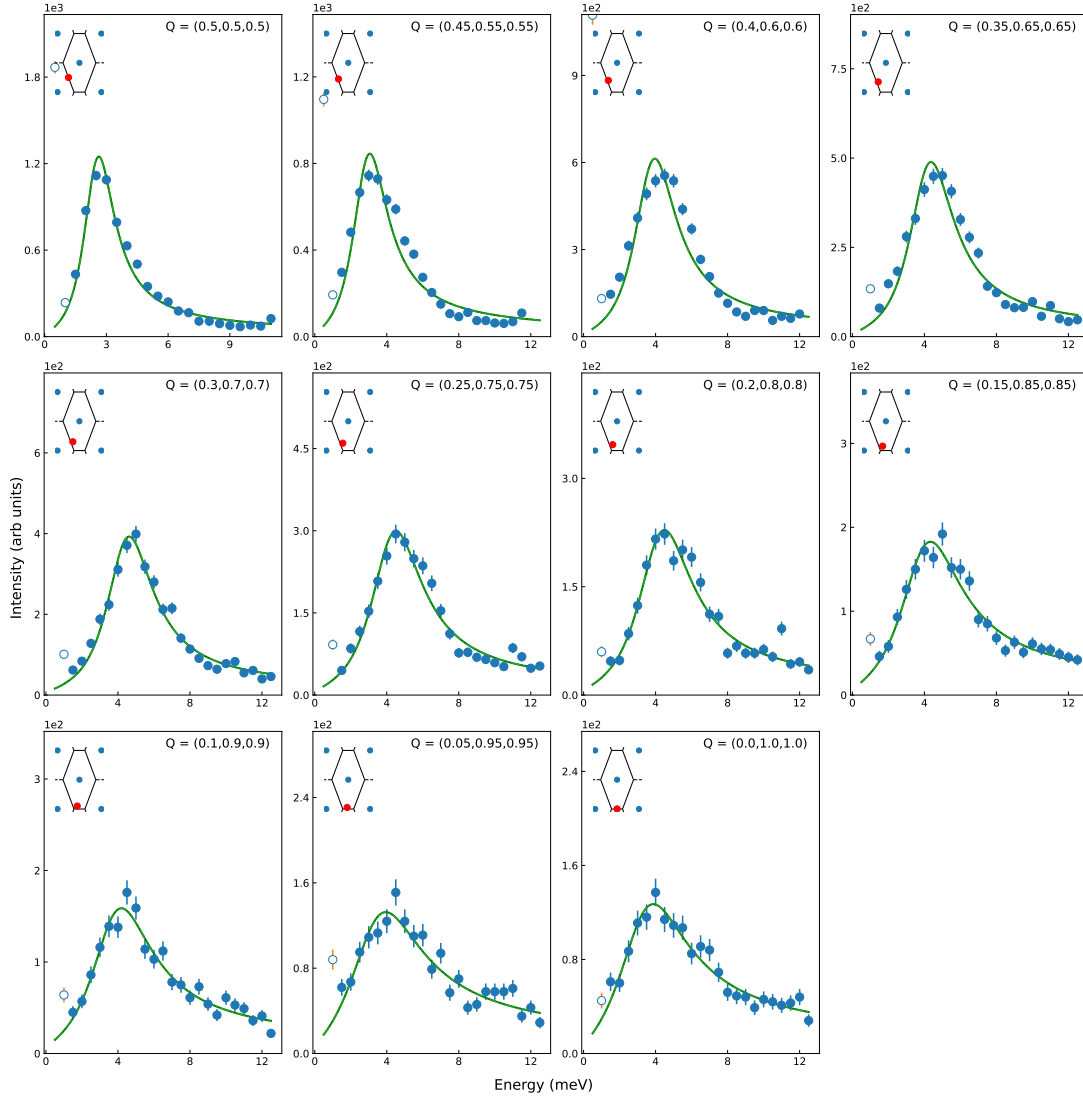


Figure B.6: Energy scans along $(1-q,q,q)$.

B Appendix: CuMnSb

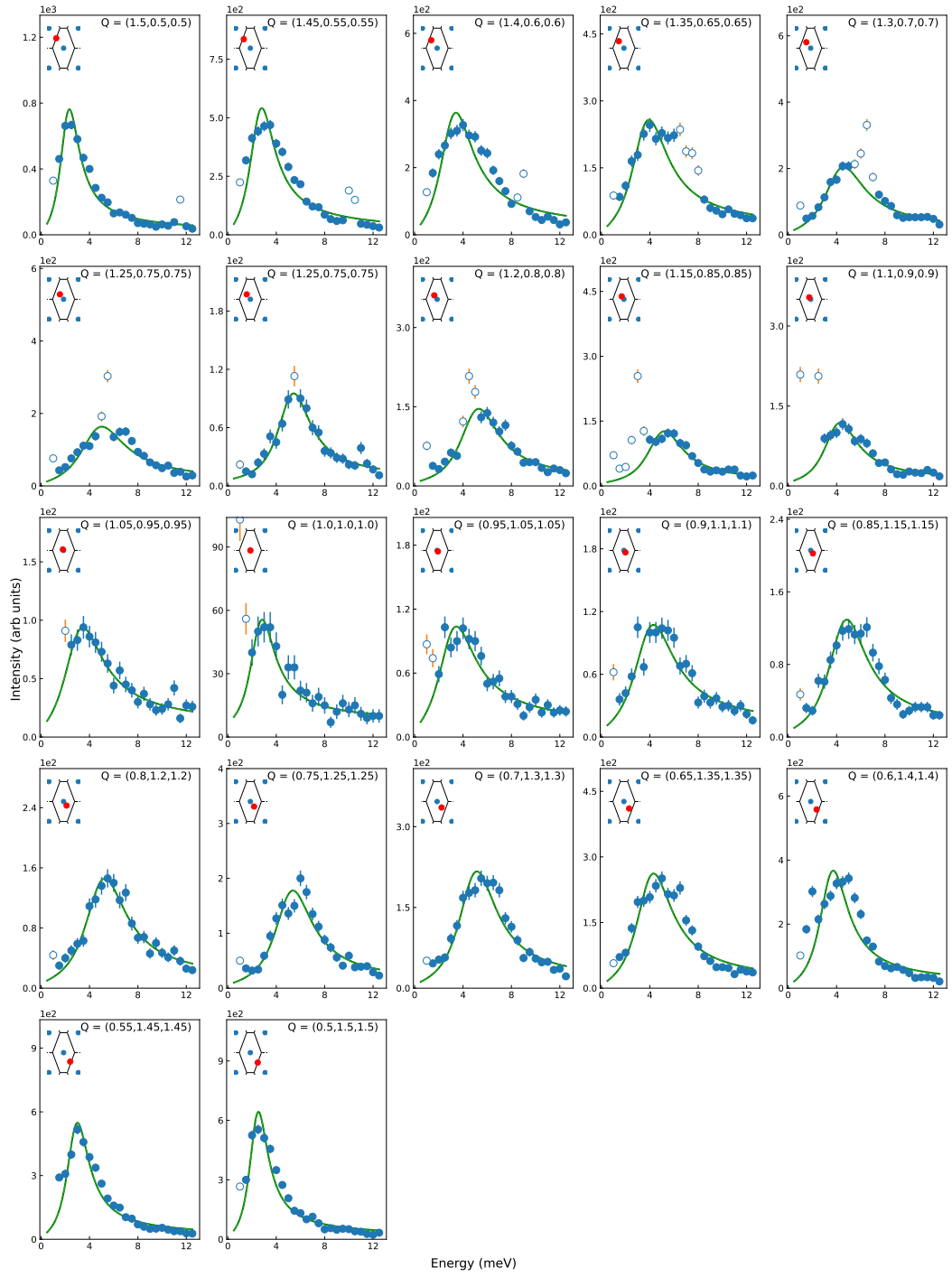


Figure B.7: Energy scans along $(2-q, q, q)$.

B.2 Energy scans at $T = 2$ K for different Q directions

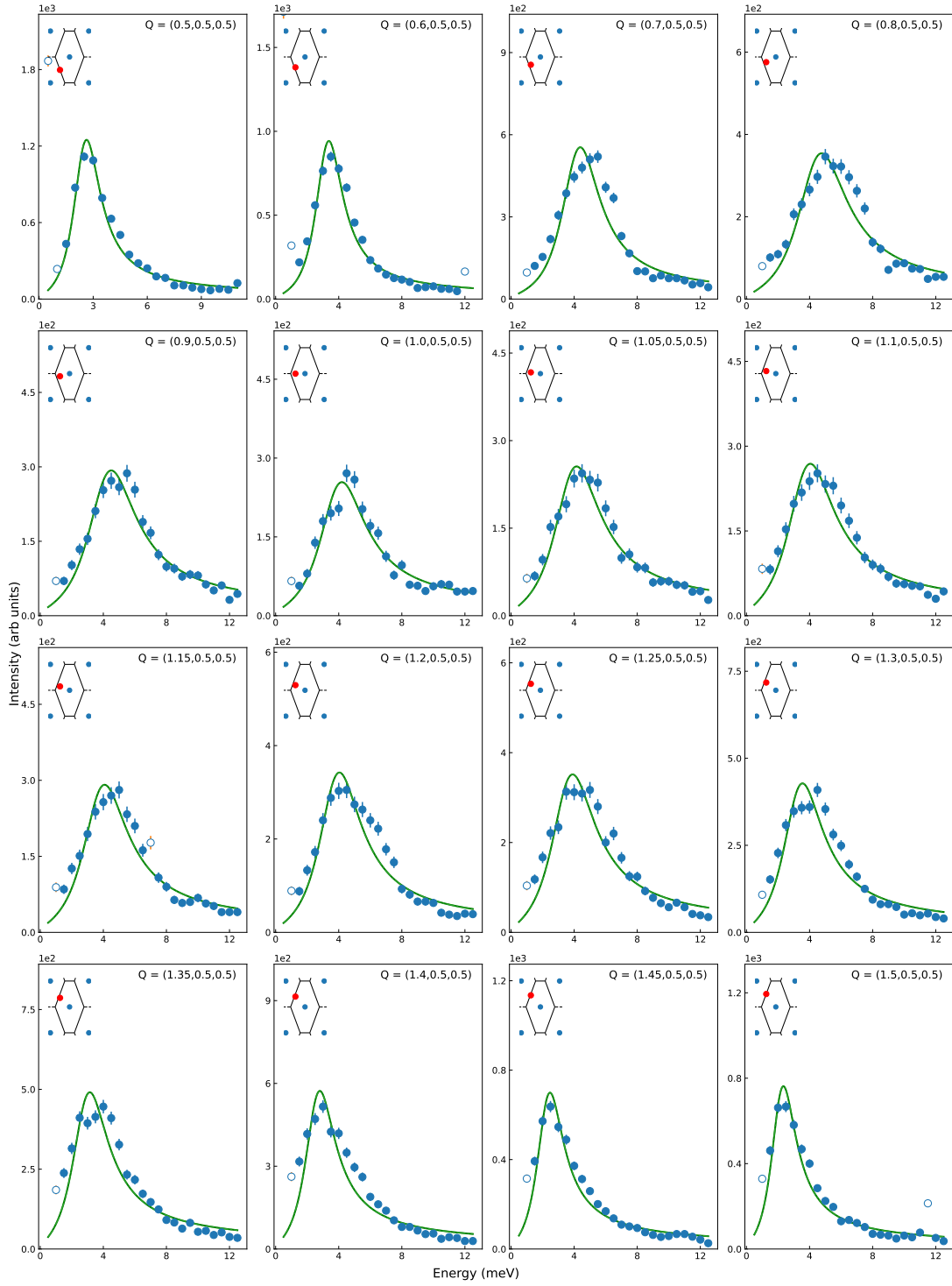


Figure B.8: Energy scans along $(q, 0.5, 0.5)$.

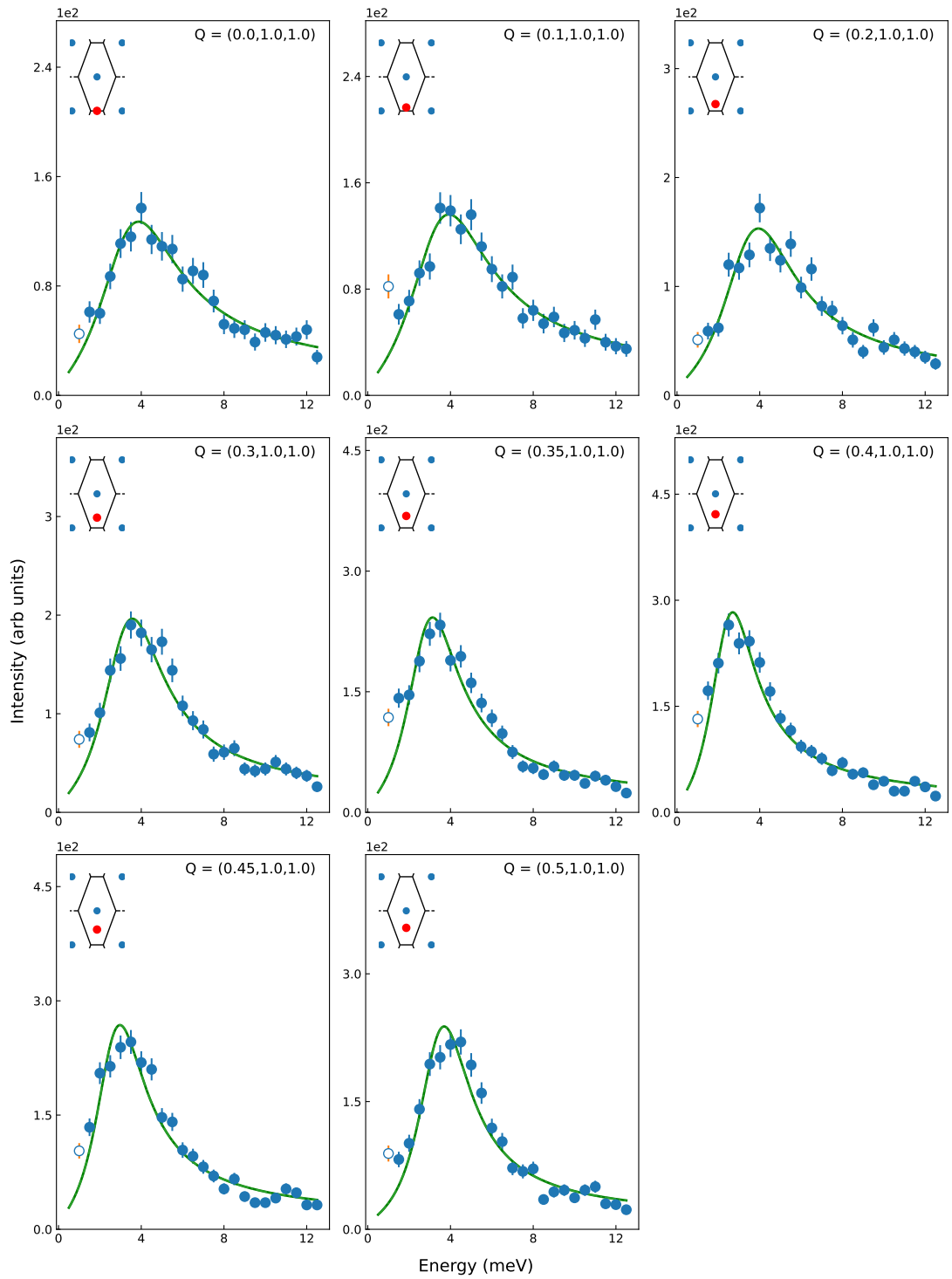


Figure B.9: Energy scans along $(q,1,1)$.

B.2 Energy scans at $T = 2$ K for different \mathbf{Q} directions

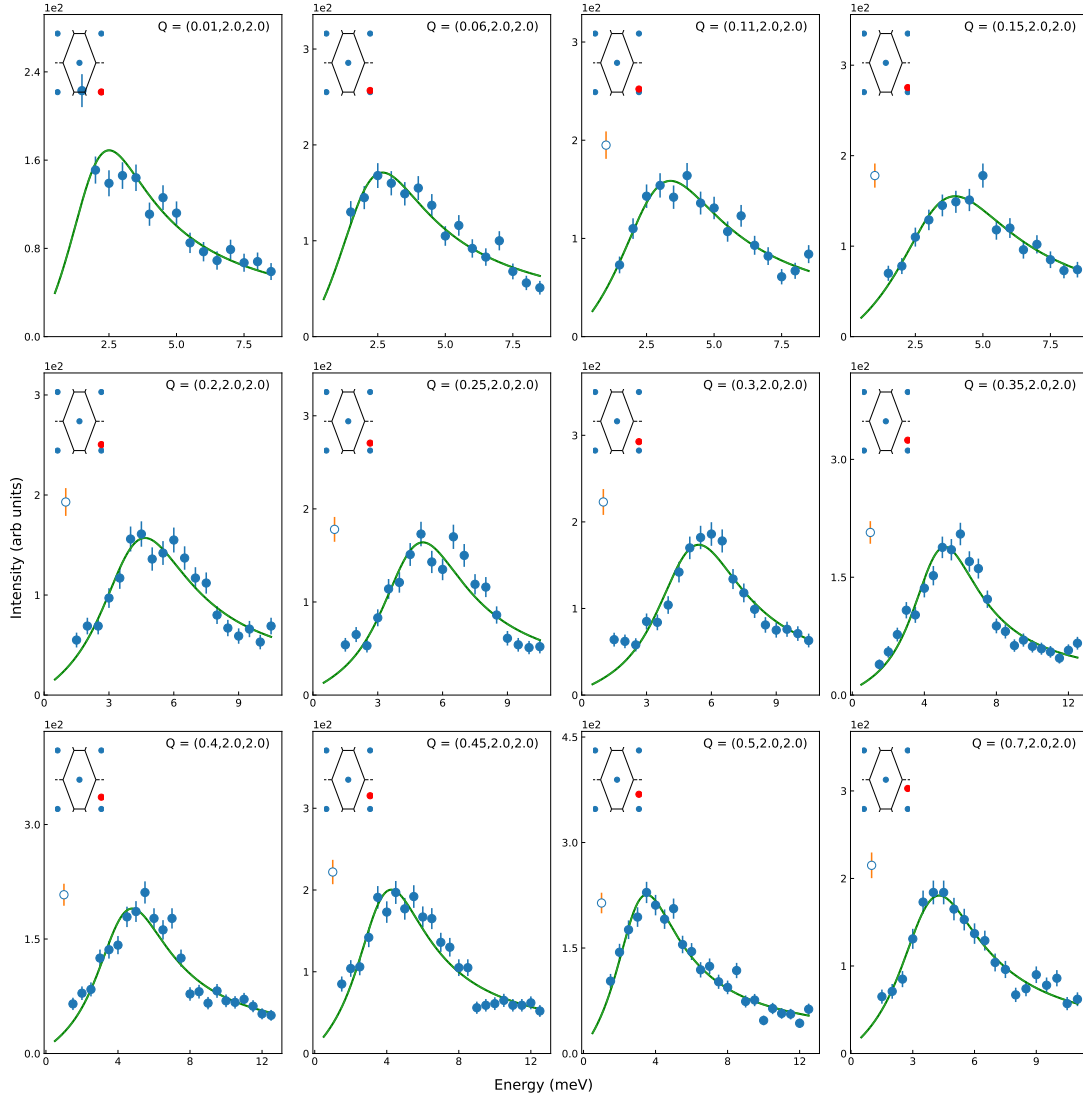


Figure B.10: Energy scans along $(q,2,2)$.

B Appendix: CuMnSb

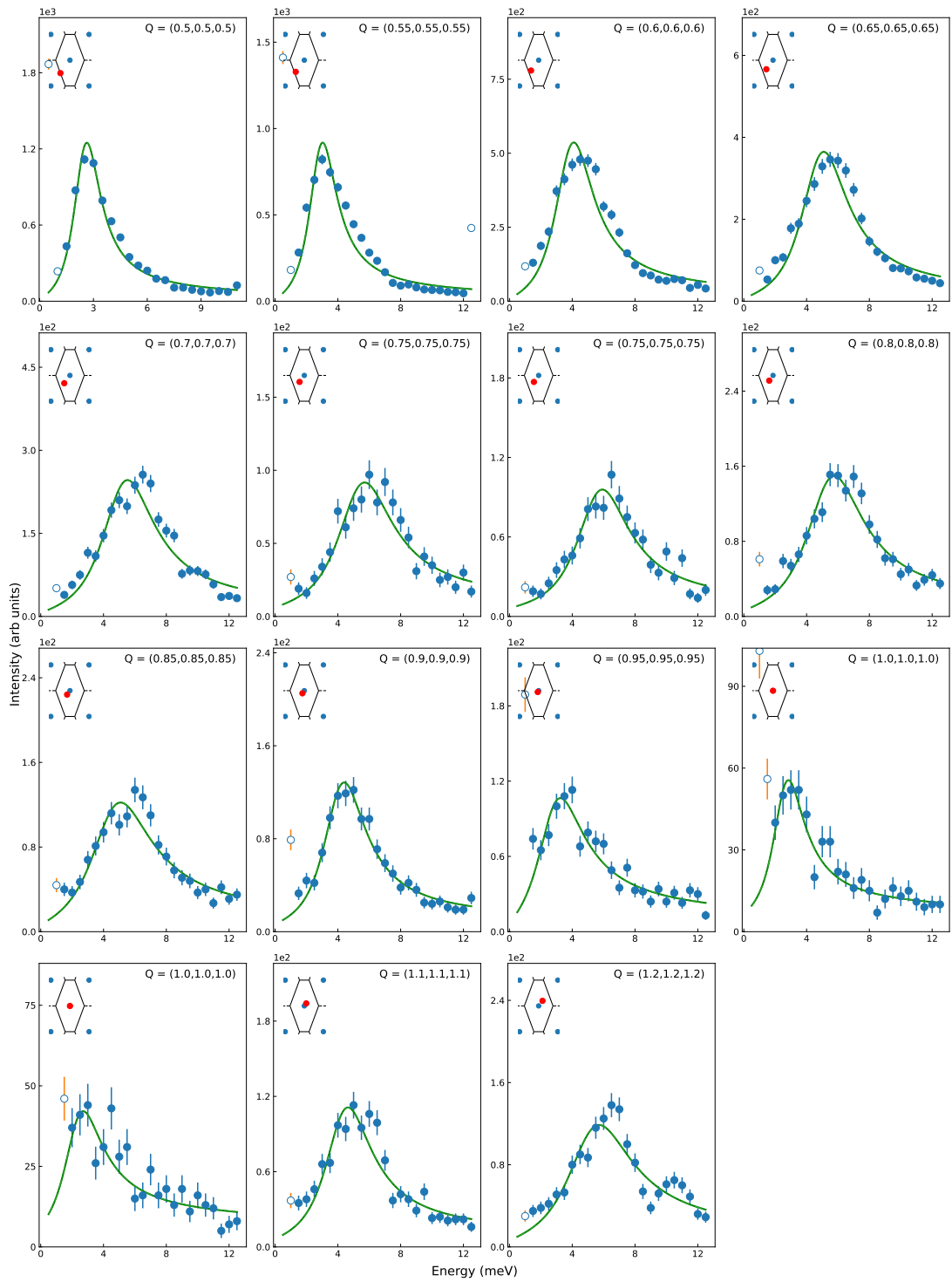


Figure B.11: q,q,q

B.3 Magnon Linewidth

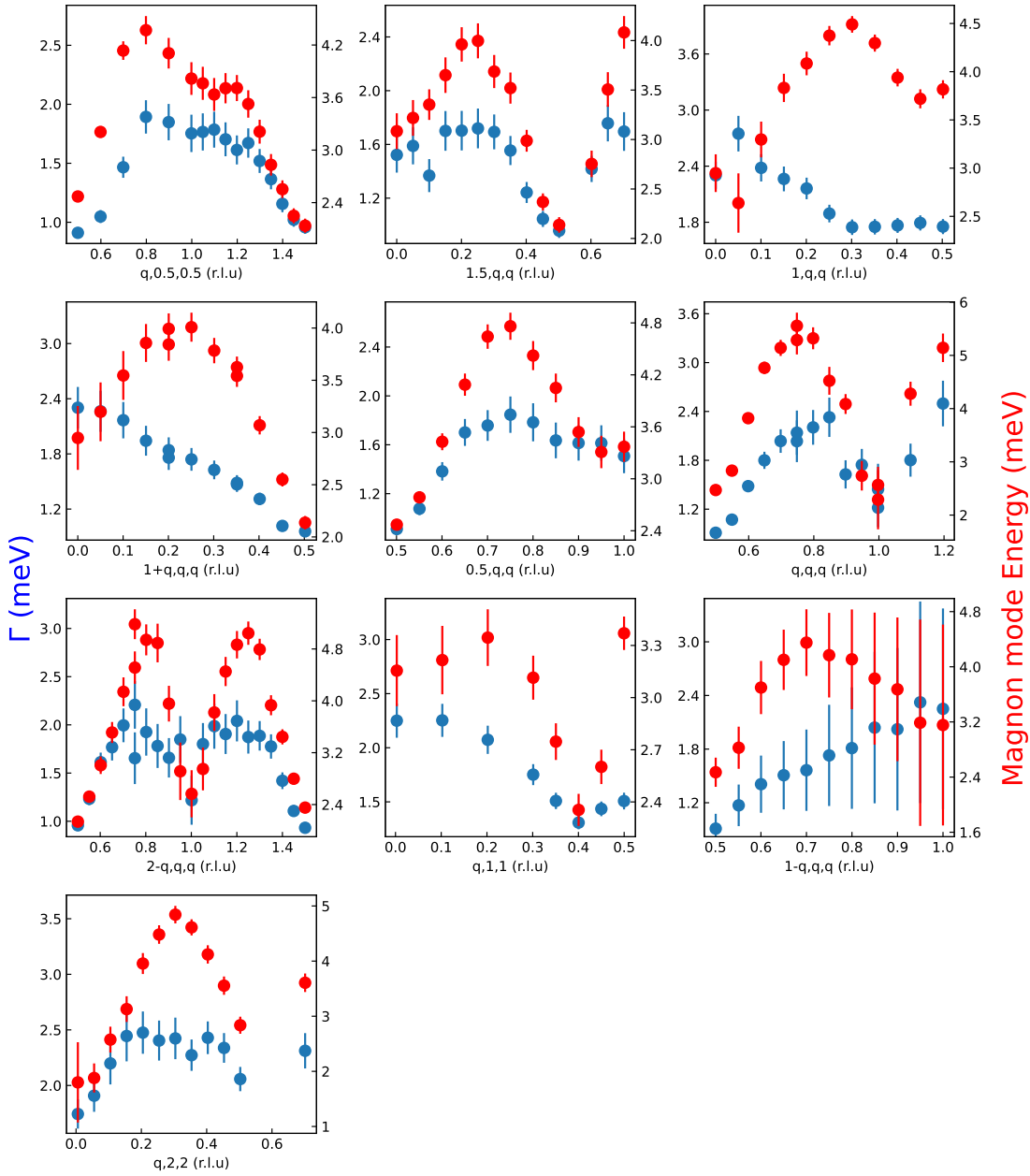


Figure B.12: Linewidth of the magnon mode. The linewidth Γ of the magnon mode obtained by the fits of the energy scans. The linewidth Γ is compared to the magnon mode energy.